

AD-A015 832

PROTOTYPE MOVING BASE ROTATING GRAVITY GRADIOMETER

Charles B. Ames, et al

Hughes Research Laboratories

Prepared for:

Air Force Cambridge Research Laboratories
Defense Advanced Research Projects Agency

May 1975

DISTRIBUTED BY:

NTIS

National Technical Information Service
U. S. DEPARTMENT OF COMMERCE

ADA 015832

PROTOTYPE MOVING BASE ROTATING GRAVITY GRADIOMETER

CHARLES B. AMES, ROBERT L. FORWARD,
PHILIP M. LA HUE, LARRY R. MILLER,
ROBERT W. PETERSON, DAVID W. ROUSE,
JOSEPH B. SETTO AND GEORGE L. WILLIAMS

HUGHES RESEARCH LABORATORIES
3011 MALIBU CANYON ROAD
MALIBU, CALIFORNIA 90265

FINAL REPORT

MAY 1975



APPROVED FOR PUBLIC RELEASE; DISTRIBUTION UNLIMITED.

Sponsored by
DEFENSE ADVANCED RESEARCH PROJECTS AGENCY
ARPA NO. 1836

Monitored by
AIR FORCE CAMBRIDGE RESEARCH LABORATORIES
AIR FORCE SYSTEMS COMMAND
UNITED STATES AIR FORCE
HANSCOM AFB, MASSACHUSETTS 01731

ACCESSION for	
NTIS	White Section <input checked="" type="checkbox"/>
DTIC	Buff. Section <input type="checkbox"/>
UNCLASSIFIED	
JUSTIFICATION	
BY	
DISTRIBUTION/AVAILABILITY NOTES	
ORIG.	AVAIL. NOT/OF SPECIAL
A	

Qualified requestors may obtain additional copies from the Defense Documentation Center. All others should apply to the National Technical Information Service.

UNCLASSIFIED

SECURITY CLASSIFICATION OF THIS PAGE (When Data Entered)

REPORT DOCUMENTATION PAGE		READ INSTRUCTIONS BEFORE COMPLETING FORM										
1. REPORT NUMBER AFCRL-TR-75-0362	2. GOVT ACCESSION NO.	3. RECIPIENT'S CATALOG NUMBER										
4. TITLE (and Subtitle) PROTOTYPE MOVING BASE ROTATING GRAVITY GRADIOMETER		5. TYPE OF REPORT & PERIOD COVERED FINAL REPORT 1 Feb. '72 thru 30 April '75										
		6. PERFORMING ORG. REPORT NUMBER										
7. AUTHOR(s) Charles B. Ames, Robert L. Forward, Philip M. LaHue, Larry R. Miller, Robert W. Peterson, David W. Rouse, Joseph B. Setto & George L. Williams (Consultant)		8. CONTRACT OR GRANT NUMBER(s) F19628-72C-0222										
9. PERFORMING ORGANIZATION NAME AND ADDRESS Hughes Aircraft Company Research Laboratories Division Malibu, CA 90265		10. PROGRAM ELEMENT PROJECT, TASK AREA & WORK UNIT NUMBERS 1838-N/A-N/A 62701 D										
11. CONTROLLING OFFICE NAME AND ADDRESS Air Force Cambridge Research Laboratories Hanscom AFB, Massachusetts 01731 Contract Monitor: James A. Hammond/LWC		12. REPORT DATE May 1975										
		13. NUMBER OF PAGES 167										
14. MONITORING AGENCY NAME & ADDRESS (if different from Controlling Office)		15. SECURITY CLASS. (of this report) UNCLASSIFIED										
		15a. DECLASSIFICATION/DOWNGRADING SCHEDULE										
16. DISTRIBUTION STATEMENT (of this Report) <div style="border: 1px solid black; padding: 5px; width: fit-content; margin: 10px auto;"> <p>DISTRIBUTION STATEMENT A</p> <p>Approved for public release; Distribution Unlimited</p> </div>												
17. DISTRIBUTION STATEMENT (of the abstract entered in Block 20, if different from Report)												
18. SUPPLEMENTARY NOTES This research was sponsored by the Defense Advanced Research Projects Agency. ARPA Order No. 1838												
19. KEY WORDS (Continue on reverse side if necessary and identify by block number) <table style="width: 100%;"> <tr> <td>Gravity Gradiometer</td> <td>Airborne Gradiometer</td> </tr> <tr> <td>Gravitational Mass Sensor</td> <td>Vertical Deflection</td> </tr> <tr> <td>Gravitational Gradient Sensor</td> <td>Motion Isolation and Stabilization</td> </tr> <tr> <td>Gravity Mapping</td> <td>Inertial Guidance</td> </tr> <tr> <td>Mass Detection</td> <td>Navigation</td> </tr> </table>			Gravity Gradiometer	Airborne Gradiometer	Gravitational Mass Sensor	Vertical Deflection	Gravitational Gradient Sensor	Motion Isolation and Stabilization	Gravity Mapping	Inertial Guidance	Mass Detection	Navigation
Gravity Gradiometer	Airborne Gradiometer											
Gravitational Mass Sensor	Vertical Deflection											
Gravitational Gradient Sensor	Motion Isolation and Stabilization											
Gravity Mapping	Inertial Guidance											
Mass Detection	Navigation											
20. ABSTRACT (Continue on reverse side if necessary and identify by block number) Improvements in the knowledge of the earth's gravitation field would be of great value to the scientific fields of geology, geodesy and geophysics. Several military and commercial applications await the development of a mobile gravity gradiometer to provide such data.												

DD FORM 1 JAN 73 1473 EDITION OF 1 NOV 65 IS OBSOLETE

UNCLASSIFIED

SECURITY CLASSIFICATION OF THIS PAGE (When Data Entered)

UNCLASSIFIED

SECURITY CLASSIFICATION OF THIS PAGE(When Data Entered)

Gravity gradient instrumentation has been the topic of an on-going research project at Hughes since 1965. The object of this thirty-nine month contract was to develop a prototype moving base Rotating Gravity Gradiometer (RGG) by redirecting and applying the extensive Hughes capability.

At the contract outset, studies were conducted of error mechanisms and their effects. These studies addressed both the sensor alone and the sensor operating as part of an airborne survey system. It was established that we could achieve the performance objective of 1 Eötvös Unit noise contribution to the determination of the components of the gravity gradient tensor, with an equivalent noise bandwidth of 0.05 Hertz (equivalent to a ten second integration time).

During the second and third year of the contract, subsystems were designed, fabricated and tested. The sensor was assembled, taken through initial rough balancing, and operated during the final month. Sensor operation was demonstrated in both the horizontal and vertical orientation at a noise level of 300 Eötvös Unit (10 sec integration time). The overall performance objective was not met due to a problem with the spin bearings and the preliminary balance state of the sensor. Unfortunately, time was not available to correct the bearing problem and carry out the final precision balance. However, the many achievements that were demonstrable warrant acceleration of the development program.

UNCLASSIFIED

SECURITY CLASSIFICATION OF THIS PAGE(When Data Entered)

TABLE OF CONTENTS

SECTION		PAGE
I	INTRODUCTION	7
II	PROGRAM OVERVIEW	15
	A. Description of the RGG	15
	B. Mechanical Assembly of Sensor	36
	C. Error Analysis Summary	40
	D. System Considerations	43
III	SUBSYSTEM PERFORMANCE	51
	A. Spin Bearings	51
	B. Isoelastic Arm	57
	C. Pivot Torsion Spring Rate and Q Test	60
	D. The Q of the RGG	61
	E. Piezoelectric Transducers	61
	F. New Photoelectric Pickoff	62
	G. Speed Control Servo and Spin Motor Operation	64
	H. Power Input and Signal Output Transformers	66
	I. The "Cap Driver" System	70
	J. RGG Temperature Control	71
	K. RGG Sensor Electronics	74
	L. External RGG Electronics	74
	M. Balance Tubes	75
	N. Computer	76
	O. Vacuum	76

SECTION		PAGE
IV	RGG NOISE PERFORMANCE STATUS	79
	A. Introduction	79
	B. RGG Operation and Signal Processing Model	79
	C. Error Sensitivity Models	82
	D. Error Sensitivity Adjustments	87
	E. Nonspinning RGG Error Coefficient Correction Method	95
	F. Results of Nonrotating Tests and Adjustments	97
	G. Rotating Test Performance	100
V	CONCLUSIONS AND RECOMMENDATIONS	105
	APPENDIX A — Arm/Pivot Attachment Consideration	A-1
	APPENDIX B — Test of Torsional Spring	B-1
	APPENDIX C — Error Coefficient Estimation and Compensation	C-1

LIST OF ILLUSTRATIONS

FIGURE		PAGE
I-1	Prototype moving base RGG contract milestones	11
I-2	RGG sectional view	13
II-A-1-1	RGG sensor	16
II-A-1-2	RGG stator and plastic model stator	18
II-A-1-3	First stage of disassembly	18
II-A-1-4	Second stage of disassembly	19
II-A-1-5	Third stage of disassembly	21
II-A-2-1	Unitized arm/pivot machining sequence	21
II-A-2-2	RGG sectional view	23
II-A-2-3	Assembled sensing components	25
II-A-2-4	Assembled sensing components	26
II-A-3-1	Electronics system block diagram	28
II-A-3-2	RGG external electronics	29
II-A-3-3	Rotating electronics functional schematic	30
II-A-3-4	Power supply logic circuits	31
II-A-3-5	Preamplifier AM-to-FM modulator	31
II-A-3-6	Example of computer printout	33
II-C-2	Summary of RGG tensor element error standard deviations	42
II-D-2-1	Three-axis air bearing stabilized platform	48
II-D-2-2	Gravity Environment Measuring System (GEMS)	49

FIGURE		PAGE
II-D-2-3	Airborne gravity gradiometer mapping system	50
III-A-1	RGG cylindrical oil spin bearing	52
III-A-2	Bearing test fixture	54
III-B-1	Arm plate static test specimen	59
III-E-1	Piezoelectric bender transducer	65
III-F-1	Computer printout	67
III-G-1	Prototype RGG hardware spin motors	68
III-H-1	Rotary transformer	69
III-M-1	Mass balance device	77
IV-B-2-1	Equivalent model of signal process	81
IV-C-1-1	RGG differential moment equation	83
IV-C-2-1	Signal processing error model	86
IV-D-5-1	Prime anisoelasticity	89
IV-D-5-2	Isoelastic arm design	91
IV-D-7-1	Skew misalignment sensitivity	92
IV-D-7-2	Skew misalignment adjustment	93
IV-D-10-1	Phase shift sensitivity	96
IV-E-1	RGG Sensor Test Fixture	98

I. INTRODUCTION

This report documents the accomplishments of a 39 month, \$797,142 contract to develop a prototype Rotating Gravity Gradiometer (RGG) for moving base applications. The contractual and technical milestones of the program are depicted in Fig. I-1. A glance at this chart shows that the 39-month time span is characterized by interrupted contractual funding. A second look will show that this resulted from time and money requirements which exceeded original expectations. The contribution by Hughes Aircraft Company is seen by observing that parallel research efforts were conducted throughout and that continuity was maintained. Not visible in the milestone chart is the wealth of knowledge and the excellence of the RGG sensor produced by this effort. The basic contract was divided into two phases.

Phase One called for analytical studies to evaluate certain design alternatives, establish general performance parameters and specifications, including the general mechanical and electronic configuration. Included in Phase One was a study of the requirements which would be imposed on a stabilization and motion isolation system needed for a specific moving base application. It was then necessary to show that these latter requirements were consistent with existing technology. Phase I was successfully concluded in February 1973 when the study results were presented at AFCRL at a formal Design Review.

Phase Two was the engineering, fabrication and laboratory evaluation test and rework phase. Much of our early effort was concentrated in the preparation and letting of the long-lead-time subcontracts. Other personnel were given the tasks of electronics detailed design, breadboarding, circuit testing and detailed analyses and design of mechanical components, particularly the sensor arms. Later, as the program evolved, the personnel often were convened to discuss the closed loop relationships and interactions of the many subsystems. The result was the formation of a small team which ultimately produced the RGG hardware.

At the start of Phase Two we established a program philosophy which had a significant influence on the conduct of our efforts. Our philosophy stressed that each task and subtask be accomplished with the highest degree of assurance that the end product, the prototype RGG, meet the specified performance goals. In practice, this meant that each subsystem, and its assemblies and components, be analyzed, designed and tested, and redesigned and retested, if necessary, before being integrated with the other subsystems. The purpose, of course, was not only to minimize the number of system problems but to minimize the task of identifying and isolating individual error sources.

The necessity for this philosophy was dictated, in part, by the fact that Phase II authorized the construction of but one single prototype RGG. Unfortunately, this limitation also excluded duplicate subsystems and spare components. Thus, we had to plan a program which had no provision for comparative analyses of simultaneous test results. It also allowed for no unforeseen contingencies which threaten both the schedule and cost of any program. These limitations proved to be severe. They were mostly overcome, however, by designing and fabricating the best possible components within the time and money constraints.

Historically, it is well to remember the years of work that preceded this contract. The Prototype RGG is really a third-generation sensor. The first RGG sensor, made of plastic, was demonstrated in 1967. The 1 E.U. sensitivity of this sensor was excellent and much was learned. However, the original sensor had many limitations rendering it unsuitable for applications in other than orbiting vehicles. From this original design grew the first "hard bearing" RGG sensor. This second-generation sensor was more precisely and ruggedly constructed than its predecessors. Again, much more was learned. The best sensitivity performance was 6.3 E.U. noise level. Work on improving the performance of this "brassboard" model was discontinued in favor of initiating a new program which examined the error sources and studied the design alternatives before constructing hardware. Thus, the present Prototype RGG program was conceived.

The contract was awarded to Hughes as the result of a competitive procurement. Two years later, by February 1974, the configuration of the mechanical assembly had been finalized. The present mechanical design of this sensor is depicted in the RGG Sectional View, Fig. I-2, (taken from the RGG Assembly Drawing No. 740583).

The sequence of this report starts in Section II with an overview of the mechanical and electronic subsystems and then leads to discussions of the assembly process. This is followed by a summary of the error analysis work and finally by some comments about system considerations. Section III provides specific information about the configuration and performance of subsystems and components. Section IV provides details about the error sensitivities, the mechanisms to correct these errors and, lastly, the RGG test results. Section V presents the conclusions and recommendations.

CONTRACT MILESTONES

- (1) Contract award: 1 February 1972
Phase I: Study Phase, \$263,233.
- (2) Semiannual Report No. 1, August 1972.
- (3) Phase I Extension granted, no increase in cost:
1 December 1972.
- (4) R&D Design Evaluation Report, January 1973.
- (5) Semiannual Report No. 2, February 1973.
- (6) Phase I end, 21 February 1973.
Design Review at AFCRL.
Phase II start authorization, \$223,992: hardware design,
fabrication and test phase.
- (7) Comparative Gradiometer Review at AFCRL, 23 October
1973.
- (8) Semiannual Report No. 3, November 1973, draft copies
delivered to AFCRL. Breadboard Electronics and Computer
Subsystems Demonstrated.
Phase II funds depleted, 15 November 1973.
- (9) Unitized Arm/Pivot concept adopted for AFCRL program.
- (10) Phase II cost growth funded, \$219,999, 15 April 1974.
Move personnel and equipment to new, 1100 square foot
laboratory.
- (11) Unitized Arm/Pivot successfully manufactured; spin bear-
ings received from subcontractor.
RGG Rotating Electronics packages assembled and checked
out.
- (12) Phase II funds depleted, RGG sensor nearly assembled.
- (13) RGG sensing components assembled in Inner Rotor; start
static balance tests 26 December 1974.
- (14) Comparative Gradiometer Review at Colorado Springs,
4 February 1975.
- (15) Phase II cost growth funded, \$89,988, 21 February 1975.
- (16) RGG sensor operational two day meeting with AFCRL and
DMA. Complete RGG system electronics demonstrated.
- (17) Phase II technical work complete.

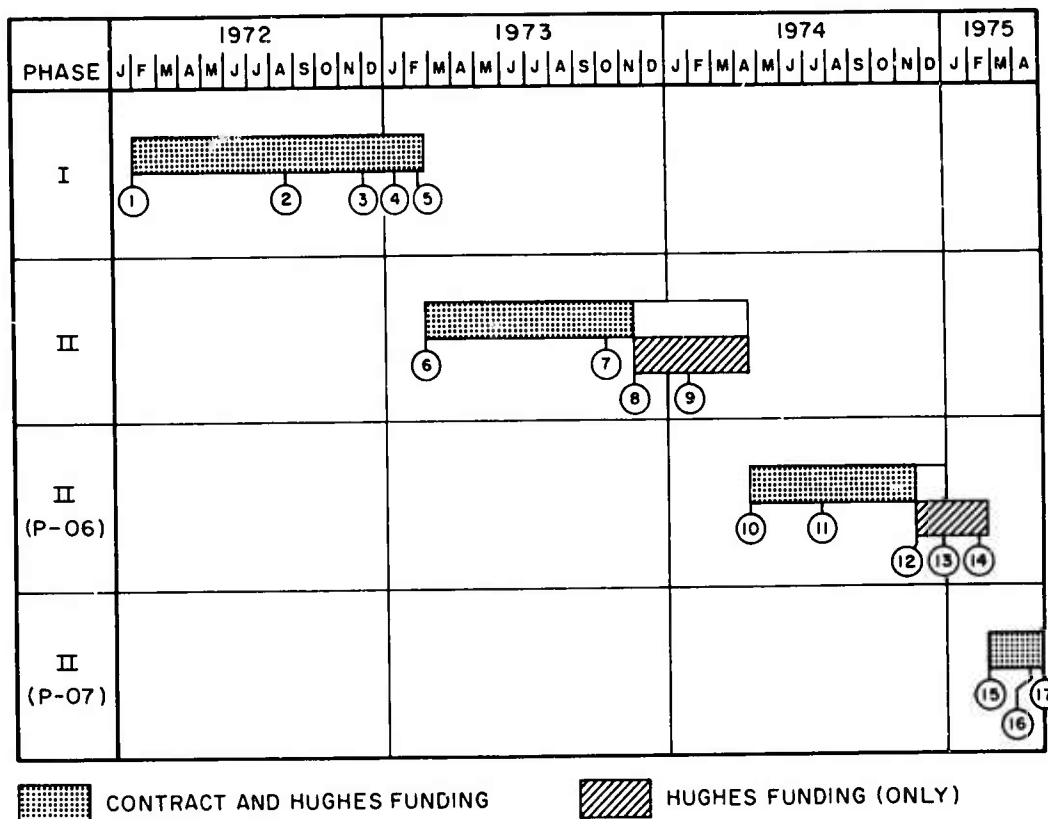


Fig. I-1. Prototype moving base RGG contract milestones.

NOMENCLATURE RGG SECTIONAL VIEW

- | | |
|--|--|
| ① Drag Cup (Top) | ①7 Top Arm Plate
(Arm No. 2) |
| ② Motor (Top) | ①8 Center Plate |
| ③ Spin Bearing (Top) | ①9 Bottom Arm Plate
(Arm No. 1) |
| ④ Light and Photocell | ②0 Heater and Sensing
Winding Slots |
| ⑤ Optics | ②1 Bottom Arm Plate
(Arm No. 2) |
| ⑥ FM Transformer | ②2 Radial Balance
Devices and Mount
(Bottom) |
| ⑦ Encoder Disk | ②3 End Flange
(Bottom) |
| ⑧ Stator | ②4 Printed Circuit
Board ("B") and
Electronics |
| ⑨ Outer Rotor | ②5 Access Plug |
| ⑩ Printed Circuit Board
("A") and Electronics | ②6 Dynamic Balance Screw |
| ⑪ Inner Rotor | ②7 "Cap Driver" Rotating
Capacitor Plates |
| ⑫ Top Arm Plate
(Arm No. 1) | ②8 Power Input
Transformer |
| ⑬ Torsional Pivots (Top) | ②9 Terminals, Drive
Motor (Bottom) |
| ⑭ Piezoelectric Trans-
ducer and Mount | |
| ⑮ Mass, Arm No. 1 | |
| ⑯ Balance Screw, Tan-
gential (Arm No. 1)
(Radial Balance Screws
not shown) | |

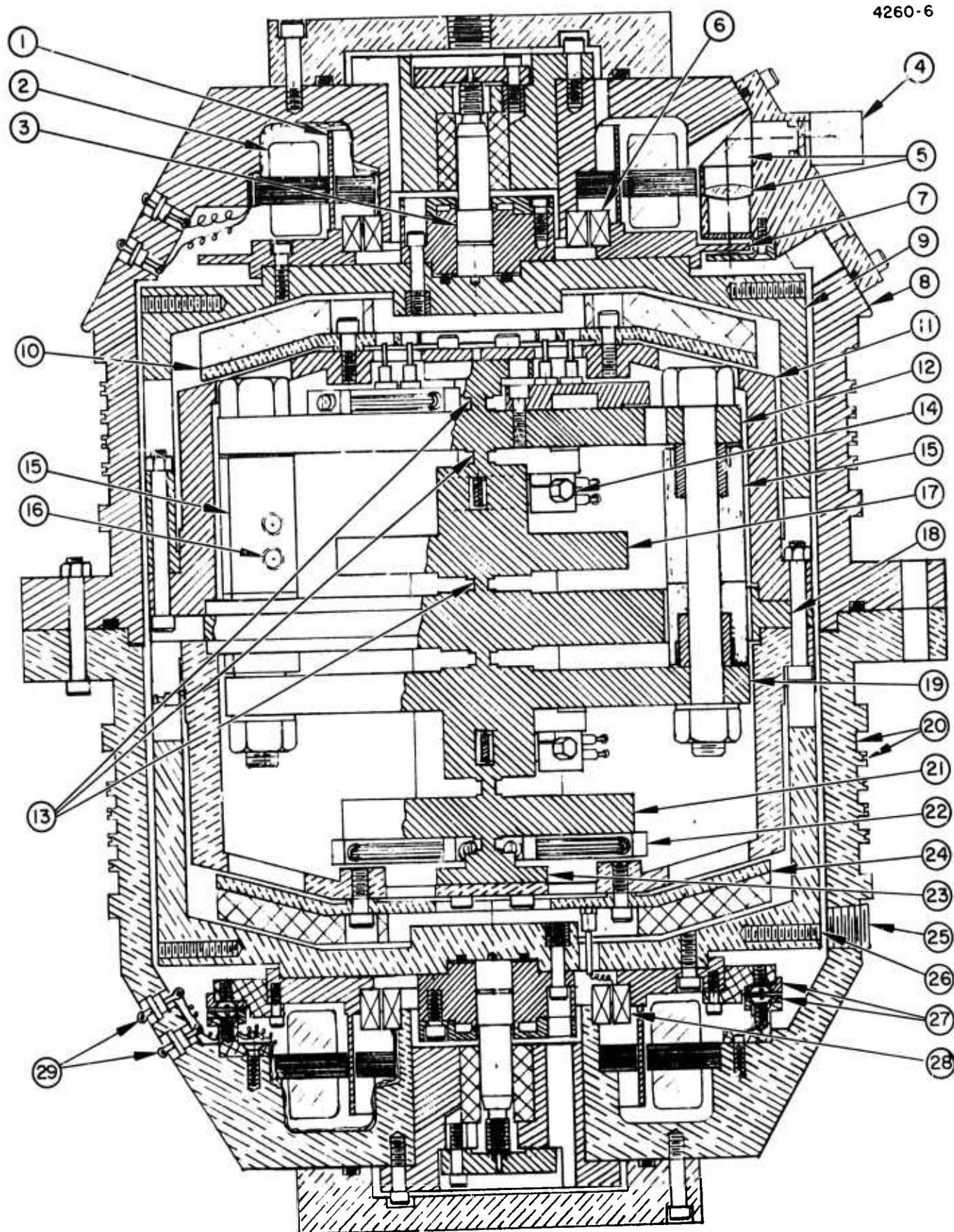


Fig. I-2. RGG Sectional view.

II. PROGRAM OVERVIEW

A. Description of the RGG

1. General Description

The fully assembled RGG sensor is shown in Fig. II-A-1-1. The cylindrical outer housing (Stator) is approximately 20 cm in diameter, is nearly 30 cm in length and, fully assembled, has a total mass of approximately 16 kG. The sensor dimensions have not been minimized or otherwise optimized for a particular volumetric or specific form-factor viewpoint. Time and money constraints restricted the iterative processes required to achieve dimensional optimization. In the future when it becomes desirable to address such considerations, we feel certain that the existing design will lend itself to weight and size reductions.

The prototype RGG is functionally identical to its Hughes RGG predecessors which employ a rotating reference frame to preferentially improve the signal-to-noise ratio. The Hughes Rotating Gravity Gradiometer consists of two orthogonal mass quadrupoles (arms) which are torsionally coupled to each other and to a common supporting structure (the rotor case). This structure has two fundamental torsionally resonant frequencies, the "sum mode" which is related to the common movement of the arms and the "difference mode" which is related to their differential motion. The spin speed is selected to be equal to one half the differential mode resonant frequency in order to provide resonant amplification of the gravity gradient signal.

When the mass quadrupoles are rotated at constant angular velocity about the torsional axis in a nonuniform gravity field, the second order gradients of the field create periodic differential moments on the arms at twice the spin frequency. The differential mode motion is sensed by piezoelectric transducers, and the resultant signal is amplified, filtered, and frequency modulated within the rotor for transmission to the stator. The FM signal is synchronously demodulated digitally into two quadrature channels using rotor position information. The process is functionally analogous to phase detection of the original

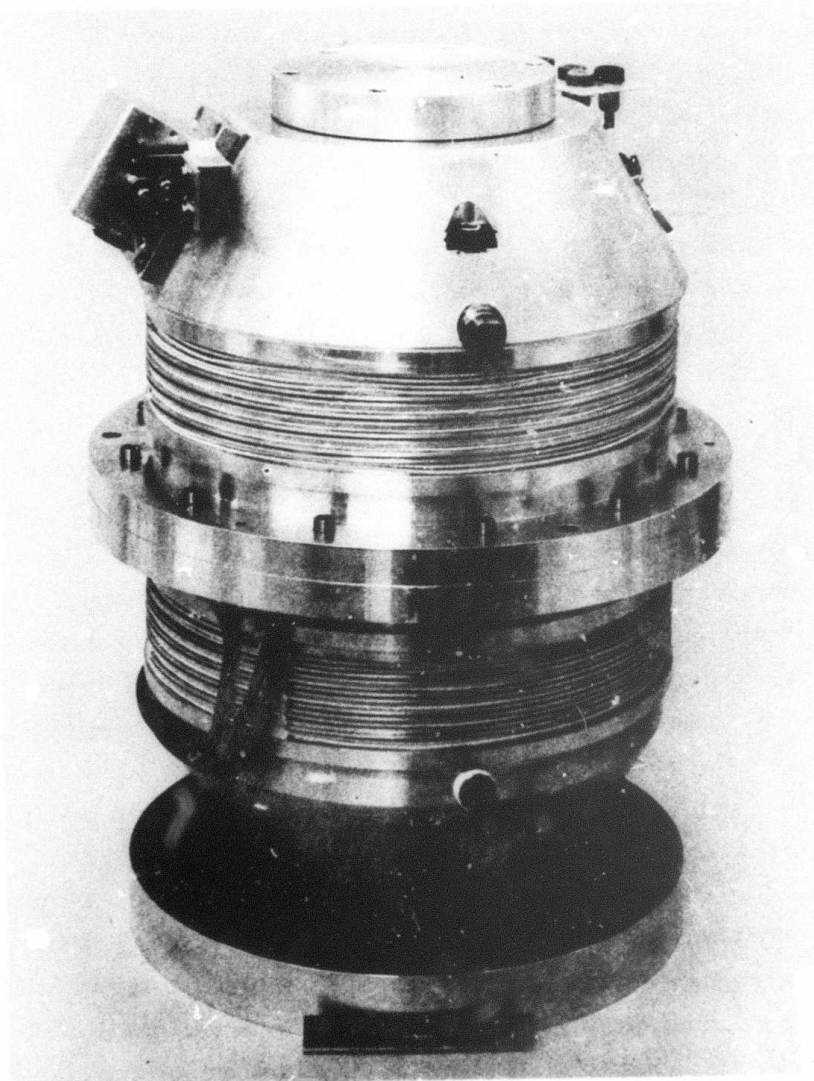


Fig. II-A-1-1. RGG Sensor.

analog signal into two channels using the sine and cosine of twice the relative rotor angle. The digitized signals are then filtered (time averaged) to provide the RGG output signals in digital form.

Despite functional similarities with its predecessors, the mechanization details of the prototype RGG are necessarily different. The differences are primarily due to the more difficult objective of designing a gravity gradiometer to operate in a moving vehicle environment. Also, because we continue to gain increased understanding of the problems and their solutions, the mechanization of certain subsystems have continued to evolve until the specified goals have been fully achieved.

To assist the reader to gain an overview of the RGG mechanical components and familiarity with the terminology, the following discussion is offered. The photographs of the clear plastic model are better suited for this purpose than are photographs of the actual hardware. The plastic model was constructed in March 1974, nearly one year before the hardware was first assembled. Accordingly, differences do exist but they are insignificant for initial familiarization.

Figure II-A-1-2 depicts the Stators of the actual RGG hardware beside the plastic model to illustrate the general similarity.

Figure II-A-1-3 depicts the first step in disassembly. Number 1 points to the Stator or housing assembly, which in turn, mounts to an environmental isolation system. Number 2 points to the Outer Rotor which is supported within the Stator, at each end, by two journal bearings (not shown). The Outer Rotor is rotated by two electric motors. Number 3 points to the "drag cup" component of each motor. Number 4 points to the slotted encoder disk, a component of the extremely precise speed control servo system.

Figure II-A-1-4 depicts the second state of disassembly. Number 5 points to the Outer Rotor. Number 6 points to the Inner Rotor containing the Sensing Components. Each half of the Inner Rotor is bolted to its corresponding half of the Outer Rotor to facilitate alignment during assembly (to obtain coincidence of axes of the Sensing

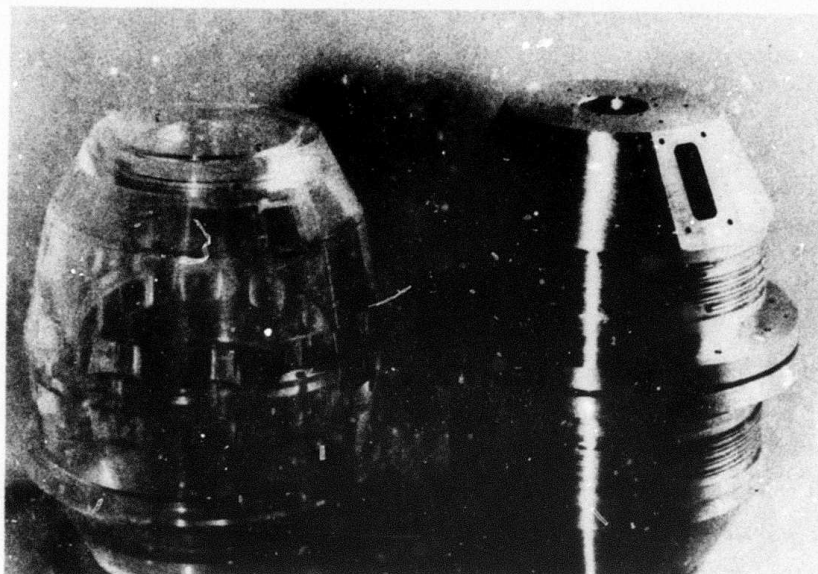


Fig. II-A-1-2. RGG Stator and Plastic Model Stator.

M10255

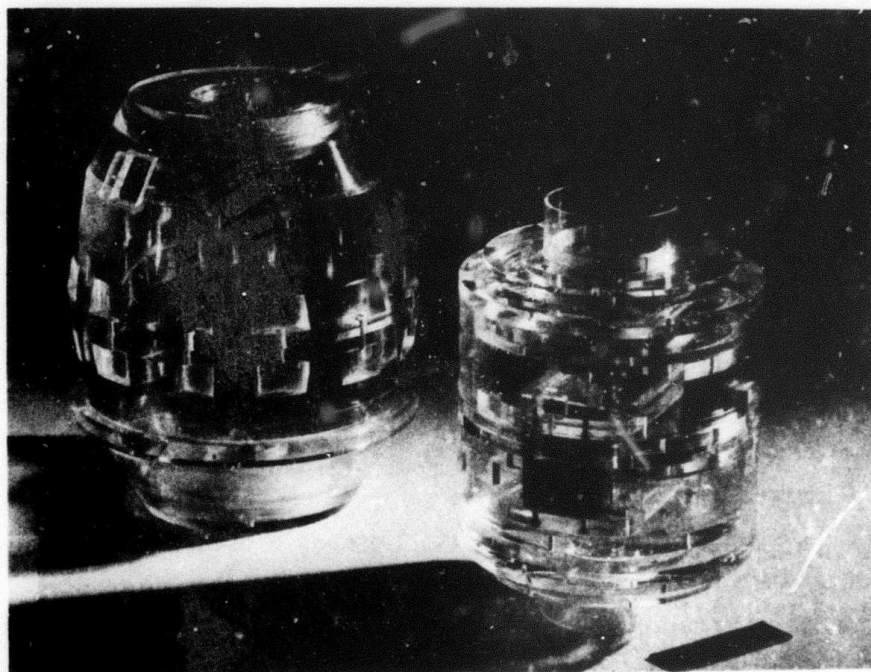


Fig. II-A-1-3. First stage of disassembly.

M10256

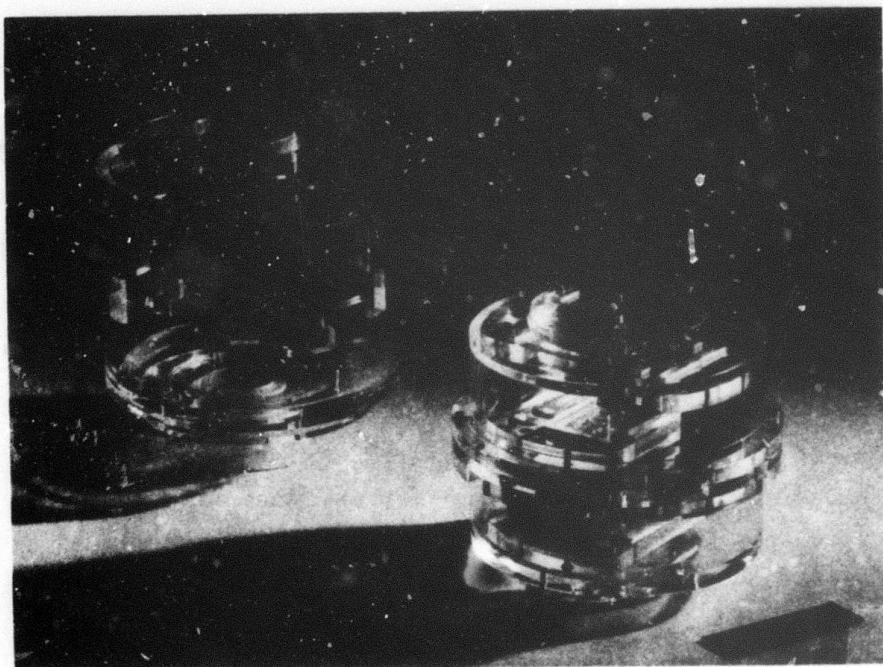


Fig. II-A-1-4. Second stage of disassembly.

Components with the spin axis). Number 7 points to one of the cylindrical volumes which contains the rotating electronics.

Figure II-A-1-5 depicts the third stage of disassembly. Number 8 points to the Inner Rotor with the Sensing Components removed (shown at the right). The Inner Rotor supports the Sensing Components at each end, by two bolted flanges (not shown) at each end of the column (No. 7) of six torsional pivots (see Sectional Drawing in Introduction) and at the circumference by bolts through the Center Plate (No. 9).

2. Sensing Components

a. Unitized Arm-Pivot Description — Selection of the method of attachment of the arm plates to the single-piece pivot structure was a difficult and time-consuming process. Three fastening techniques were considered: (1) an interference fit between the pivot boss and the arm, (2) various clamping methods, and (3) use of high-strength bonding agents. A detailed discussion of these tradeoffs is contained in Appendix A. All of these attachment methods had drawbacks. A decision to select from one of these three attaching techniques would have involved many undesirable compromises. Before a final decision was made, contract funds were depleted which resulted in a temporary work stoppage.

During this time span, it is fortunate that our attention was directed toward a NASA gradiometer program, because an entirely new design approach was developed. The new solution was applicable to the AFCRL design and it provided a significantly improved solution to the arm-pivot attachment problem.

The new concept called for making the pivots and arms from one single ingot of aluminum; it thus became known as the Unitized Arm-Pivot. The new solution presented some new considerations such as the unknown difficulties in machining this intricate part. Our first concern was directed toward the difficulties in making the relatively "long reach" between each arm plate to machine the central column down to the required diameters of the torsional pivots. The

M10257

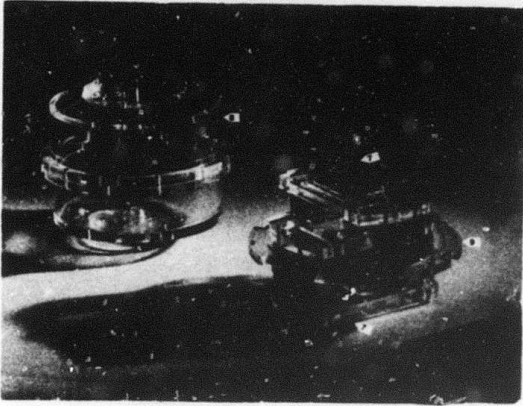


Fig. II-A-1-5.
Third stage of disassembly.

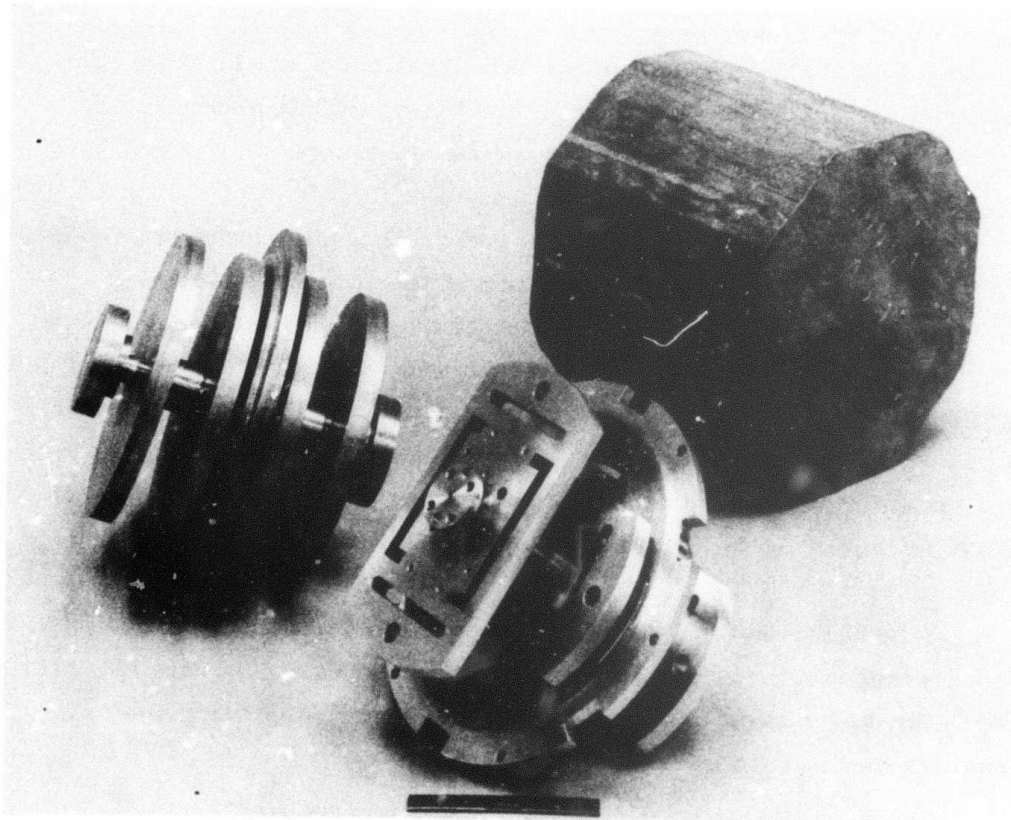


Fig. II-A-2-1. Unitized arm/pivot machining sequence.

question of this particular machining operation was evaluated using a prototype part; the machining operations were found to be difficult but feasible. The machining vendor selected to manufacture this part made the first part with no breakage. The concept of a unitized arm-pivot was then established as not only feasible but a superior solution to the three alternatives whereby the arm to the pivot attachment was to have been accomplished as a post-machining assembly step.

In the unitized design, the arms, the torsional pivots and the Central Plate, are made from a single forging of aluminum. Figure II-A-2-1 illustrates the progressive steps in machining the final unit. Conventional machining techniques and tools were used throughout. The details of the Unitized Arm Pivot are better depicted in the RGG sectional drawing (see Fig. II-A-2-2).

Referring to Fig. II-A-2-2, the anisoelastic cutouts (No. 1) in the arms and the end mass cutouts (No. 2) in the Central Plate are machined by the Electro-Discharge Machining (EDM) process. Turning of the torsion pivots (No. 3) to the final diameter is the last step in the machining process.

The piezoelectric transducers (No. 4) are mounted by means of the short standoff posts (No. 5). Each of the two transducers is clamped to the standoff posts and pass through the slots (No. 6) in the outer arm bosses (No. 7). By contrast, our prior design required use of relatively long standoff posts which carried the torsional deflections from the arm plates to two sets of interleaved mounting supports for each transducer. Thus, a further advantage and simplification of the unitized concept is the improved method of mounting the piezoelectric transducers.

The Inner Rotor (No. 8) supports the pivot end flanges (No. 9) by providing rigid mechanical links back to the Central Plate (No. 10). The Outer Rotor (No. 11) provides the means of supporting the rotor structure on the spin bearings (No. 12).

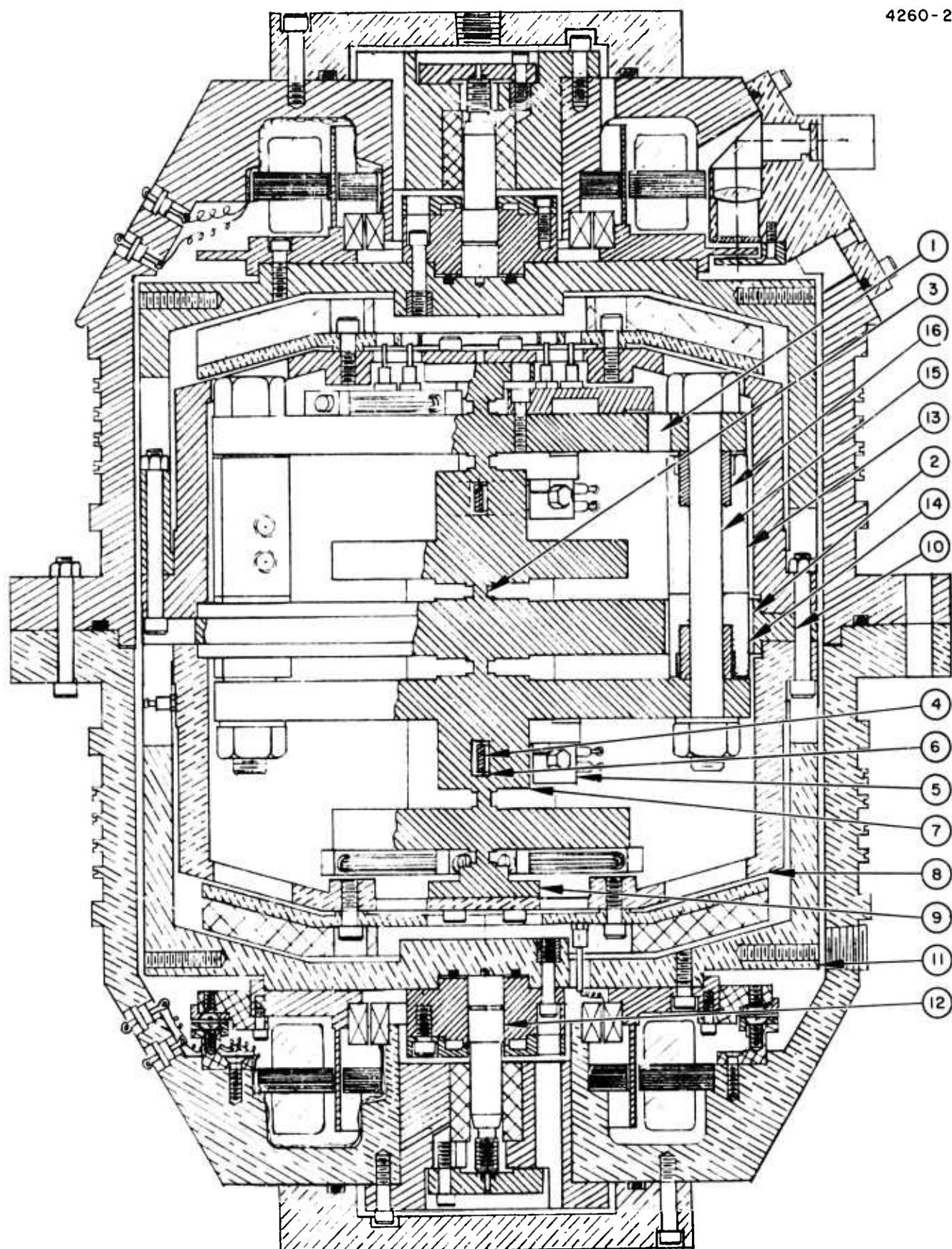


Fig. II-A-2-2. RGG Sectional view.

In order to be able to assemble the end masses through the end mass cutouts in the Central Plate, the end masses were made in two pieces. Typically, the "inner" piece (No. 14) is nested in the end mass cutout, and then the "outer" piece (No. 13) slides in place. The end masses are fastened in place to the sensor arms by one 5/16 in. diameter beryllium-copper bolt (No. 15).

The end masses contain aluminum inserts (No. 16) which have been inserted by a press fit. Their purpose is to provide an aluminum-to-aluminum material contact at the arm plate-mass interface and an interference-fit interface between the aluminum insert and the end mass. Thus, the inserts reduce the possibility of "walking" of these non-equal expansion coefficient parts when subjected to temperature variations. The length of the aluminum inserts has been designed such that the resulting thermal expansion of end mass material (Mallory 1000), inserts, plus arm plates, is the same as that of the beryllium-copper bolt.

b. Sensing Component Assembly - The assembled sensing components are shown in Fig. II-A-2-3. In this photograph, three of the six pivot diameters are clearly shown (No. 4); they each measure 0.27 cm diameter x 0.318 cm length. The tungsten masses of the upper arm (No. 1) are bolted between the two arm plates of the upper arm (No. 2). The two lower arm plates are shown by No. 3. The Central Plate No. 5 is shown bolted to the lower half of the Inner Rotor (No. 7). The two transducers are not clearly visible, but their general location is shown by No. 6, both top and bottom.

The oblique view of the assembled Sensing Components, Fig. II-A-2-4, shows more clearly how isoelasticity of the arm plates is achieved. Material has been removed in each Arm Plate (No. 1) to intentionally weaken the structure. The ends of the pivot column terminate in flanges (No. 3) which are bolted to the Inner Rotor halves. Balance of the structure is attained by balance screws and the balance tubes (No. 2). Arrow No. 4 points to a large radial screw and No. 5 to a small tangential balance screw.

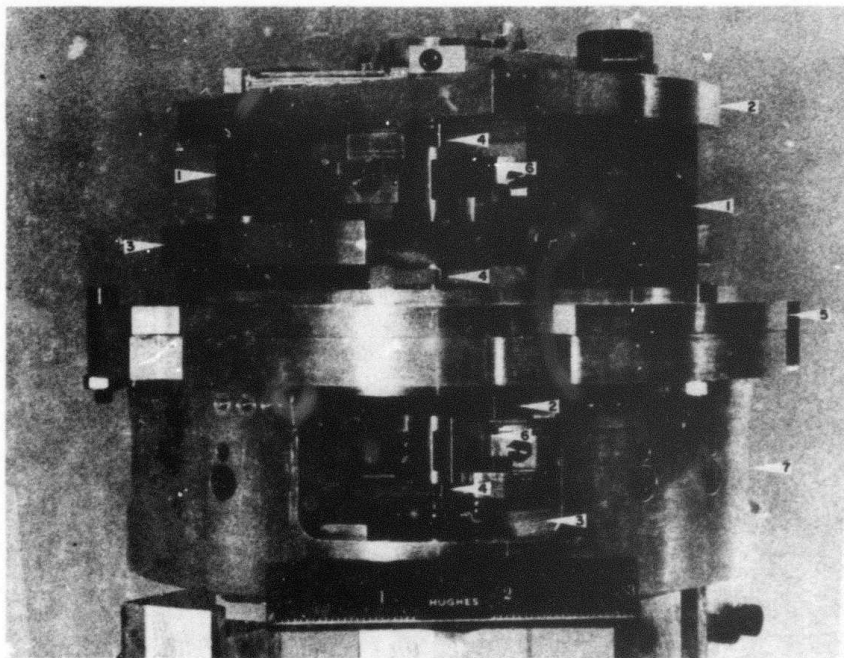


Fig. II-A-2-3. Assembled sensing components.
(Mounted in lower half of inner rotor)

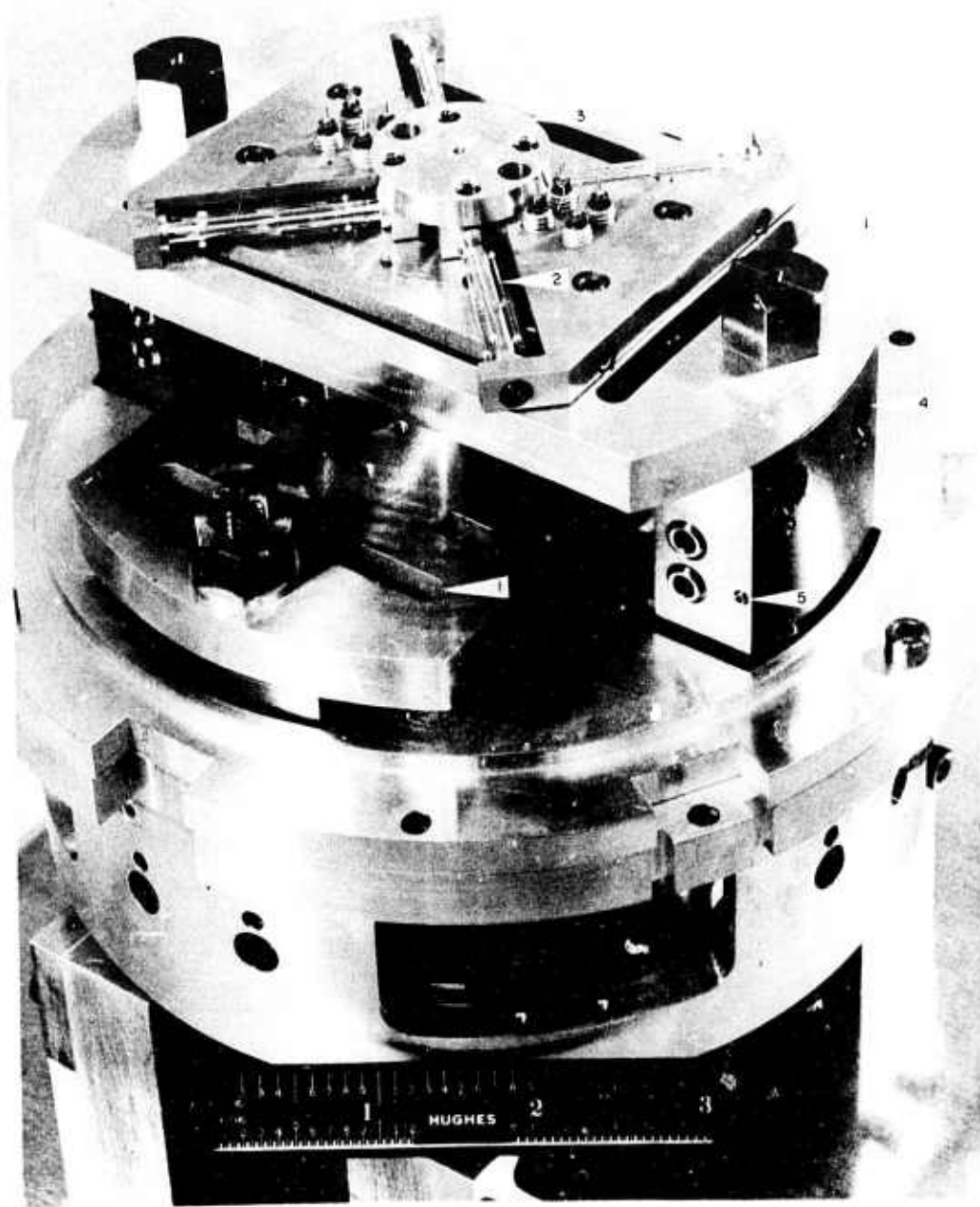


Fig. II-A-2-4. Assembled sensing components.
(Oblique view)

3. RGG System Electronics

The RGG system electronics are divided into two groups:

- External (rack or sensor mounted)
- Rotating (located on the Inner Rotor)

The system block diagram is shown in Fig. II-A-3-1 and the external electronics are shown in the photograph, Fig. II-A-3-2.

a. External Electronics — The system block diagram shown in Fig. II-A-3-1 is useful for this discussion.

The reference element for the whole system is the high precision 10 MHz clock. It is stable to one part in 10^9 and accurate to one part in 10^7 . An eight slot optical encoder disc on the RGG Rotor provides the Rotor-to-Stator position reference. The operator sets the computer to the desired number of 10 MHz counts per octant and the computer reads the number of counts actually received. The computer computes an error signal that is converted to an analog error signal, approximately 140 times per second, and this signal goes to the speed control servo. The computer also corrects the apparent position of each slot in the encoder disk. Errors which occur in the manufacturing of each slot require that each slot position be electronically repositioned.

Final tests on the speed control servo can not be made until precision spin bearings are installed in the RGG, however, all tests made to date indicate that the speed control subsystem is within specification.

Power for the rotating electronics is provided by an external rf power supply, ~500 kHz. This supply can be interrupted by the data injector and logic state commands thus provided to the electronics.

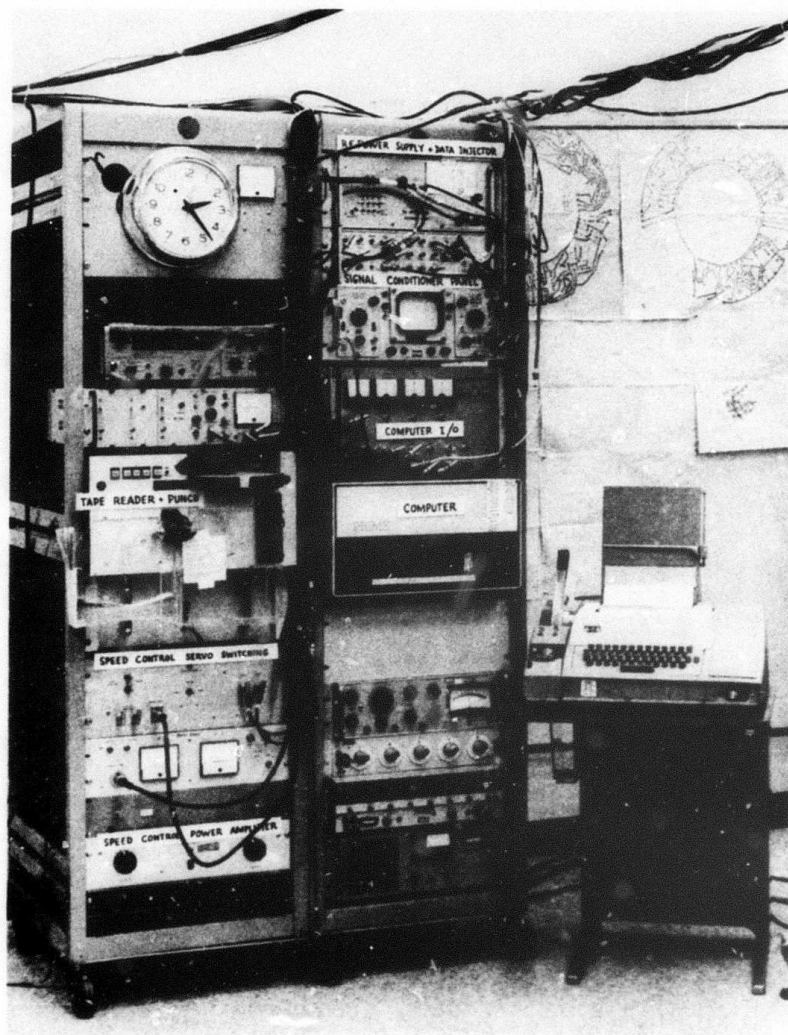


Fig. II-A-3-2. RGG External electronics.

Digital Minicomputer
Tape Reader and Punch
Frequency Standard and Counter
Signal Conditioner
Power Supplies
Speed Control Servo
Teletype Printout

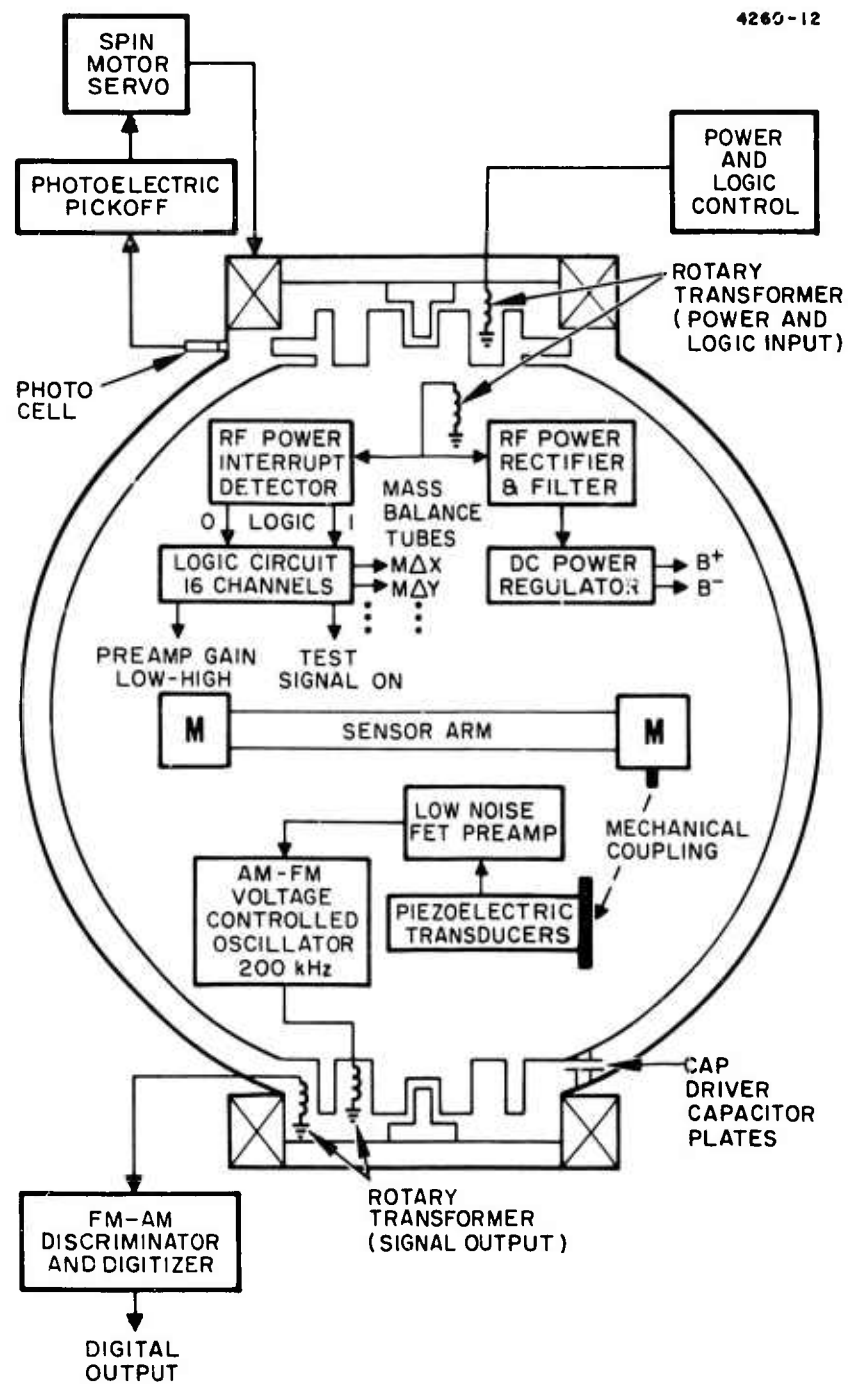


Fig. II-A-3-3. Rotating electronics functional schematic.

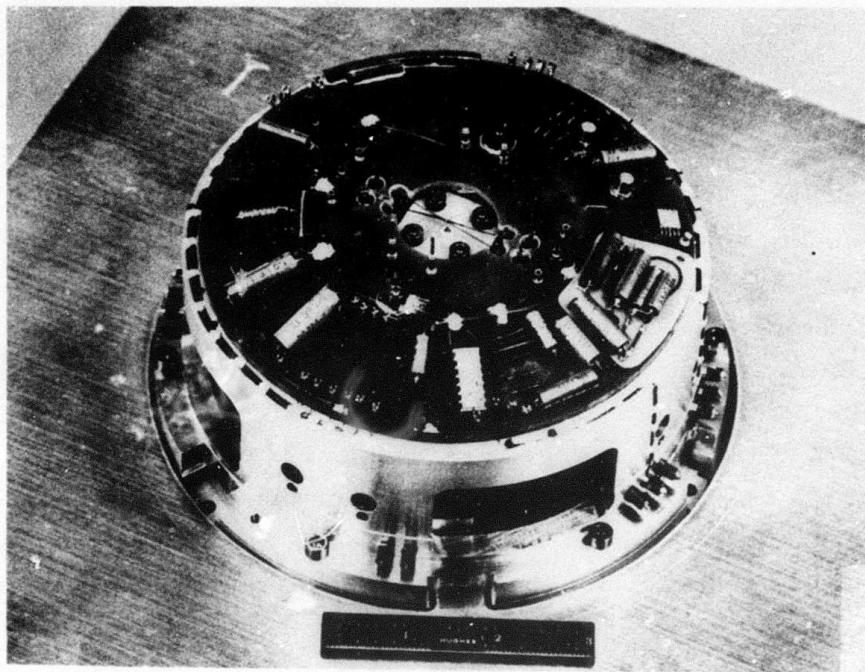


Fig. II-A-3-4. Power Supply, Logic Circuits, and Test Circuits (internal voltage and temperature).

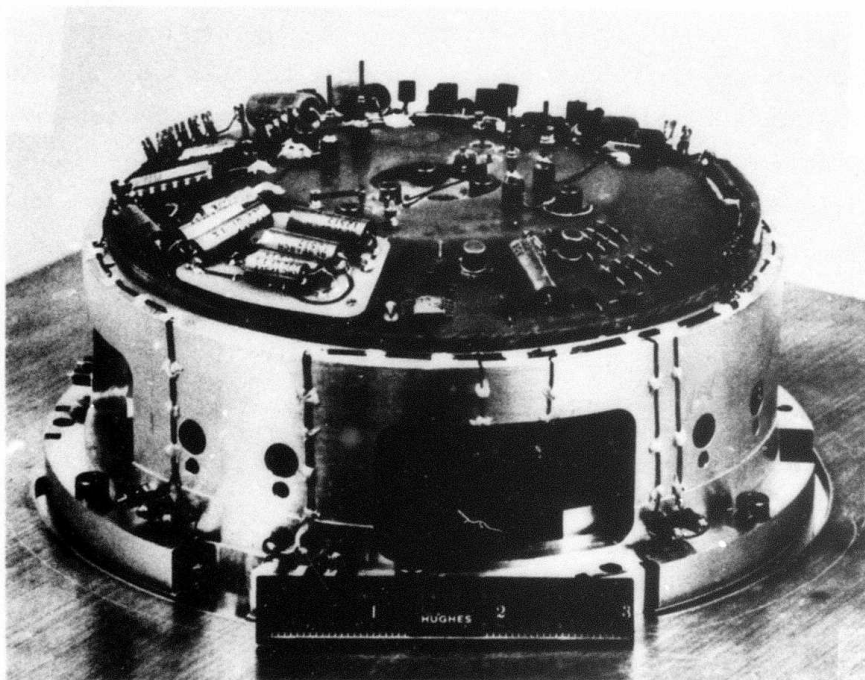


Fig. II-A-3-5. Preamplifier, AM-to-FM modulator and Filter.

Also included in the external electronics is the temperature control which maintains the sensor temperature to 45 ± 0.0006 °C.

A "Signal Conditioner Panel" is included with the external electronics although it is not actually a part of the system. It generates regulated square wave and sine wave test and reference signals at 1, 2, 3, and 4 times the Rotor speed. All of these are precisely phase-locked to the rotor encoder disk position.

The rotating electronics generate an FM signal that is proportional to the gravity gradient signal acting on the sensor. The computer counts each cycle of this signal and stores the count generated during each octant. The computer then time averages these octant counts, converts them to an equivalent E. U. and causes the teletype to print the cosine and sine E. U. terms.

An example of a computer printout, dated February 25, 1975 at 11:39 a.m., is shown in Fig. II-A-3-6. Particulars about this test (test number 16) have been entered manually on the teletype to document certain specific conditions of this test. The page heading, printed by the computer, contains information about the encoder disk slot corrections (M1 through M8), balance tube gap location information for each arm and date of last gap movement, the selected rotor speed and two omega frequency (35.6379 Hz), as well as gain and servo information. Seven column headings were printed before the actual test was started. In this example, five lines of 2ω data, each averaged over a time period of 245 revolutions, were recorded. The values of the cosine, sine and signal magnitude are recorded in Eötvös Unit values and the phase angle data is recorded in degrees. At the bottom of the page, the five lines of sine, cosine, magnitude and phase angle data have been averaged and the standard deviation values recorded. In this example, the particular test conditions produced an output of 5813 E. U. (bias) at a phase angle of -156.2 degrees, with a variation of 31.6 E. U. (noise).

*ROTATED SENSOR TO K UP POSITION

=

TNO 16

=

*TEST COND 6A I NO K UP J WE HORIZ ANG 10.00 MV -25 DEG

*SPEED OK

HEA

```

2,25,75 11:39 TNO 16 BIAS -92.0000 0.0 0.0 0.0000
M1-M3= 68. 103. 53. 68. 13. 1. 10. 33.
ARM1 0.5000 0.5000 ARM2 0.5000 0.5000 TU-FAC 0.
LAST BAL 12, 8,73 11:52. SPEED 561200.00 0.10 2W = 35.6379
SERVO 0.010 0.950 GAIN 11.34619 FAC 0.0937300
2W AVE
COND COS SIN MAG PHA FM-CAR OCT.PER
2W245 -5349.5 -2317.6 5830.0 -156.6 265697.5 4629
2W245 -5330.4 -2339.4 5821.2 -156.3 265700.3 4613
2W245 -5345.0 -2352.8 5839.9 -156.2 265700.9 4648
2W245 -5300.6 -2365.1 5804.3 -156.0 265699.6 4611
2W245 -5277.9 -2341.3 5773.9 -156.1 265695.9 4643

2W AVE 5=N -5320.7=C -2343.2=S 27.69=SC 15.24=SS
5813.8=MAG 31.61=SMAG -156.2311=PHA

```

Fig. II-A-3-6. Example of computer printout.

b. Rotating Electronics — The rotating electronics functional block diagram is shown in Fig. II-A-3-3. The rf power comes in through a rotary ferrite transformer and is rectified, filtered and precisely regulated to provide + and - 10.000 volts dc. The rf power input can be interrupted on a logical basis. Inside the sensor these interrupts are converted to a 16-bit logic state. These logic states program a selectable amplifier and adjust the mass balance of the sensor arms by means of electrolyte mass transport balance tubes. Piezoelectric transducers measure the instantaneous differential sensor arm motion. The resistive load across the output of the transducer controls the mechanical Q of the sensor. The transducer output is amplified by a balanced pair of low noise field effect transistors, amplified and passed through a tuned filter. The next stage is an amplifier that can output any of four selected inputs. The output signal is selected by logic states determined by interrupts in the rf power.

The logic control provides for the following outputs:

- Sensor Output Normal Gain
- Sensor Output Low Gain
- Regulated DC Voltage Monitor
- Rotor Temperature Monitor
- Test Signal Insertion Capability

The output of the selectable amplifier drives a voltage controlled oscillator with midfrequency of about 250 kHz. Thus, a signal is converted to a frequency deviation and an FM output is obtained. This FM is transmitted outside the sensor through another rotary transformer.

c. Conclusion — Each group of electronics, although straightforward in concept, has required pushing the state-of-the-art in several areas. In spite of these difficulties, the electronics system has progressed steadily from concept, to detailed block diagram, to circuit design, to hardware and finally to system performance tests. Since inception, only minor changes and adjustments have been required to the final hardware.

A few of the more notable electronic accomplishments include:

- Control of the Rotor speed so that the angular position of the Rotor is known at any instant to ± 2.4 arc-seconds. (The Rotor is rotating at a nominal speed of 2.4 arc-seconds per 100 nanoseconds. Control is accomplished by use of a precision time source, precision optics and an on-line digital computer.)
- Adjustment of the mechanical Q of the sensor to a stable controllable value. (Accomplished by electrical loading of the mechanical to electrical piezo-electric transducer.)
- Supply of continuous electrical power to the rotating electronics without introducing torque noise. (Rotary ferrite rf transformers.)
- Conversion of a 4500 E.U. Signal (0.025 dyne-cm) into a usable output, resolved into two channels, each accurate to one part in 10^5 . (Precision optics, transducers, amplifiers, and digital computer demodulation of an FM signal.)
- Control of the sensor temperature to a specified temperature in the range of 43 to 49°C to 0.0006°C. (This has not yet been proven, since the existing temperature control is better than the best available monitor.)

B. Mechanical Assembly of Sensor

Installation of the various piece parts of the RGG in a logical sequence of steps to result in a properly aligned, assembled unit was a major task. This task was significant both in terms of the required planning and in the assembly effort. The nature of the RGG design is such that one starts from the innermost element and "builds" his way out. Thus, a nominal amount of planning is necessary merely to assure that access is continually available to mount the next part. Furthermore, because of the delicate nature of the unsupported Arm-Pivot unit, much effort was given to handling and providing holding or assembly fixtures. Also, because of the extremely small clearance of the spin bearings, considerable thought was given to the assembly procedure and fixture design to prevent binding or galling of the bearing mating surfaces during assembly.

The first building block of the RGG is the Arm-Pivot. During manufacture of the Arm-Pivot, ultra precision machining spacers were fabricated and installed between the outer and inner arm plates and between the inner arm plates and the Center Plate. These spacers were required because the various pivots were turned down to final diameter. The first items to be installed are the end masses. To install the end masses, the Arm-Pivot, with machining spacers still in place, was set in a holding fixture, which supported inner arm No. 1. The short end masses were set in their proper positions, then the long end masses were slid into place. The mounting bolts were then installed, the washers and nuts added and hand tightened. Then the machining spacers mounted between the two plates of arm No. 1 were removed. After their removal, the end mass bolts were tightened. The amount of tightening was judged by producing a stretch in the bolt of 0.004 in. which corresponds to a stress of about 20,000 psi and a tension of 1500 lb. At this point, the unit was turned over and the second set of end masses installed in a similar manner. Then the preassembled balance tube mounts were installed.

The next step was to install the Inner Rotor halves. A special holding fixture was required to support the Inner Rotor at its center flange while allowing access for the six screws which fasten the two Inner Rotor halves and the Center Plate of the Arm-Pivot together. After installing and torquing these six bolts to a prescribed torque level of 24 in. -lb, the four screws which fasten each Arm-Pivot end flange to the Inner Rotor halves were installed and torqued down.

Installation of the transducer mounts and the transducer leaves proceeded next. This installation was quite tedious due to the relatively difficult access to some of the mounting screws. The electronic circuit boards were then mounted to the ends of the Inner Rotor halves. Then, the interconnecting wiring between the top and bottom circuit boards, the transducer, and the balance tubes were installed and checked. The unit was then placed in the vibration test stand while the sensor error sensitivity adjustments were made as described in Section IV-D.

The next assembly step was to attach the Outer Rotor halves. Since each half is held in place with only three screws, this step is relatively simple. It is necessary to install all six screws at first due to limited access, however. These screws are held by a specially designed differential screw thread to permit precise adjustments of screw tension (for skew axis alignment adjustments).

After installation of the Outer Rotor halves, the spin motor drag cups, encoder disk, rotating cap driver plate and the female portion of the spin bearings were mounted.

Ball bearing type spin bearings were first mounted in the sensor to reduce the risk of damage to the hydrodynamic oil bearings, while the rotor subsystem was first subjected to the static and dynamic balancing steps.

Dynamic balancing of the RGG rotor was accomplished by mounting the completed sensor on a test fixture so that it was free to translate in the horizontal plane containing the spin axis. Two geophones were mounted, one at each rotor balance plane node points with their input axes perpendicular to, and in the horizontal plane of, the sensor spin axis. The phase and magnitude of each geophone output signal

was measured with reference to the sensor encoder disk position. This signal was a direct measure of the magnitude and rotor location of the change required in the balance plane adjustment masses. This equipment allowed the rotor to be balanced to the equivalent of about 1 μ -in. for a free rotor.

During the foregoing assembly operations, the Stator halves were prepared for assembly. This effort included mounting and bonding in place, using special assembly fixtures (1) the spin motor windings and back-up lamination stacks, (2) the stationary portions of the rotary transformers, (3) the stationary cap driver plate, and (4) the vacuum-sealed electrical feedthroughs. All interconnecting wiring was then installed to the feedthroughs and soldered to connector terminals on the outside of the Stator halves. Then, the heater and temperature sensing elements were mounted, bonded down, and connected to the connector terminals. After this, the Rotor subsystem and the two Stator halves were ready for assembly with the spin bearing pintles.

This process, as mentioned earlier, required the use of several special fixtures to maintain precise alignment of the bearing components during assembly. First, the lower Stator half was mounted on a fixture which fits through the 1-5/8 in. diameter pintle holder hole in the end of the Stator. This fixture has a centering hole 1-1/2 in. in diameter which, when the Rotor is lowered in place, centers the lower bearing in its Stator. With this fixture installed, the Rotor was lowered in place. The O-ring gasket was installed and the upper Stator half positioned in place on the lower Stator half and the two halves bolted together with the twelve 8-32 beryllium copper screws and nuts. Then each was torqued to a level of 24 in-lb.

The next step was to install the upper bearing pintle in its pintle holder. This was accomplished using a special puller fixture to pull the pintle into the carbon sleeve in the pintle holder. Next, three guide rods were placed in the pintle holder hole in the end of the upper stator. These three guide rods are machined to a precise thickness. They fit between the o.d. of the female (rotor mounted) bearing (1-1/2 in. o.d.) and the i.d. of the pintle holder hole. These rods,

then, center the rotor bearing in the Stator. The lubricant was then added to the bearing and the upper pintle and pintle holder was lowered into place. (The pintle holders have three equally spaced axial slots which provide clearance for the guide rods.) The guide rods were removed and the upper pintle holder was then fastened in place with its six mounting screws.

Next, the assembly was turned upside down. The first centering fixture was removed, after first installing the guide rods. (This fixture also has three axial slots which provide clearance for the guide rods.) Then the second bearing was lubricated and its pintle and pintle holder installed in a similar manner. This completed the assembly of the Rotor into the Stator.

Next the axial position of the Rotor relative to the Stator was adjusted to provide 0.005 in. clearance for the cap driver plates. This is accomplished by sliding the pintle on the cap driver end of the sensor in its carbon sleeve. Once positioned, a special pintle spacer washer was machined and installed which permanently positioned this pintle axially. Then, the second pintle is positioned in a similar manner.

The position of the second pintle in its carbon sleeve is adjusted to set the end clearance of the two bearings. This adjustment is accomplished in two steps. First, it is adjusted to allow approximately 0.002 in. end shake, i.e., 0.001 in. clearance for each bearing. This clearance is measured by means of a special eddy current proximity probe which is temporarily mounted in the Stator. This unit "looks at" the end surface of the Rotor and provides a calibrated displacement measurement. By making a measurement with the sensor spin axis vertical and then making another measurement with sensor inverted, the end shake can be measured.

After the initial 0.002 in. end shake is set and the photocell and light source installed, the RGG sensor is then run up to speed, evacuated, thermally stabilized, and the end shake remeasured. Finally, the end shake is readjusted to 0.0005 in. for permanent operation.

The foregoing description will provide the reader with some insight into the forethought and care that was required to successfully accomplish the assembly process.

C. Error Analysis Summary

A detailed error analysis, conducted during the first year of this contract, ranks as one of our most important early accomplishments. The writeup on this subject was published in the January 1973 R&D Design Evaluation Report and in Semiannual Report Number Two, February 1973. The findings revealed many error sources unidentified prior to 1972. The error mechanisms were studied in detail. All the known error contributors were then tabulated and evaluated both individually and in relation to each other. Both sensor and system aspects were considered. Limits were put on the amount that each potential source should contribute in order to stay within our desired goal. Thus, the original error analysis served as the basis for almost all of the subsequent system and component design and development work.

Table II-C-1 tabulates our 1973 estimate of the contribution of the error sources to each tensor element of a complete gravity gradient measuring system. Such a system is composed of both the RGG sensor and the Vibration Isolation, Alignment and Leveling System (VIALS).

Figure II-C-2 provides a graphic portrayal of our most recent (1975) worst-case error estimates. Because of sensor design modifications, some of the values have changed slightly from our earlier estimate. Also, two error sources, "skew axis misalignment" and "dynamic mass unbalance," have been discovered and added to our 1973 list. A discussion of each of the presently known error contributors is included as Section IV-D of this report.

The RSS total, 0.7 E. U. at 10 s, shown in Fig. II-C-2, provides continued confidence that the RGG Sensor and System are estimated to perform within our desired goal.

TABLE II-C-1

RGG Prototype Design System
Error Summary
(1973)

Error Sources	Gravity Gradient Tensor Element Errors, 1σ					
	σ_{XX}	σ_{YY}	σ_{ZZ}	σ_{XY}	σ_{XZ}	σ_{YZ}
<u>RGG Errors</u>						
Thermal noise	0.338	0.338	0.338	0.358	0.358	0.358
Arm mass unbalance	0.218	0.218	0.218	0.231	0.231	0.231
Sum mode mismatch	0.093	0.093	0.093	0.098	0.098	0.098
Scale factor	0.150	0.150	0.212	0.045	0.002	0.002
Phase Errors	0.003	0.003	0.003	0.033	0.325	0.325
Rotational field	0.027	0.027	0.027	0.028	0.028	0.028
Anisoelastic	0.017	0.017	0.020	0.014	0.010	0.010
RSS of RGG Errors	0.441	0.441	0.465	0.442	0.547	0.547
<u>VIALS Errors</u>						
Arm mass unbalance	0.036	0.036	0.036	0.038	0.038	0.038
Rotational field	0.086	0.086	0.086	0.079	0.079	0.079
Anisoelastic	0.069	0.069	0.135	0.016	0.011	0.011
Platform orientation	0.368	0.368	0.212	0.352	0.327	0.327
RSS of VIALS Errors	0.386	0.386	0.286	0.377	0.339	0.339
RSS of RGG and VIALS	0.586	0.586	0.546	0.581	0.643	0.643

RSS TOTAL: ≈ 0.7 EU AT 10 sec

2704-29R1











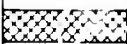


ERROR MECHANISM	EÖTVÖS UNITS			MAIN SOURCE
	0.1	0.2	0.3	
THERMAL NOISE				SENSOR/XDCR
RESONANT FREQUENCY				SENSOR/XDCR
SKEW MISALIGNMENT				SPIN BEARING
SCALE FACTOR				ELECTRONICS
AXIAL VIB TORSION				SPIN BEARING
DYNAMIC MASS UNBALANCE				SPIN BEARING
SPEED CONTROL SERVO				SPIN BEARING
DIGITALIZATION ERROR				ELECTRONICS
PRIME ANISOELASTICITY				VIALS
DIFF MASS UNBALANCE				SPIN BEARING
SUM MODE MISMATCH				SPIN BEARING
ROTATION FIELD				VIALS
CROSS ANISOELASTICITY				SPIN BEARING

Fig. II-C-2. Summary of RGG tensor element error standard deviations (1975).

D. System Considerations

1. Motion Isolation Considerations

Although gravity gradiometers have operated successfully in the laboratory at the sensitivities required for airborne surveys, gradiometer operation in an aircraft is considerably different than that in a laboratory. To isolate the gradiometer measurement system from the various aircraft motions, the instrument package must be mounted on a Vibration Isolation, Alignment, and Leveling System (VIALS). This system must not only provide for isolation from vibration and short-term angular rates, but must also maintain the sensor package orientation despite aircraft roll, pitch, and heading changes so that the gravity survey data can be accurately related to the earth coordinates.

a. Vibration Isolation Requirements -- In their present stage of development, the gravity gradiometer instruments require some isolation from aircraft vibrations. Although gravity gradiometers are not sensitive to linear accelerations to first order, they are sensitive to second order, since the accelerations can couple through the instrument fabrication errors or nonlinearities to produce an erroneous output. The RGG offers a second barrier against these induced errors by separating the frequency of the gravity gradient signal, which appears at twice the rotation frequency, from the majority of the acceleration-induced error signals, which appear at the rotation frequency. Nevertheless, even for the RGG, the aircraft vibrations (especially those at one and three times the rotation frequency) must be attenuated to a level where they can be rejected by the sensor processing electronics. The specifications for the vibration isolation system and stable platform are given in Table II-D-1-1.

b. Alignment and Leveling Requirements -- Another gravity survey system source of error that must be controlled by the motion isolation system is the effect of erroneous signals generated by an error in the alignment or leveling of the gravity gradiometer instrument package. A misalignment error couples into the background

TABLE II-D-1-1

Isolation Platform Specifications

ANGULAR FREEDOM		
Pitch and Roll	$\pm 30^{\circ}$	
Azimuth	Full freedom	
READOUT ACCURACY		
± 1 arc-min (± 0.3 mrad)		
INITIAL ALIGNMENT (1σ)		
Vertical	0.015° (250 μ rad)	
Azimuth	0.03° (500 μ rad)	
ANGULAR DRIFT (1σ) (10-h maximum)		
Vertical	0.003° (50 μ rad)	
Azimuth	0.03° (500 μ rad)	
ANGULAR OSCILLATION (any frequency)		
Maximum Amplitude	0.003° (50 μ rad)	
Integrated Angular Rate	$2^{\circ}/h$ (10^{-5} rad/sec)	
VIBRATION ATTENUATION SYSTEM		
Type: Six degree of freedom linear second order system		
	Natural Frequency	Damping Ratio
Translation (each axis)	1.0 Hz	0.4
Rotation (each axis)	2.5 Hz	1.0

gravity gradient bias of the earth to produce an erroneous output. This error, of course, occurs with any gravity gradiometer instrument package. For an example here, however, let us examine the effect of alignment errors on the RGG that measures the difference in the gravity gradients in the plane of rotation of the sensor. An RGG with a vertical spin axis in a region where no anomalies exist should have a zero output, since the background gradient of the earth (-1500 E. U.) is uniform in the horizontal direction. However, if the isolation system is tilted with respect to the horizontal, then a portion of the vertical gravity gradient of +3000 E. U. will couple into the supposedly horizontal gravity gradiometer, thus producing an erroneous signal that indicates a gravity anomaly in the direction of the misalignment.

For an RGG with a horizontal spin axis in a region with no anomalies, the background bias signal of $+3000 - (-1500) = +4500$ E. U. should be in the signal channel associated with the vertical-horizontal direction. If the platform is not level, a portion of this signal will show up in the quadrature phase, indicating a gravity anomaly at 45° .

The angular orientation error sources require that the isolation system have sufficient accuracy in leveling and pointing so that these errors are reduced below the other error sources. For geophysical prospecting, a high-quality camera platform might be acceptable; for military gravity survey systems, however, requirements dictate that the platform have inertial grade performance. Unfortunately, there is no inertial quality platform that can carry the weight of a three-gradiometer package in addition to its normal complement of gyros and accelerometers. For the military gravity survey system, then, a new gimbal system is needed that carries the weight of the gradiometer instrument package.

c. Angular Motion Requirements — A major concern with the motion isolation requirements for a gravity gradiometer survey system is the need to attenuate angular rates. Although gravity gradiometers are not sensitive to linear accelerations, they are sensitive to rotational angular rates. In the RGG, the torque response

of the sensor is a function of not only the gravity gradient, but also any angular rates that may be present. For an RGG spinning in the xy plane, the torque (ΔT) in the arms results from the gravity gradient terms (Γ_{xx} , Γ_{yy} and Γ_{xy}) and the angular velocity rates (Ω_x , Ω_y):

$$\Delta T = \frac{ml^2}{4} \left[(\Gamma_{yy} - \Gamma_{xx} + \Omega_y^2 - \Omega_x^2) \sin 2\omega t + 2(\Gamma_{xy} - \Omega_x \Omega_y) \cos 2\omega t \right] .$$

It is important to note in the above equation that it is the product or square of the angular rate that causes the angular rate sensitivity problem. Thus, if the disturbance were in the form of a sinusoidal jitter, at any frequency, it would be rectified by the square-law response of the sensor and would produce an error signal. Thus, the effect of angular rate on the RGG must be calculated by integrating the angular rate disturbances over the entire frequency spectrum. For example, since our goal is a 1 E. U. sensor, the integrated angular rate spectrum should not exceed $\Omega = 3 \times 10^{-5}$ rad/s. It is seen that the error signal produced by this rate would be

$$\Omega^2 = 9 \times 10^{-10} \text{ sec}^{-2} = 0.9 \text{ E. U.}$$

Because the angular rate sensitivity is independent of the frequency of the angular rate, care must be taken to identify and eliminate even the apparently negligible (very small) high-frequency angular rates. Unfortunately, conventional platforms are known to be capable of introducing high-frequency angular rates while removing the low-frequency angular rates induced by the aircraft. The slip-stick friction of ball bearings in conventional platforms cause this noise. Although no quantitative data have yet been available on these high-frequency angular rates, we have estimated that a typical inertial grade platform (with ball bearing gimbals) can produce an integrated

angular rate spectrum amounting to several E. U. s. Thus, in addition to a gimbal system capable of supporting the RGG payload, a platform employing bearings other than ball bearings is needed.

The VIALS studies permitted under this contract were very limited. This aspect of the work was terminated in 1972 when it was satisfactorily shown that the platform requirements can be achieved with state-of-the-art hardware. No design work, no quantitative measurements with existing platforms, and no vendor surveys have been done since that time.

2. Survey System Considerations

At this point in our design work, we are far from having a complete design for a gravity gradiometer survey system; however, we can outline its general characteristics. A configuration for the gravity gradiometer instrument package is shown in Fig. II-D-2-1. The vertically oriented spin-axis gradiometer is on top the stable element of the platform together with the platform gyros, accelerometers, and electronics. The other two gradiometers are hung from below. The six-legged vibration isolation system is one of many that have been considered and could be used to decrease the aircraft vibration level reaching the platform. The platform uses a three-axis, air-bearing, gimbal platform. Again, this is just one of many designs being considered. For example, the three-axis gimbal system could be replaced with a single hemispherical air bearing similar to that presently undergoing flight tests in the NASA/Ames airborne telescope program.

The gravity gradiometer instrument package is, of course, only one portion of a complete survey system. As shown in Fig. II-D-2-2 and II-D-2-3, considerable data monitoring and recording equipment is necessary in a full survey system to ensure that the gradiometer data and navigation information are collected in a coordinated manner for later processing and preparation of gravity contour maps. Airborne geophysical prospecting, of course, is a well-developed field now, and

the development of a complete gravity gradiometer mapping system will be left to those more familiar with its requirements. Our view is that the only perturbation the gravity gradiometer will introduce is that caused by the data processors learning to work with tensor data rather than scalar or vector data.

2045-18

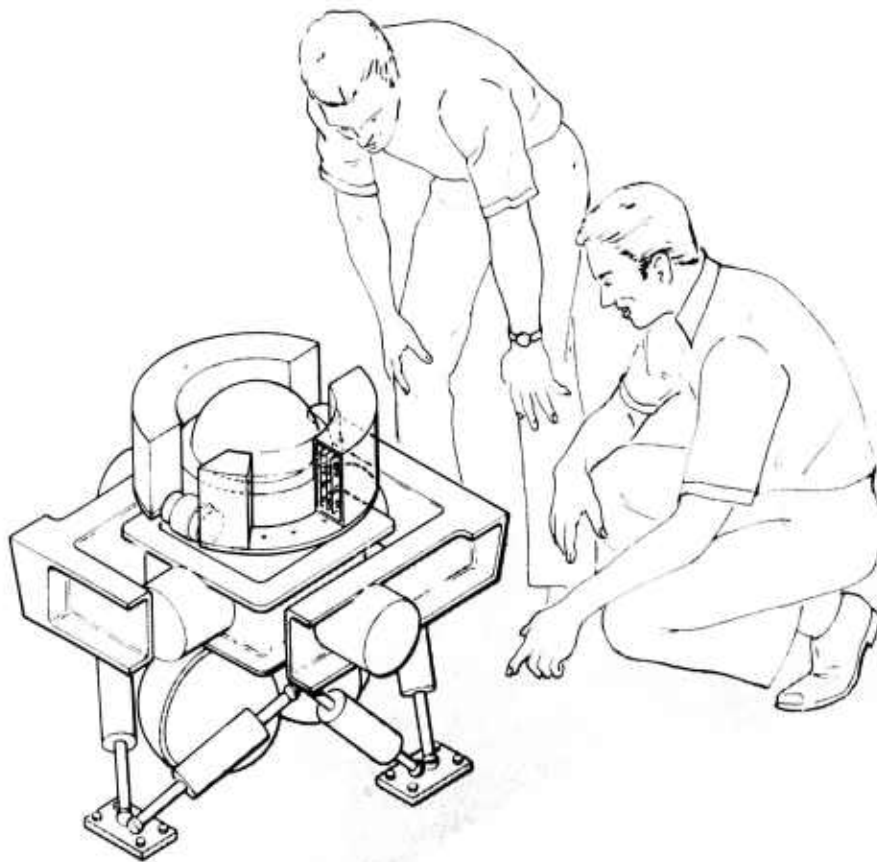


Fig. II-D-2-1. Three-axis air bearing stabilized platform.

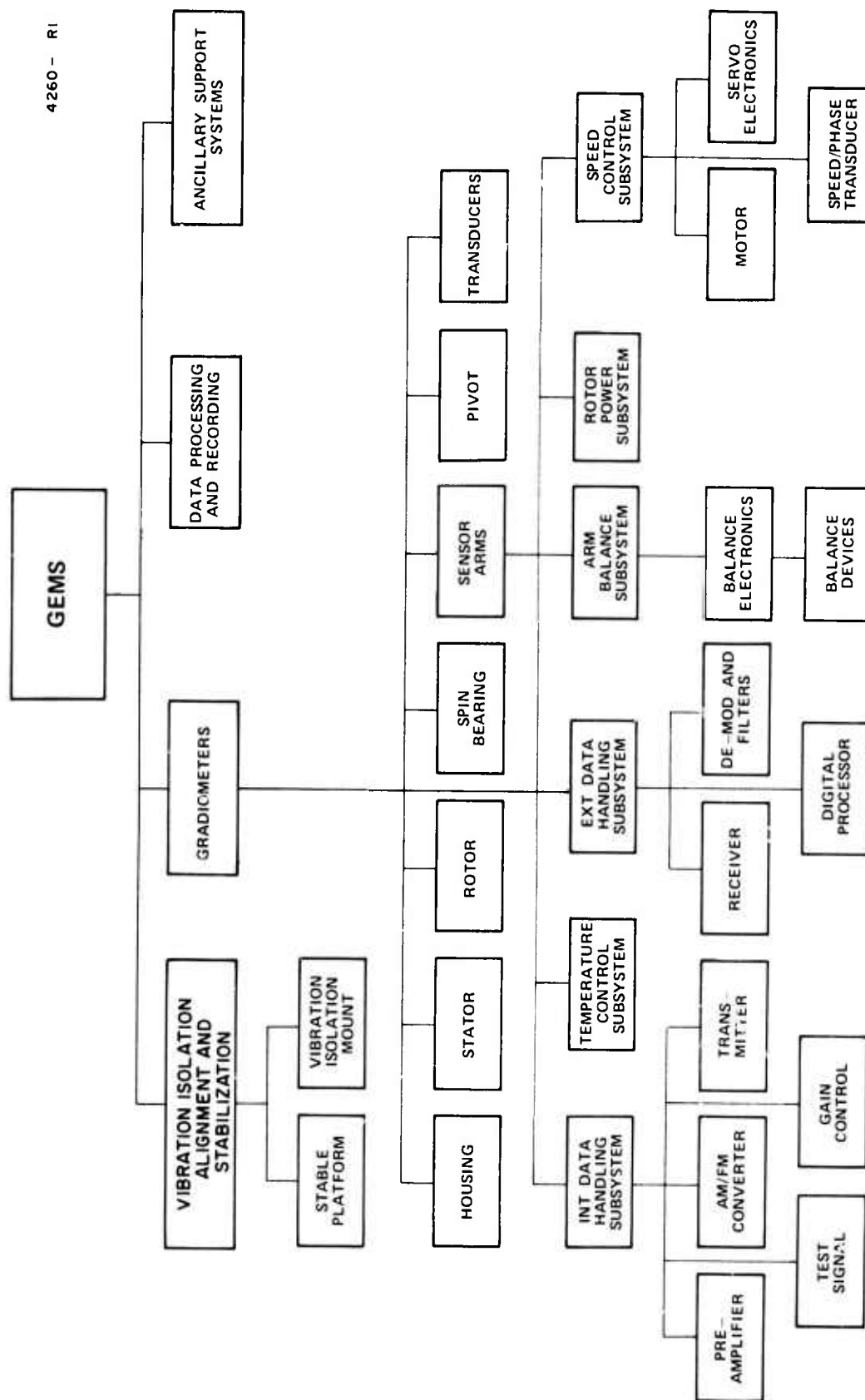


Fig. II-D-2-2. Gravity environment measuring system (GEMS).

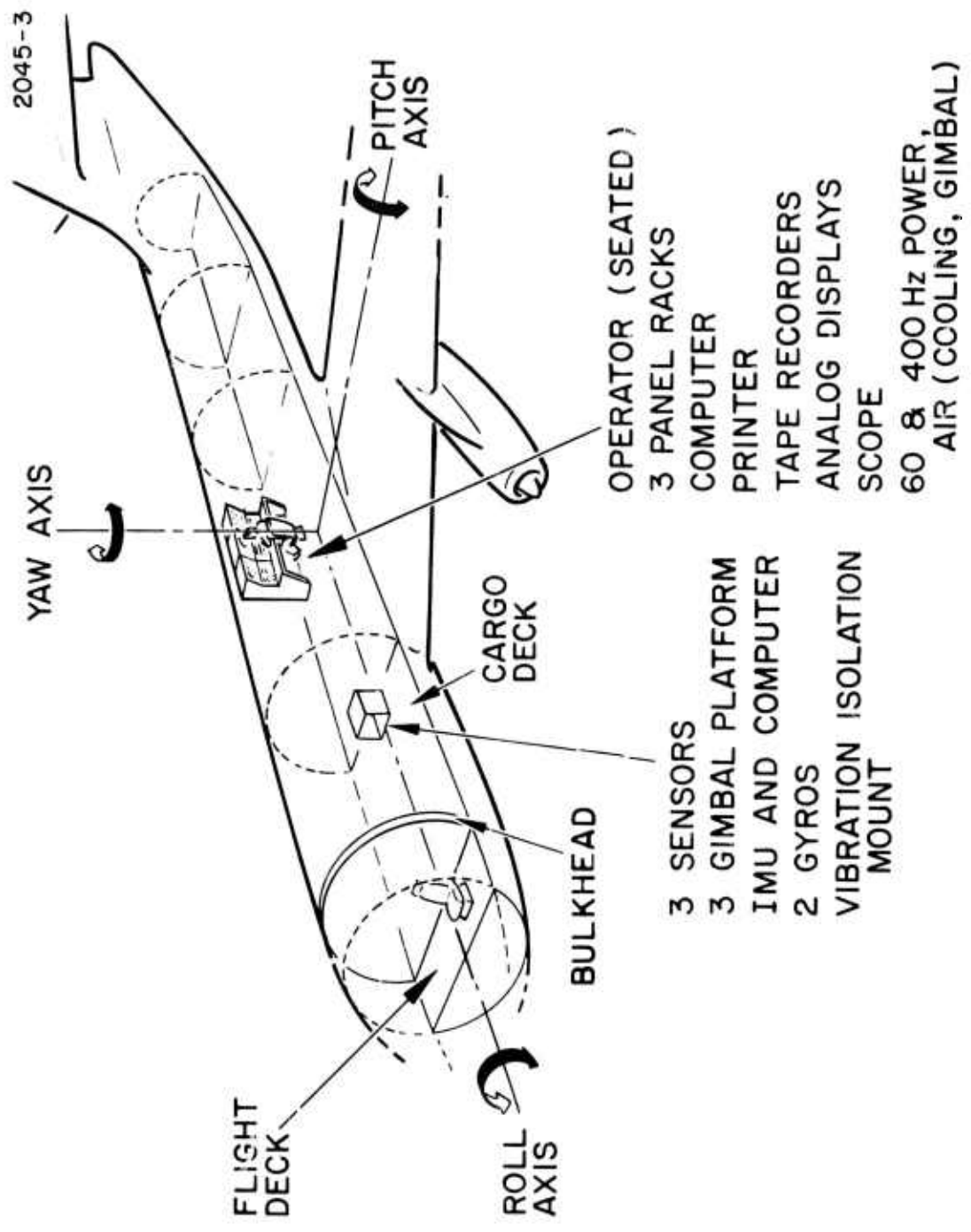


Fig. II-D-2-3. Airborne gravity gradiometer mapping system.

III. SUBSYSTEM PERFORMANCE

A. Spin Bearings

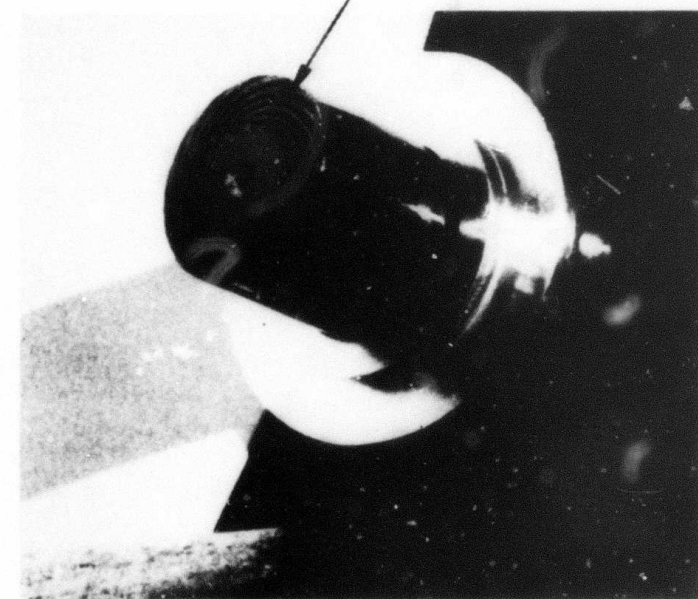
The hydrodynamic oil spin bearings (see Fig. III-A-1) for the RGG were fabricated, tested, and delivered by the spin bearing subcontractor, Shaker Research Corporation, Ballston Lake, New York in July 1974. Many of the specification goals for the spin bearing development were known to be pushing the limits of bearing fabrication technology. Accordingly, the contract was written on a "best effort" basis. Nevertheless, as is shown in Table III-A-1, the delivered bearings met most of the specification goals.

TABLE III-A-1

Spin Bearing Parameters	Goal	Achieved
Load Capacity	>6.8 kg	7.7 kg (min)
Breakaway Torque	< 5×10^5 dyn-cm	4.1×10^5 dyn-cm
Running Torque	< 5×10^4 dyn-cm	3.6×10^4 dyn-cm
Stiffness (Radial)	> 2×10^{10} dyn/cm	2.4×10^{10} dyn/cm
Stiffness (Axial)	> 1×10^{10} dyn/cm	7×10^{10} dyn/cm
Friction Power Loss	<0.5 W	0.4 W
Runout, Total	<1.5 μ -in.	1.5 μ -in.
Runout, Second Harmonic	<1.5 μ -in.	0.5 μ -in.
Runout, Third Harmonic	<0.25 μ -in.	0.3 μ -in.

1. Vacuum Operation

At the time when the RGG spin bearings were released for manufacture, the RGG design configuration was such that the bearings would be exposed to ambient air pressure. Subsequently, the RGG design configuration was changed so that the bearings would be exposed to a vacuum. The spin bearing subcontractor was questioned as to the



SPIN BEARING
PINTLE SHOWING GROOVES
FOR HYDRODYNAMIC THRUST
AND JOURNAL BEARING

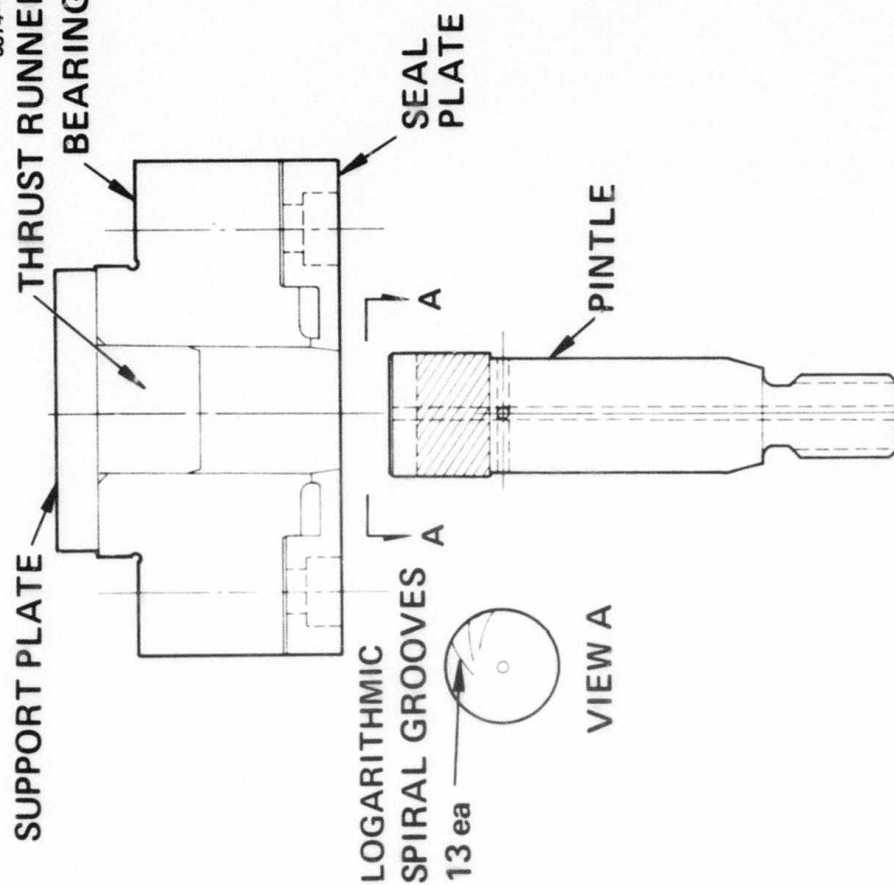
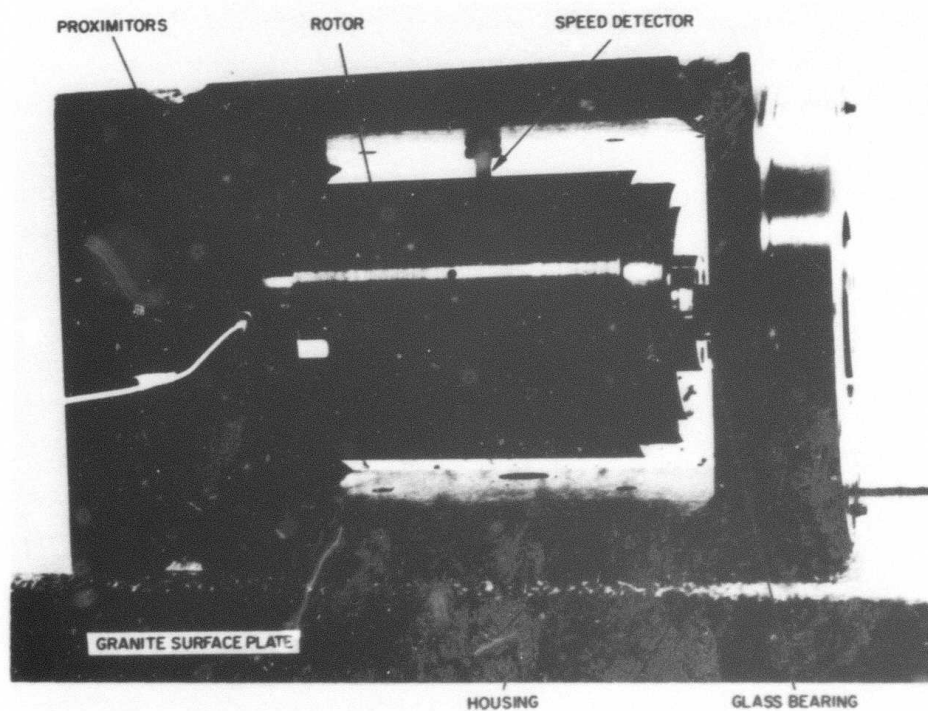


Fig. III-A-1. RGG cylindrical hydrodynamic oil spin bearing.



2. Filling and Vacuum Test

Somewhat later in the program, Hughes personnel conducted some brief experimentation aimed at determining a satisfactory method of filling the bearings with lubricant for vacuum operation. This effort occurred in March 1975, just prior to assembly of the bearings into the sensor. At that time, the project schedule was under great pressure to meet the contract goal to have the sensor rotating and operating by early April. Because of the schedule demands, tests were conducted by three different project personnel on a multishift operation. Because the personnel concentrated their attention on the behavior of the glass bearing on the test rig, we failed to properly lubricate the No. 2 bearing at the opposite end of the test rotor. This resulted in a bearing seizure and damage was sustained by the No. 2 bearing.

Attempts to repair the No. 2 bearing were marginally successful. The bearing can never be used as a "good" bearing again, but can be operated in a vertical spin axis orientation on the upper end of the sensor (which does not carry a thrust load) or with the sensor spin axis oriented horizontally.

While repairing bearing No. 2, we developed a filling and evacuation procedure. A ball bearing was substituted in place of bearing No. 2 on the test rig. The procedure was developed by observing operation of the glass bearing on the test rig inside a vacuum jar. It appeared to be successful the first time and was not repeated until later when the bearings were actually installed on the sensor.

3. Bearing Operation in the RGG

Prior to installing the hydrodynamic oil bearings in the sensor, commercial, off-the-shelf, ball bearings were installed temporarily to allow coarse static and dynamic balancing of the RGG rotor. The oil bearings were then substituted and the filling procedure developed earlier was used to fill the bearings. The sensor was then placed with its spin-axis horizontal in the rotor balance fixture for

dynamic balancing. This balancing operation required approximately four hours of intermittent start-stop operation. The bearings appeared to operate properly. The balancing work was done with the rotor and bearings exposed to ambient air pressure.

Upon completion of the rotor balancing, the sensor was placed in the sensor test stand with the spin axis aligned horizontally. The heaters were turned on to bring the RGG up to its nominal operating temperature of 43 °C, the vacuum pump was started, and the drive motor turned on. The rotor was run up to approximate operation speed, 1050 rpm. The events of the next ten minutes can be clearly analyzed in retrospect. However, at the time, there was no obvious reason to suspect an impending bearing problem. The observations of motor drive torque and the absence of any audible bearing noise indicated that the bearings were operating normally. The first few lines of data had been printed out when the rotor abruptly stopped. The total operating time is estimated to be ten minutes.

The RGG was quickly disassembled. It is significant to note that the sensing components had sustained no damage. The damage was limited to bearing No. 1 which had seized. Later, when the pintle and bearing were separated, we observed the type of damage to be almost identical to that sustained in the test rig by bearing No. 2, just four weeks earlier.

4. Cause of Bearing Failure

The evidence as to the cause of the failure of both bearing No. 1 and No. 2 was lack of lubrication. Since no failure occurred at the bearing subcontractor's facility during his bearing test program, we can only assume that the bearing No. 2 failure was due to lack of proper handling by the Hughes personnel. Possibly this could have been avoided by having subcontractor personnel assist in the bearing tests.

Later analysis of the records obtained just before bearing No. 1 failed, clearly indicate that it was operating on a thin film, i. e. , not in its intended thick film hydrodynamic mode of operation. Lubricant was lost during assembly prior to operation, or during operation, or at both times. We can postulate that an air bubble was trapped in the bearing or reservoir. When exposed to the final vacuum, the bubble would have expanded thereby forcing the oil supply out of the bearing and reservoir. We can also postulate that the capillary oil seal on the bearing was not able to adequately support the static pressure head of the lubricant in the vacuum. If true, this would result in a slow loss of lubricant out through the seal to the area of lower pressure.

5. Corrective Action

Corrective action will require an intensive re-examination of the bearing design with regard to the vacuum requirements. The original bearing concept, dimensions, tolerances, materials, and surface coatings are satisfactory. We still have confidence that Shaker Research is the proper subcontractor to assist Hughes in this effort. Corrective action will require both time and engineering effort by Hughes and Shaker. These future tasks will include investigation of the lubrication filling procedures, and review and correction of the design deficiencies.

B. Isoelastic Arm

1. Design and Tests

Static deflection tests were run on a prototype arm plate to check the isoelastic arm design calculations. In these tests, the arm was tested in two different orientations to determine its lateral and longitudinal stiffnesses, k_y and k_x . The arms were supported on a stand and various loads applied; the amount of load was sensed and

controlled by a precision load cell. The arm deflections were monitored along several points on the arm by a sensitive electronic displacement gauge.

The test results showed quite good agreement between our analyses and the experiment. One discrepancy was noted however. The longitudinal deflection of the end of the arm, i.e., the area where the end mass attaches to the arm, see Fig. III-B-1, was found by test to be significant. In our analyses, we had assumed this portion of the arm structure to be rigid. By uncovering this discrepancy, we felt the results justified the relatively minimal effort of performing the static tests. It had a significant effect in influencing the area of the arm which would be trimmed to bring the anisoelastic error to zero.

Originally, we envisioned that area A of Fig. III-B-1 would be trimmed (by reducing the dimension H) to adjust the anisoelasticity. After correcting the structural model equations to account for the end member deflection, it was found that varying H had little effect on the anisoelasticity. It was determined that trimming area B (to reduce dimension G) had a much more significant effect on the anisoelastic coefficient. Hence in planning follow-on efforts, material must be removed to reduce dimension G to achieve the required degree of isoelasticity. Accordingly, the present arm plates have been machined to be initially unbalanced. This was accomplished by increasing the dimension G by 0.125 in. This results in a stiffness ratio, $k_x/k_y = 1.16$, compared with the desired value of 0.945 (0.945 is desired rather than unity to offset the effect of different "moving" mass distributions in the x versus the y direction). This original, intentional stiffness mismatch corresponds to an anisoelastic error coefficient of approximately 15,000 E. U. /g² at the sensor output.

2. Trim Procedure

To trim this initial anisoelastic error coefficient, we have designed a special tool that will be used to remove the material

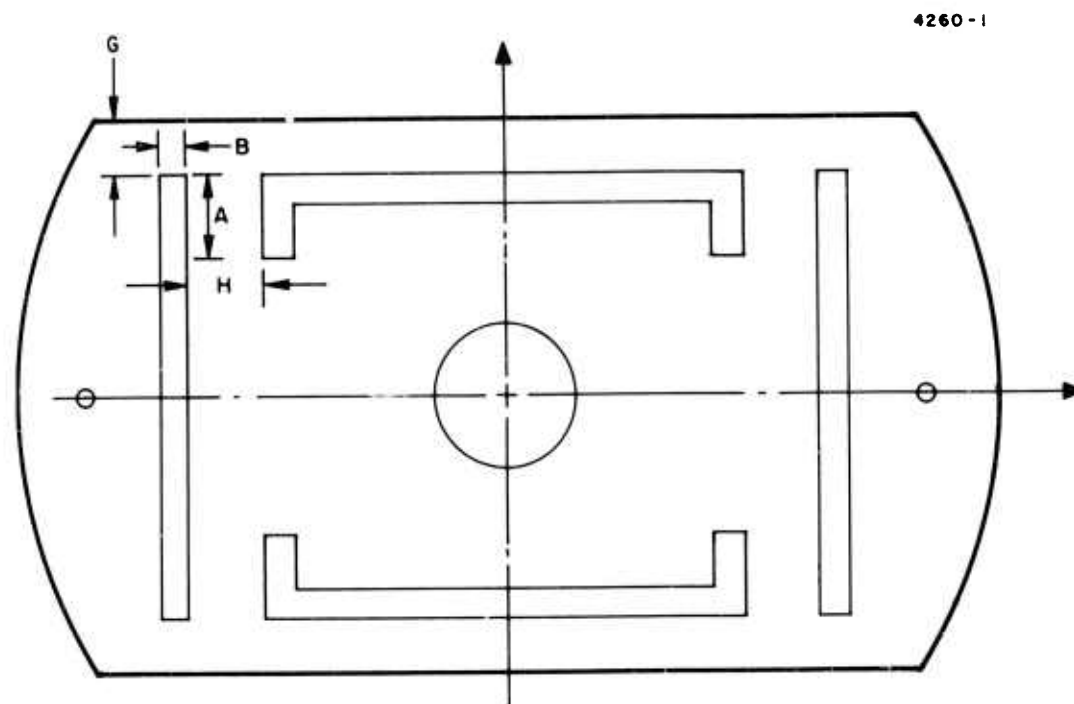


Fig. III-B-1. Arm plate static test specimen.

to reduce dimension G. The tool (see Hughes Drawing No. 740556) is essentially a small single-axis feed milling machine that consists of a rotating tungsten carbide cutter, powered by a miniature gearhead motor, a guide which fits snugly in the cross slot of the arm, and a precision feed mechanism. The feed mechanism utilizes a commercial micrometer movement that drives through a 2:1 lever arm so that 0.001 in feed of the micrometer screw feeds the cutting tool 0.0005 in.

It was necessary to develop such a fixture to be able to attain the precision control on trimming the dimension G. Since there are four arm plates with two slots per plate and two ends per slot, there are 16 possible areas to be trimmed. It is anticipated that the first coarse trimming will be performed on all 16 areas. However, for final trim, possibly only four or eight areas will need to be trimmed.

Anisoelastic trimming on the completed sensor has not yet been attempted. Mass balancing and other adjustments to the sensor must be completed first so that an accurate estimate of the prime anisoelastic coefficient may be obtained. The anisoelastic coefficient of the present hardware may only be trimmed by removing material from the arms. The trimming operation with this first sensor will be a learning process which will require time for the trimming iterations and caution that too much material not be removed. Future trimming operations with subsequent sensors will benefit from this initial learning experience.

C. Pivot Torsion Spring Rate and Q Test

Tests were conducted to measure the Q and the torsional spring rate on a test specimen which simulated one of the sensor torsion bar "pivots." These tests experimentally verified the influence of end effect on the pivot torsional spring rate. The end effect reduced the torsional stiffness by 18.8%.

Q measurements on the test specimen indicated that the Q was 9300, a value larger than expected, especially considering that the test specimen had one bolted joint. These test results are discussed in detail in Appendix B.

The measured influence of end effect was used to modify the design dimensions of the sensor pivot structure.

D. The Q of the RGG

The concept of the Hughes RGG requires a relatively high mechanical Q of the sensor structure. The present RGG design utilizes a one-piece inner rotor construction. That is, the individual arm plates, pivots, central support plate, and the end support bosses are machined from a single piece of aluminum. Since there are no accurate data that allow the Q of a structure to be calculated, a test structure was built. The tests are discussed in Appendix B where it is shown there that the mechanical Q of the sensor would be over 9000.

The Q of the completed sensor is affected by the losses in the piezoelectric transducers and by the load resistor on the transducers. The value of the load resistor is selected to lower the system Q to approximately 300. The Q of the existing RGG has been set to 330. It could have been lowered to 300, but this would have resulted in a relatively severe signal amplitude penalty. Since the exact Q value attained is not at all critical, as long as it is stable, the 330 value was selected as a practical operating point.

E. Piezoelectric Transducers

Six piezoelectric transducers were purchased as specified in the R&D Evaluation Report, dated January 1973. Initial tests on these transducers demonstrated an acceleration sensitivity that was unexpected. The preliminary analysis in that Evaluation Report had not predicted

this sensitivity. A very thorough analysis of the transducer was then initiated. While this analysis was in progress, a new batch of transducers was purchased. These were manufactured to the same specifications as the first batch except that the electrode plating was extended to the full length of the transducer. The full length plating was primarily intended to help overcome a breakage problem with only some consideration that there might be an end effect problem.

The new full-plated transducers reduced the acceleration sensitivity by a factor of about 15. The detailed transducer analysis showed that without full plating, mechanical tolerances of the plating and end effects in the clamping area could be expected to introduce an acceleration sensitivity of approximately the magnitude that had been observed. In addition, the detailed analysis revealed a small inherent acceleration sensitivity term in the transducer output. All of the effects combined in the current transducer results in an acceleration sensitivity of 3 to 4 mV per g. This value is felt to be acceptable in the existing unit and it seems probably that it can be reduced in future designs if this is considered to be required.

F. New Photoelectric Pickoff

Experiments conducted during early 1974 demonstrated that the photoelectric cell, sensor encoder disk and light source designed to control the speed and rotor position of the RGG sensor did not meet the required resolution and stability requirements established in the R&D Design and Evaluation Report, dated January 1973. An instantaneous rotor position error of 2.5×10^{-5} rad (1σ) and an average position error 2.0×10^{-5} rad (1σ) is required by the above referenced report.

The first photoelectric cell, light source (PE/LED) and encoder disk were tested in a servo loop utilizing a hydrostatic air bearing, a drag cup motor, and an inertia load that approximated the final RGG

rotor. It was found that the instantaneous position error was 2 or 3×10^{-4} rad and that the average position error was uncertain by slightly more than 2×10^{-5} rad (1σ). The error in the average was largely due to the uncertainty (jitter) of the instantaneous indicated error. It was determined that the primary cause of the apparent instantaneous position error was due to the PE/LED trigger level uncertainty.

A new PE/LED package and amplifier circuit was designed. The Type TIXL27, P-N Gallium Arsenide Diode Light Source (Texas Instruments) was used for the light source. This light-emitting diode (LED) has a small (0.4 mm x 0.4 mm) square source and delivers a minimum of 7.5 mW into a cone of 135° included angle. A precision condensing lens was used to reduce the image size to approximately 0.1 mm x 0.1 mm at the edge of the slot in the encoder disk. The radiant power passing through the slot in the encoder disk was collected by an integrated photoelectric cell and high transconductance amplifier (Merit, Inc., FDA425).

The output of the PE was amplified by a factor of approximately 30 and delivered to a 10,000 Ω load resistor which served as the input to a comparator stage and simultaneously to a sample and hold stage. The peak PE voltage across this load resistor is about 3 V with a total rise time of approximately 20 μ s. In the region of steepest rise, the voltage has a rate of rise of $1/6$ V/ μ s. By means of two monostable timers, the sample-and-hold circuit is allowed to sample the peak of the PE pulse for 30 μ s. One-half this peak sample voltage is used as the reference for the comparator.

Thus the comparator, which has a 10 mv switching sensitivity, is switched on at the edge of each slot when the PE pulse output is at one-half the peak level of the previous slot. Variations in amplifier gain, LED output, etc. have little effect on the pulse position accuracy as long as they occur at a rate that is slow compared with $1/140$ s.

The circuit diagram for this new design is shown in Hughes Drawing SC No. 72374.

The RGG computer system has the capability of printing the actual counts that occur in all eight consecutive octants of the encoder disk once every 175 revolutions. The printout is the total counts in each octant minus 2^{16} . A sample of such a printout is shown in Fig. III-F-1. Since the individual 10 MHz pulses cannot be divided, and since the interface circuitry prevents any count from being lost, the variation of the last digit is expected to be ± 0.5 . One unit variation in the last digit represents 1.1×10^{-5} rad. Since the printed value represents the instantaneous servo error as well as the PE/LED jitter, it is apparent that on this sampled data basis, the photocell jitter is well within the 2.5×10^{-5} (1σ) rad instantaneous position error. It is completely satisfactory from this point of view. Long term mechanical stability and electrical noise immunity have not yet been proved. This will be further evaluated during the next phase of the RGG development program.

G. Speed Control Servo and Spin Motor Operation

It was shown in Section III-F of this report that the new PE/LED provided encoder disk position information with an uncertainty of less than 2.5×10^{-5} rad (1σ). That section also referenced the RGG system speed control servo requirements of 2.5×10^{-5} rad (1σ) instantaneous position error, and an average position error of not more than 2.0×10^{-5} rad (1σ). The average position error refers to averaging times from days down to 10 s.

The digital computer outputs a digital error signal 140 times per second. This is converted from a digital to an analog error signal which then drives the speed control servo. The digital error signal is composed of the sum of two terms. One of these is a damping term

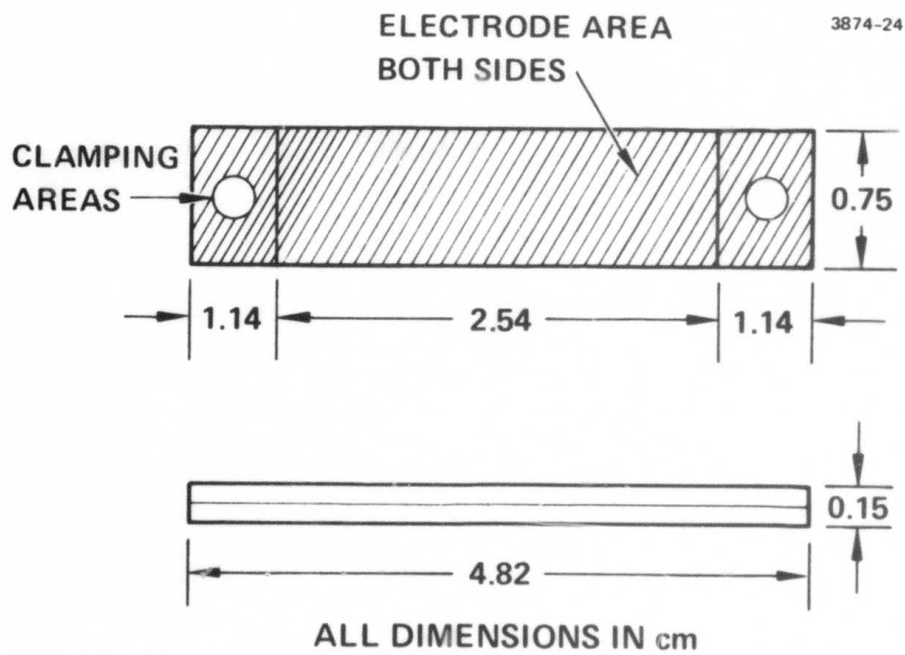
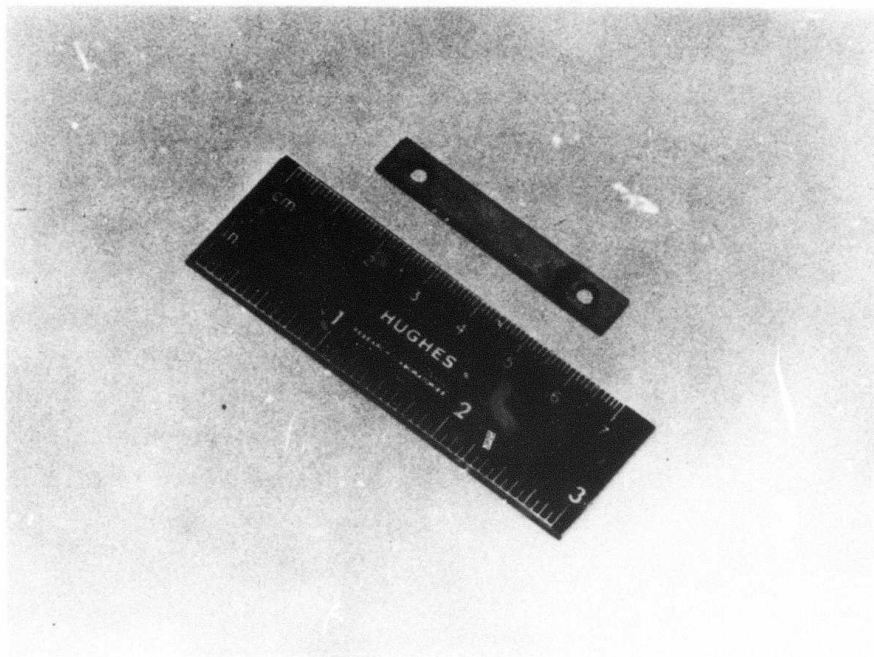


Fig. III-E-1. Piezoelectric bender transducer.

that is proportional to the difference between the desired 10 MHz octant count and the actual octant count. The other term is proportional to the sum of all of the octant count errors since the servo first synchronized. A typical proportionality constant for this output term is 550 analog volts per radian of integrated error. Since the analog output voltage is $1.00 \text{ V} \pm 0.05 \text{ V}$ for days at a time, the long-term average obviously is being met with ease.

An electronic counter is connected so that it can average the number of 10 MHz reference counts during 10, 100, or 1000 revolutions with an error of not more than one count. If the electronic counter is set to average for 100 revolutions, and the sensor speed is 17.5 rps, then the average number of 10 MHz counts per rev should be 571429.00. A variation of one count in the first digit before the decimal represents an average position error of $\pm 1.1 \times 10^{-5}$ rad averaged over a period of 5.7 s. When the servo is operating normally, average count variations occur only in the two digits to the right of the decimal point. Therefore, the average position requirement is easily met.

See Fig. III-G-1 which depicts the spin motor components and the slotted encoder disk.

H. Power Input and Signal Output Transformers

During the initial design of the RGG sensor, it was proposed that air core radio frequency rotary transformers would be used. Their purpose was to couple power into the rotor and couple the signal out. Early tests on a breadboard system showed that rf leakage fields caused excessive induction heating of the sensor.

Ferrite core rotary transformers were designed as shown in Fig. III-H-1. The primary winding of the power input transformer was designed to accommodate a transistor output stage operating from a single +15 V power supply. This concept aids in the implementation

AEA

4. 1.75 10:54 TJJ 1 BIAS 360.0000 0.0 0.0 0.0000
 A1-A3= 143. 121. 133. 73. 156. 170. 220. 163.
 AR1 0.5029 0.7363 AR12 0.5133 0.5050 TU-FAC 14400.
 LAST BAL 3. 6.75 10:23. SPEED 560630.00 0.10 21 = 35.0710
 SERVJ 0.010 1.000 GAIN 11.34617 FAC 0.0937300

COND CJS SIN MAG PHA F1-CAR JCT.PER

JCT CLK 4550 4550 4549 4550 4549 4551 4549 4549

JCT CLK AVE

JCT CLK 4550 4550 4549 4550 4549 4550 4543 4549

JCT CLK 4550 4549 4549 4543 4549 4550 4543 4547

JCT CLK 4550 4550 4549 4549 4549 4550 4543 4549

JCT CLK 4549 4550 4549 4549 4549 4549 4543 4549

JCT CLK 4549 4550 4549 4543 4549 4550 4543 4549

JCT CLK 4550 4550 4549 4543 4549 4549 4549 4543

JCT CLK 4549 4549 4550 4543 4543 4549 4549 4549

JCT CLK 4549 4550 4549 4543 4549 4549 4543 4550

JCT CLK 4549 4549 4549 4543 4549 4549 4543 4549

JCT CLK 4549 4549 4549 4543 4549 4549 4543 4549

JCT CLK 4543 4549 4549 4543 4549 4549 4543 4549

JCT CLK 4550 4549 4549 4549 4549 4550 4549 4550

J.C. ERRS 396=N -0.3 0.1 -0.2 0.9 -0.2 -0.6 0.6 0.1

EA SEP 0.17

A1.....A3 -0. -0. -0. 0. 0. -1. -0. 0.

=

POJ

PLA 4. 1. 75.

PTI 9. 15.

SPEED 560630.0 0.1000

A14 143.00000 121.00000 133.00000 73.00000

A53 156.00000 170.00000 220.00000 163.00000

AR1 0.50293 0.73634

AR2 0.51330 0.50500

LDA 3.00000 6.00000 75.00000

LT1 10.00000 23.00000

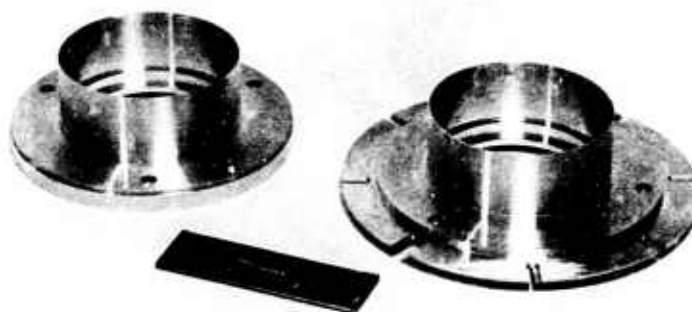
SER 0.01000 1.00000 0.00000

FAC 0.093730

GAI 11.346169

BIA 360.00000 0.00000 0.00000 0.00000

Fig. III-F-1. Computer printout.



**ROTOR DRAG CUPS
(ONE WITH SPEED
CONTROL DISC)**

Fig. III-G-1. Prototype RGG hardware
spin motors.

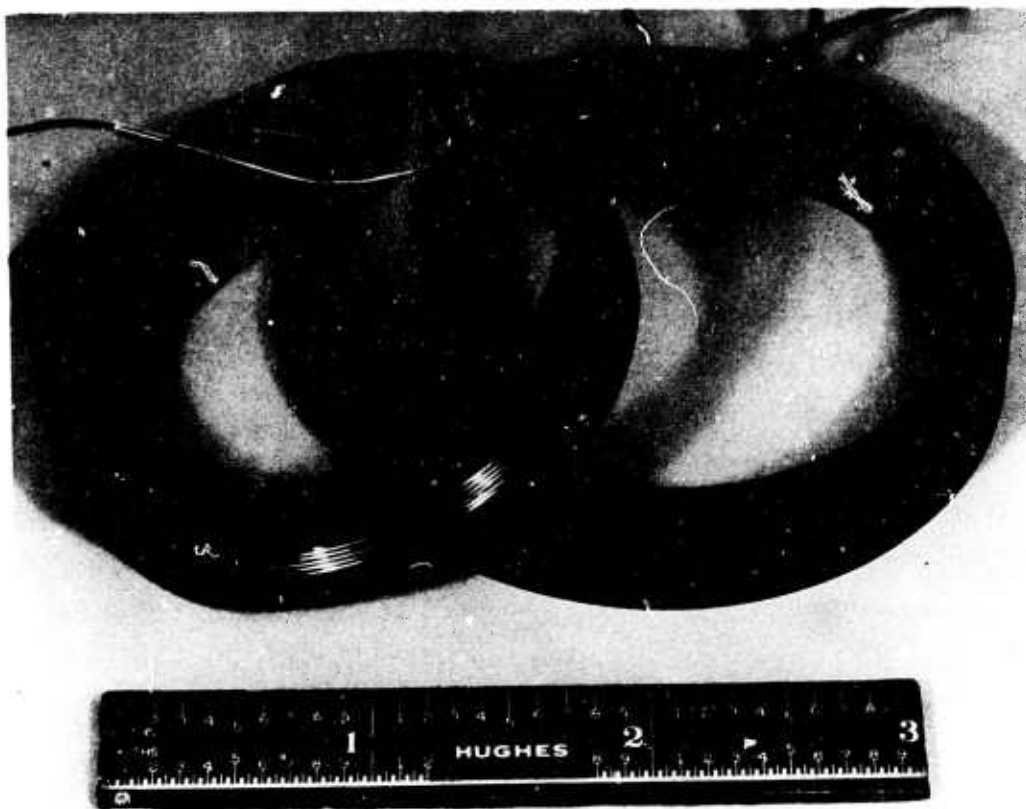


Fig. III-H-1. Rotary transformer.

of the overall electrical system and simplifies the interruption of this source by the Data Injector Logic section. The existing transformers require an input voltage of 6.5 to 7.5 V, peak to peak. At 7.5 V, the line current is 0.95 A peak to peak and the winding current, on the load side of the line and tuning capacitors, is 1.4 A peak to peak.

The FM output transformer is not critical. A few turns were wound on both sides for convenience and tuning purposes. They also serve to put a damping load on the output to eliminate the phase lag of a modulated high Q secondary.

The new ferrite rotary transformers seem to be satisfactory in every way; no changes or modifications are anticipated.

I. The "Cap Driver" System

The R&D Design Evaluation Report, dated January 1973, discussed a proposed method of introducing a known test signal into the RGG sensor. The proposed method consisted of capacitively coupling a test signal to a bistable multivibrator circuit on the RGG rotor. The output of this multivibrator was to be connected to capacitor plates mounted so that the end masses served as one-half of the capacitor. Thus, an external signal driving the internal multivibrator would apply a voltage between fixed capacitor plates and the end masses on the arms. The voltage across this capacitor would apply a differential torque and thus drive the sensor arms. This sensor drive system became known as the "Cap Driver." The actual drive capacitor plates were never installed, but all of the electronics and other necessary components were installed.

Thus, it is possible with the existing RGG to introduce an external signal and, by means of the sensor internal logic, to cause this signal to generate various test functions. We can

- Monitor regulated voltage supply
- Monitor unregulated voltage supply

- Monitor internal temperature
- Introduce a 1 mV electronics test signal.

Monitoring these signals has been helpful during this startup and initial adjustment phase. Unfortunately, the cap driver operation has been relatively erratic. It does not trigger reliably on external input signals and sometimes triggers erratically with no external input. In the future, tests and adjustments will be required to improve the performance of this useful feature. These tests and adjustments would be trivial if they could be performed on an open, nonrotating sensor. In fact, the Cap Driver system was operating perfectly in a bench environment prior to installation in the sensor. The erratic operation is due to the sensor environment of radio frequency fields, spin motor magnetic fields, coupling capacitor spacing, and bearing vibration. To make each adjustment, the sensor must be dismantled to expose the electronics, the adjustment or change made in the electronics, the sensor reassembled and tested. This is not difficult, but it is time consuming.

In the next phase of the RGG development, when new bearings have been installed and the sensor is operating properly, all the features of the original Cap Driver concept should be incorporated so that we can apply a precisely known torque to the sensor arms.

J. RGG Temperature Control

The temperature control system for the RGG is patterned after the systems used with precision gyros and accelerometers. This same concept is generally accepted as having the best absolute accuracy and best repeatability of all temperature control systems in the limited temperature range between 38° and 93° C.

The RGG temperature-sensing elements consist of two thermally sensitive resistance wires formed into a four-leg bridge along with two precision high-stability reference resistors. The temperature-sensitive resistance wire is 70% nickel, 30% iron, called "Balco," and

is made by Wilbur B. Driver Company. Balco has a temperature coefficient of resistance of $+0.0045 \Omega/\Omega/^{\circ}\text{C}$ at 20°C . In addition to this relatively high temperature coefficient, Balco has excellent long term stability and is relatively insensitive to strain. The reference resistors have temperature coefficients of 5 parts per million (ppm) per degree C or less and a resistance stability of 20 ppm per year.

The temperature control bridge is excited by a 10 V, 1000 Hz sine wave. The bridge output signal ($22.5 \text{ mV}/^{\circ}\text{C}$) is amplified by a bandpass amplifier to a level of $5.4 \text{ V}/^{\circ}\text{C}$. The use of the filtered ac carrier avoids errors due to thermal EMF, contact potential and pickup. After ac amplification to high level, the signal is phase sensitive demodulated and a dc heater current is generated. The use of dc for the heater current prevents the output from coupling into the temperature sensing bridge. The "temperature gain" of the system is $5580 \text{ W}/^{\circ}\text{C}$ at the present time; this is to be increased in the future.

Each half of the RGG stator has a four-turn spiral groove with a pitch of four turns per inch. A bifilar heater winding is laid in these grooves and cemented to the stator. An additional groove has been cut in the top of the lands and the temperature sensing resistance wire is cemented into these top grooves. The bridge reference resistors are mounted on the RGG stator so that they too are temperature controlled. The inactive bridge connections are only a few inches in length and are temperature controlled.

The temperature control system has been tested and found to be satisfactory. The heater power required to maintain the sensor at 43°C in a 23°C ($\Delta^{\circ}\text{C} = 20$) room ambient with no thermal blanket, is 64 W. The watts per $^{\circ}\text{C}$ ambient are 3.2. With a temperature gain of $5580 \text{ W}/^{\circ}\text{C}$, the temperature hangoff is 0.036°C and the variation with ambient is $6 \times 10^{-4}^{\circ}\text{C}/^{\circ}\text{C}$. The complete sensor has been tested and the resonant frequency has been found to shift $383 \text{ ppm}/^{\circ}\text{C}$. With a sensor mechanical Q of 330, the phase of the output will shift

$$\Delta\psi = -2Q \frac{\Delta\omega}{\omega_n} \text{ rad.}$$

The RGG error budget has assumed $\Delta\psi = 1.2 \times 10^{-4}$ (1 σ) due to the temperature control. Thus the allowed $\Delta\omega$ is

$$\Delta\omega = \frac{\Delta\psi \omega_n}{2Q} = 4 \times 10^{-5} \text{ rad/s}$$

or, as a ratio

$$\frac{\Delta\omega}{\omega_n} = 1.8 \times 10^{-7}.$$

Thus the standard derivation of temperature variation that can be allowed is

$$\begin{aligned} \Delta T &= \frac{\frac{\Delta\omega}{\omega_n} \text{ allowed in error budget}}{\frac{\Delta\omega}{\omega_n} \text{ measured temperature sensitivity}} \\ &= 4.7 \times 10^{-4} \text{ }^\circ\text{C.} \end{aligned}$$

This temperature control requirement is essentially the same as the original 1.0×10^{-3} $^\circ\text{C}$ estimate when the original is corrected for the difference between the shear modulus temperature sensitivity of beryllium copper (-350 ppm/ $^\circ\text{C}$, original pivot material) and aluminum (-580 ppm/ $^\circ\text{C}$, present pivot material).

As shown in the previous paragraphs, we can overcome the effects of ambient temperature variations at the present time and even this can easily be improved. The principal temperature control problem lies in the variable power input to the spin motor drag cups, the

rf power variation and the variable power dissipation in the internal sensor electronics. The thermal resistance between any of these sources and the external heat sink is believed to be such that a fraction of a watt change in any of them will cause the average pivot temperature to exceed the allowable limit.

Since these thermal resistances are not accurately known, a detailed thermal analysis, and development of new methods of regulating the sensor rotor power input will be required. This task had been fully anticipated and the need documented in May 1974.

K. RGG Sensor Electronics

Only minor changes have been made in the sensor (internal) electronics since the last report period. For example, the thermistor internal temperature sensing circuit was modified slightly to improve the temperature resolution. A single transistor, a zener diode, and three resistors were added to allow the internal regulated and unregulated voltage to be monitored. Also, a 1 mV, 2 ω electronics test signal was added. The power regulator, internal logic decoding balance tube logic, frequency modulation circuit, preamplifier, and filters are unchanged.

These electronics packages have performed according to specification in every respect. Based on our operating experience of the RGG sensor as a complete unit, we would expect to add some additional logic to any new RGG design. This would allow additional internal monitoring and filter modification. Such additions and changes would be simple and straightforward.

L. External RGG Electronics

Only one significant change has been made in the external RGG electronics since the last report period. A Signal Conditioner Panel has been added. This panel accepts the output of the sensor photocell-encoder disk position and the slot corrections from the computer.

Phase locked, voltage regulated 1ω and 2ω square and sine waves at 1 volt and 10 mV are then generated. These reference and test signals have been found to be very useful during all phases of electronics and RGG sensor test and adjustment. In fact, these signals have been found so useful that the panel will be redesigned in the next phase of this program to provide 3ω and 4ω signals. In addition, the panel will be split up so that the outputs are more accessible.

The external rf power supply for the RGG sensor is relatively inconvenient to use in its present configuration. The output voltage level is not sufficiently stable and must be monitored at frequent intervals. This power supply must be redesigned and repackaged. This will be a straightforward design and test effort.

The computer I/O and servo electronics have met all performance requirements and have not been modified or changed since the last reporting period.

M. Balance Tubes

The RGG sensor balance tubes have been installed on the sensor and are generally satisfactory. However, some specific problems exist that must be explored in depth, both experimentally and theoretically, before the balance tubes can be considered fully satisfactory. The problems are believed to be due almost entirely to the limited production of this batch.

First, it was found that the present tubes are too fragile. The walls of the tubes are too thin. Correction of this problem requires that thicker wall tubes must be specified and used. The epoxy end seals on several tubes pulled off during normal handling. A quality control batch was given a "lead pull" test and passed, but somewhere in the production process, control was lost. New tubes will be individually tested. Also it is believed that the ends of the tubes should be etched to give the epoxy a better grip.

Electrical continuity within several tubes was lost after they were installed. Several more were lost when the tubes were

electrically exercised (by moving the gap back and forth along the length of the tube). The failure is believed to be due to contamination within the tube. It is known that the manufacturer did have difficulty cleaning the 0.030 mm diameter internal bore; the probability is high that some were not perfectly clean. The quality control solution to this problem by the vendor should consist of better cleaning of the tubes and an end-to-end exercise (10 to 20 round trips) of the gap before shipment.

The solutions to the foregoing problems have not yet been fully investigated; therefore, it is premature to comment on the level of remaining effort. Early attention to this matter will be given in the next program phase.

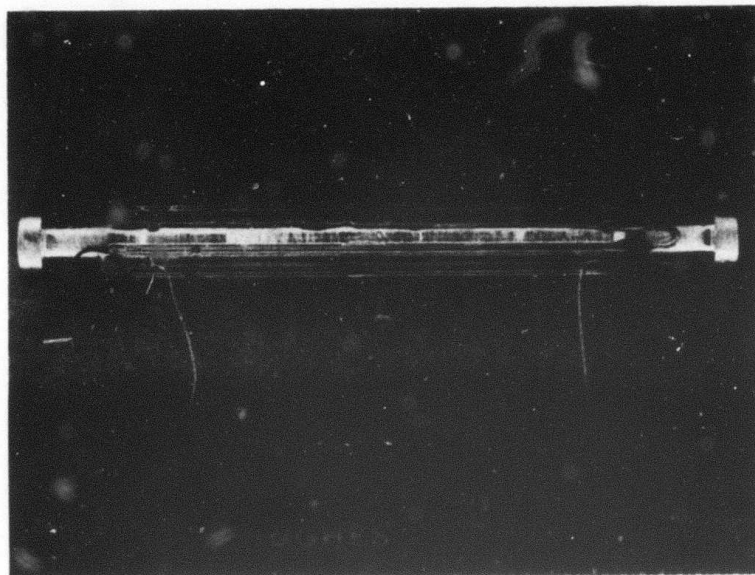
See Fig. III-M-1 which depicts the balance tube details and mounting provision whereby four tubes are attached to aluminum posts.

N. Computer

The concept of using a digital minicomputer to provide the functions of speed control, data reduction, and filtering has proved to be rewarding. This subsystem operates exactly as originally visualized and has been highly reliable. The present computer programs are essentially the same as those published in the November 1973 Semiannual Technical Report and no major changes are anticipated.

O. Vacuum

A vacuum is needed inside the sensor stator to prevent windage noise and external acoustic noise from exciting the sensor arms and to improve the sensor thermal and rotational speed characteristics. The vacuum level needed is not high, (1 to 500 mTorr(μ m. Mg)) and can easily be attained with a mechanical vacuum pump. There was some initial concern that the many components inside the stator would produce real and virtual leaks and outgassing that would require constant pumping. Specific items of concern were the 12 ports and feed-throughs, the porous ferrite transformer cores, the epoxy-fiberglass



Four tubes mounted on post

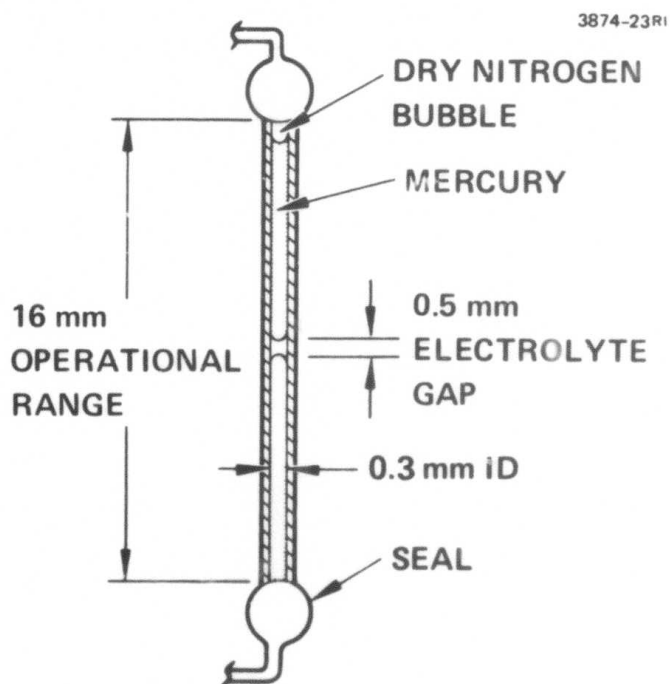


Fig. III-M-1. Mass balance device.

substrates for the electronics and capacitive driver subsystems, the laminated motor cores and windings, and the epoxy bonds.

Fortunately, these were not a problem. After initial assembly, the sensor was easily evacuated to 1 mTorr. After a week, the outgassing was reduced to the point where less than 1 mTorr was reached during pumping, and after the pump was disconnected, the vacuum level would stay below 100 mTorr for more than 24 hours. The noise level due to this pressure was not noticeable at the 100 E.U. level. At 500 to 1000 mTorr it did become noticeable. From previous experience with similar systems the prototype sensor should be capable of sealed-off operation for weeks at a time if it has been subjected to an initial pumpdown period of 3 to 5 days at operating temperature. The addition of "getters" or a small "Vac-Ion" pump would extend this period manyfold.

In summary, the vacuum requirement will not present problems in laboratory testing, field tests, or actual operation.

IV. RGG NOISE PERFORMANCE STATUS

A. Introduction

A significant portion of the effort on the Prototype Moving Base Rotating Gravity Gradiometer was devoted toward

- Development of an error sensitivity model for the RGG
- Development of noise specifications for ultimate operation of an RGG system in a moving vehicle
- Development of laboratory test facilities and test procedures to verify the error model and determine the actual sensor error sensitivities
- Development of sensor balancing and adjustment techniques needed to reduce the error sensitivities to acceptable levels
- Operating, evaluating, and adjusting the RGG to attain the desired sensitivity levels.

Initially, we developed an RGG error model and postulated a moving base environment noise specification. Later, we developed the necessary laboratory test procedures and sensor adjustments. By 1975, we verified the validity of the error model by using the model and the adjustment techniques in laboratory tests where the nonrotating error sensitivities of the RGG were reduced to levels suitable for a first demonstration of the sensor in a rotational mode, oriented both horizontally and vertically. Continued application of the error model and the adjustment techniques can now be used to drive the rotating RGG error sensitivities to the desired levels to achieve the 1 E.U. at 10 s performance goal stipulated for a typical moving base environment.

B. RGG Operation and Signal Processing Model

1. Brief Description of RGG Operation

The Hughes Rotating Gravity Gradiometer consists of two orthogonal mass quadrupoles (arms) which are torsionally coupled

to each other and to a common supporting structure (the rotor case). This structure has two fundamental torsionally resonant frequencies, the "sum mode" which is related to the common movement of the arms and the "difference mode" which is related to their differential motion. The spin speed is selected to be equal to one half the differential mode resonant frequency in order to provide resonant amplification of the gravity gradient signal.

When the mass quadrupoles are rotated at constant angular velocity about the torsional axis in a nonuniform gravity field, the second order gradients of the field create periodic differential moments on the arms at twice the spin frequency. The differential mode motion is sensed by piezoelectric transducers, and the resultant signal is amplified, filtered, and frequency modulated within the rotor for transmission to the stator. The FM signal is synchronously demodulated digitally into two quadrature channels using rotor position information. The process is functionally analogous to phase detection of the original analog signal into two channels using the sine and cosine of twice the relative rotor angle. The digitized signals are then filtered (time averaged) to provide the RGG output signals in digital form.

2. Brief Description of RGG Signal Processing

The signal process model consists of the signal sensing and transducing functions, the preamplification and frequency modulation functions, and the detection and signal averaging functions. The signal sensing and transducing functions represent the response of the RGG differential mode to the input mechanical moments and the conversion of the mechanical strains by the piezoelectric transducers into an ac voltage for input to the preamplifier. The differential mode mechanical response of the sensor is characterized by a sharply-tuned transfer function ($Q \cong 330$) at a resonant frequency equal to twice the spin frequency. This response provides a large attenuation of all input mechanical moments except those in a narrow band centered at twice the spin frequency.

The transduced signal voltage is then amplified by a low noise preamplifier with a tuned response ($Q \approx 30$) at the resonant frequency

to provide additional attenuation of the "off-resonance" input moments. The resultant ac signal is frequency modulated using a carrier frequency of approximately 250 kHz and the FM signal is transmitted into the non-rotating detection circuitry.

Signal detection is accomplished coherently and digitally by using eight synchronous rotor position pulses (per revolution) to gate the counts of the FM zero crossings. The gated counts, when properly combined, provide two time varying digital numbers which represent the quadrature components of the original analog signal. These digitally represented quadrature components are time averaged to form the output signals of the RGG signal process model.

A functionally equivalent model of the signal process is shown in Fig. IV-B-2-1. The input to the process is the normalized differential moment which is filtered by an equivalent narrowband filter centered at twice the spin frequency. This equivalent filter, $H_{EQ}(S)$, ideally has unit gain and zero phase shift at twice the spin frequency. Gain and phase uncertainties of the signal process can be modeled as error properties of this equivalent filter.

The synchronous phase detection function is modeled by the sine and cosine multiplications which operate on the filtered input moment in Fig. IV-B-2-1. The averaging functions are represented by the low-pass filters. $H_O(S)$.

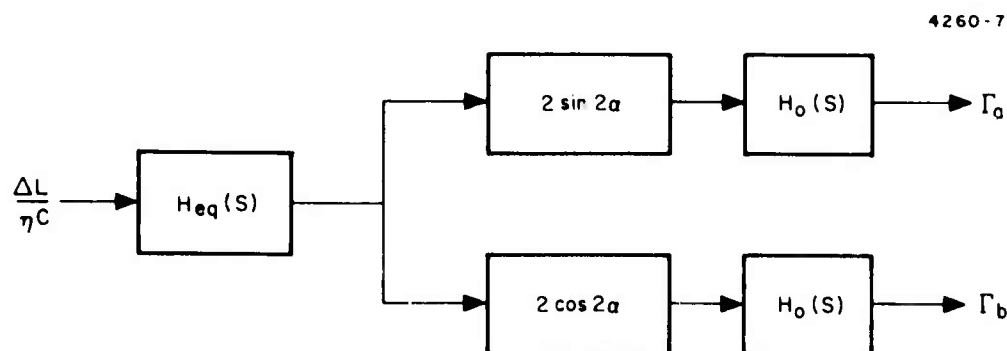


Fig. IV-B-2-1. Equivalent model of signal process.

C. Error Sensitivity Models

Errors can be introduced into the sensor output by various noise sources operating through various error sensitivities at various points in the signal processing chain.

1. Motion Sensitivity Error Model

The most significant sources of error are the error sensitivities of the sensor mechanical structure that convert environmental vibrations and rates into differential torque of the sensor arms at the sensor resonant frequency.

The equation for the known sources of normalized differential moments in the sensor is given by the equation (Fig. IV-C-1-1) where the sensor constants are:

C	- arm inertia	ω_s	- sensor spin frequency
η	- inertia efficiency (0.88)	α	- nominally $\omega_s t$

and the excitation sources applied to the sensor are:

$\Gamma_{jj}-\Gamma_{ii}, 2\Gamma_{ij}$	- gravity gradient signals
ω_i	- angular rates
$\dot{\omega}_i$	- angular accelerations
A_i	- linear accelerations
ΔL_T	- thermal noise

and the error sensitivities are:

K_1, K_2	– differential arm mass unbalance
K_3	– axial vibrational torsional sensitivity
K_4, K_5	– dynamic arm mass unbalance
K_6	– sum mode mismatch
K_7, K_8	– prime anisoelasticity
K_9, K_{10}	– cross anisoelasticity
K_{11}, K_{12}	– spin/torsion axes skew misalignment
$\Delta\Phi_{ij}$	– differential product of inertia

$$\begin{aligned}
\frac{\Delta L}{\eta C} = & \left[2\Gamma_{xy} - 2\omega_x\omega_y \right] \cos 2\alpha + \left[\Gamma_{yy} - \Gamma_{xx} + \omega_x^2 - \omega_y^2 \right] \sin 2\alpha - \left[\frac{\Delta\Phi_{ij}}{\eta C} \right] \left[(\Gamma_{yy} - \Gamma_{xx} + \omega_x^2 - \omega_y^2) \cos 2\alpha \right. \\
& - (2\Gamma_{xy} - 2\omega_x\omega_y) \sin 2\alpha \left. \right] + K_1 \left[\frac{A_x}{g} \cos \alpha + \frac{A_y}{g} \sin \alpha \right] + K_2 \left[\frac{A_y}{g} \cos \alpha - \frac{A_x}{g} \sin \alpha \right] + K_3 \left(\frac{A_z}{g} \right) \\
& + K_4 \left[(\dot{\omega}_x - \omega_y\omega_z + \Gamma_{yz}) \cos \alpha + (\dot{\omega}_y + \omega_x\omega_z - \Gamma_{xz}) \sin \alpha \right] \\
& + K_5 \left[(\dot{\omega}_y + \omega_x\omega_z - \Gamma_{xz}) \cos \alpha - (\dot{\omega}_x - \omega_y\omega_z + \Gamma_{yz}) \sin \alpha \right] + K_6 \dot{\omega}_k \\
& + K_7 \left[\left(\frac{2A_x A_y}{g^2} \right) \cos 2\alpha + \left(\frac{A_y^2 - A_x^2}{g^2} \right) \sin 2\alpha \right] + K_8 \left[\left(\frac{A_y^2 - A_x^2}{g^2} \right) \cos 2\alpha - \left(\frac{2A_x A_y}{g^2} \right) \sin 2\alpha \right] \\
& + K_9 \left(\frac{A_z}{g} \right) \left[\frac{A_y}{g} \cos \alpha - \frac{A_x}{g} \sin \alpha \right] - K_{10} \left(\frac{A_z}{g} \right) \left[\frac{A_x}{g} \cos \alpha + \frac{A_y}{g} \sin \alpha \right] \\
& + K_{11} \dot{\omega}_3 \left[\omega_y \cos \alpha - \omega_x \sin \alpha \right] - K_{12} \dot{\omega}_3 \left[\omega_x \cos \alpha + \omega_y \sin \alpha \right] + \Delta L_T / \eta C
\end{aligned}$$

Fig. IV-C-1-1. RGG Differential moment equation.

The normalized differential product of inertia error $\Delta\Phi_{ij}/C$ is produced by a difference in orientation of the coordinate reference frame used to calculate the inertia (usually oriented to the physical surfaces of the sensor structure) and the coordinate system defined by the principal axes of inertia. This error is analogous to a phase error and is lumped together with all of the other phase errors in the signal processing error model.

Each of the modeled RGG motion sensitivities will respond to selected phase-coherent, spin-harmonic excitations. The excitation functions are either translational accelerations or angular accelerations applied either radially or axially relative to the RGG spin axis. The motion sensitivities and their corresponding excitation functions are shown in Table IV-C-1-1.

TABLE IV-C-1-1
Motion Sensitivity Excitations

Motion-Sensitivity Type	Excitation Function	
	Form	Frequency
Differential Arm Mass Unbalance (K_1, K_2)	Radial Acceleration	$1\omega_s$ & $3\omega_s$
Axial Vibration Sensitivity (K_3)	Axial Acceleration	$2\omega_s$
Dynamic Arm Mass Unbalance (K_4, K_5)	Radial Angular Acceleration	$1\omega_s$ & $3\omega_s$
Sum Mode Mismatch (K_6)	Axial Angular Acceleration	$2\omega_s$
Prime Anisoelectricity (K_7, K_8)	Radial Acceleration	$0.4\omega_s$
Cross Anisoelectricity (K_9, K_{10})	Radial Acceleration	$1\omega_s$ & $3\omega_s$
Skew Misalignment (K_{11}, K_{12})	Radial Angular Velocity	$1\omega_s$ & $3\omega_s$

2. Signal Processing Error Model

In addition to the errors introduced as mechanical moments into the sensing structure, there could be errors produced by:

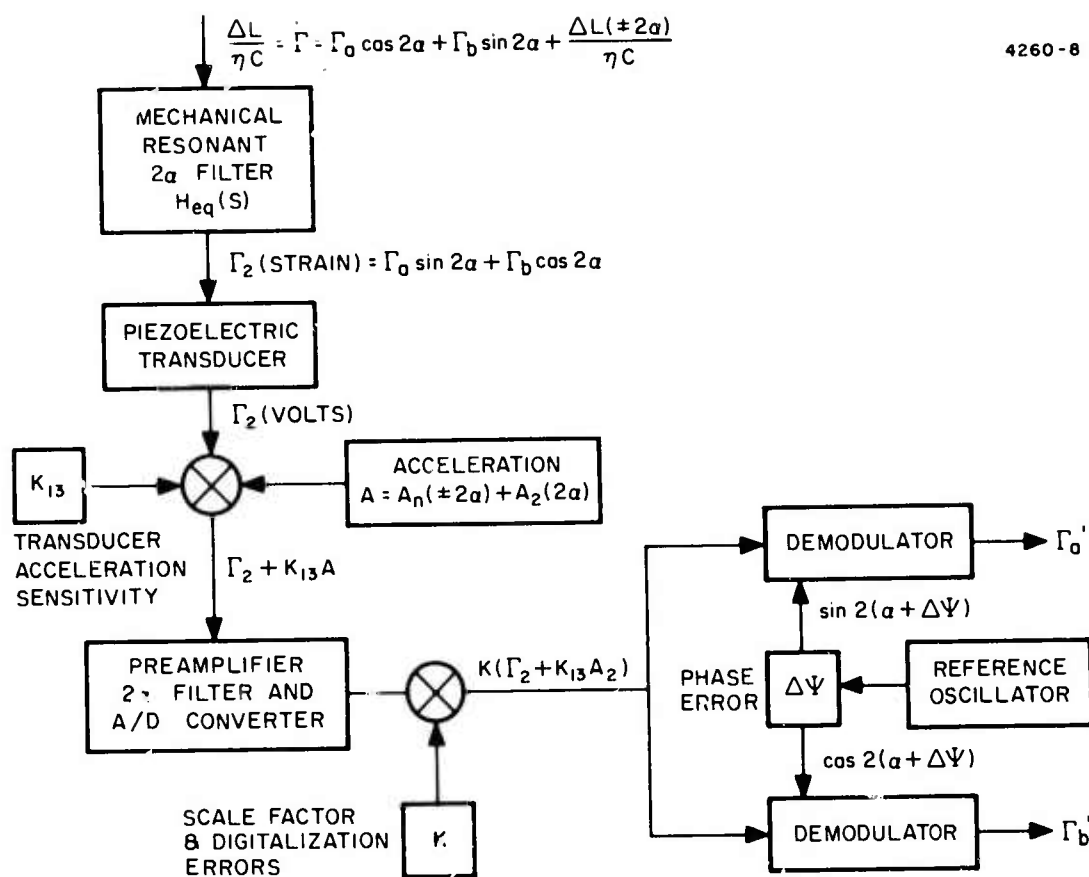
Electromagnetic fields, temperature, or accelerations acting on the transducer or internal and external electronic circuitry to produce stray voltages or phase and gain shifts in the signal channel.

Digitalization errors or other errors in processing, filtering, and presentation of the signal information.

There are three significant error sources that are incorporated into the signal processing error model (see Fig. IV-C-2-1). First is the direct sensitivity of the piezoelectric transducer to acceleration. The transducer is a bender bimorph that is closely matched to give minimum response to acceleration. The residual acceleration sensitivity (K_{13}) produces a twice revolution voltage output when the vibration frequencies in the sensor reference frame is at twice spin speed. This error enters directly at the transducer and thus does not have the high Q (≈ 330) behavior of the vibration sensitivities in the mechanical portion of the sensor, but instead has a much faster decay time associated with the preamplifier filter. ($Q = 30$).

The second significant error source is scale factor error. This includes initial calibration error, variations in the scale factor due to temperature and aging effects, and short term variations due primarily to digitalization errors. These scale factor errors can be produced at many points in the signal processing chain. For the signal processing error model they are assumed to occur at the output of the analog to digital conversion process.

The third significant error source is phase error produced by propagation of the signal (driven at twice spin speed) through the mechanical resonance filter and pre-amplifier filter (peaked near twice spin speed), and by differences in the coordinate reference systems of the sensor inertia tensor, the speed control servo, case alignment, platform alignment, and the demodulator reference



$$\Gamma'_0 = K(\Gamma_0 \cos 2\Delta\Psi - \Gamma_b \sin 2\Delta\Psi + K_{13}A_{2s}) \approx K(\Gamma_0 - 2\Delta\Psi\Gamma_b + K_{13}A_{2s})$$

$$\Gamma'_b = K(\Gamma_b \cos 2\Delta\Psi + \Gamma_0 \sin 2\Delta\Psi + K_{13}A_{2c}) \approx K(\Gamma_b + 2\Delta\Psi\Gamma_0 + K_{13}A_{2s})$$

Fig. IV-C-2-1. Signal processing error model.

oscillator. For the signal processing error model, all of these phase errors including the differential product of inertia error are assumed to occur in the reference oscillator.

There are other potential error sources, especially the magnetic field response, that are not included in this model. They will be incorporated in the future if laboratory tests show them to be significant.

D. Error Sensitivity Adjustments

Adjustments have been provided in the sensor design to allow most of the error sensitivities to be minimized. The nature of the error sensitivity and the adjustment provided are described below.

1. Differential Arm Mass Unbalance (K_1 , K_2)

If the center of mass of a sensor arm is not at the center of support, then an acceleration will introduce an error torque. Large and small radial and torsional mass balance screws are used for rough balancing of each arm. Electrolytic mass balance tubes are provided for final balancing without requiring disassembly of the sensor. The objective is to have the center of mass of both arms lie along a line parallel with the pivot axis. The center of mass of each arm can be off the pivot axis provided both arms are off the same amount.

2. Axial Vibration Sensitivity (K_3)

If the pivot structure holding the sensor arms has a built-in twist, then a vibration excitation along the pivot axis at twice spin speed will produce a differential torque. In the initial design, the sensor did not have provision for adjusting K_3 . During laboratory testing it was found that K_3 could be adjusted by inducing a fixed torsion in the pivot to compensate for the built-in twist. In the laboratory, the torsion was induced by loosening the screws holding one end of the pivot to the top of one of the inner rotors, applying a torque to the pivot, and fastening the screws down to maintain the torque on the pivot. An alternate technique would be to loosen the fit of the inner rotor halves to the center plate, allowing them to be adjusted in angle.

3. Dynamic Arm Mass Unbalance (K_4, K_5)

The arms may have excellent static balance, in that their center of mass coincides with its center of support and the arms therefore, are insensitive to linear acceleration. If, however, the inertia axis is not perpendicular to the pivot axis, (Fig. IV-D-3-1), then the sensor will respond to angular accelerations at right angles to the pivot axis. The adjustment to bring the centers of mass to the pivot axes use the same balance screws as are used for differential mass unbalance, but in different combinations.

4. Sum Mode Mismatch (K_6)

If the inertias of the two arms (I) or the springs (k) of the two arms are different, then the response of the arm to an angular acceleration about the spin axis will be different for the two arms, resulting in a differential torque. We adjust the ratio for the two arms by adjusting the balance screws used for differential and dynamic mass balance. The radial screws are moved out to increase the arm inertia or in to decrease arm inertia. There is a slight second order effect on mass unbalance when adjustment is made for arm inertia so some iteration is necessary. As a practical matter, the best practice is to lower the sum mode mismatch as far as possible first, then adjust for the mass unbalances.

5. Prime Anisoelasticity (K_7, K_8)

The anisoelastic sensitivity effects occur because acceleration of the arms will cause distortions of the arm structure resulting in a shift of the center of mass (see Fig. IV-D-5-1). If the arm is equally elastic in all directions, then the shift of the center of mass is along the acceleration and no torque is generated. The major anisoelastic coefficient in the error model is K_7 . The other coefficient, K_8 , is K_7 rotated by a small angle proportional to the error in orientation of the measurement coordinate axes with respect to the sensor structure coordinate axis. Most mass quadruple structures are

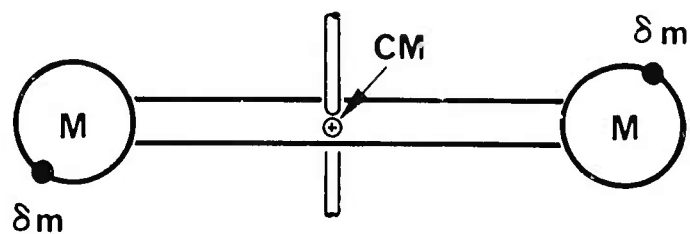
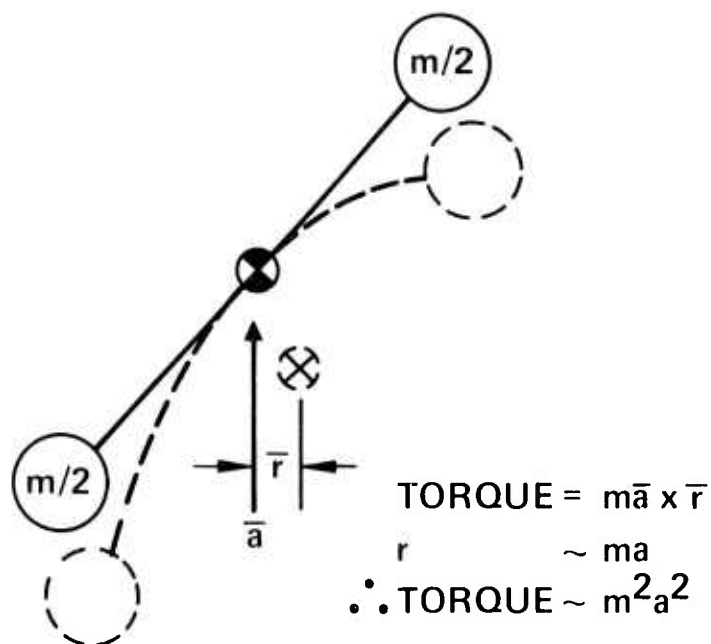


Fig. IV-D-5-1. Dynamic mass unbalance



ACCELERATIONS CAUSE DISTORTIONS OF
 SENSOR ARMS, CAUSING COUPLING OF
 ACCELERATION INTO GRAVITY GRADIENT
 SENSING MODE

Fig. IV-D-5-1. Prime anisoelasticity.

inherently anisoelastic and cutouts in the arms are required to make the spring constant in tension and compression along the arms the same as the bending spring constant. The sensor was designed with these slots (see Fig. IV-D-5-2) and the slot length will be adjusted with a special milling fixture to achieve isoelasticity. The arm slots were deliberately left short during fabrication and we expect to have a value of about $15,000 \text{ EU/g}^2$ in the "as fabricated" condition.

6. Cross Anisoelasticity (K_9, K_{10})

The cross anisoelastic terms are more complex versions of the prime anisoelastic terms that arise because the center of mass of the two arms in the present design are not at the same point, but are displaced along the spin axis. This produces an anisoelastic response to products involving accelerations along the spin axis. These effects should be negligible in this design. So far, our laboratory tests verify this to be so. We do not have a means for adjusting these terms.

7. Skew Misalignment (K_{11}, K_{12})

If the effective elastic axis of the sensor structure is not aligned with the spin axis defined by the bearings, then angular rates at right angles to the spin axis at one and three times the spin frequency can produce torques at $2\omega_s$. (See Fig. IV-D-7-1.) The bearing itself can be a significant source of angular rates at $3\omega_s$ (the $1\omega_s$ component results in a pure coning motion which does not produce error torques). To adjust this error sensitivity, there are two rotor structures. The inner rotor holds the pivot structure and defines the pivot or elastic axis. The outer rotor holds the spin bearings and defines the spin axis. The two are coupled at their center line. The inner rotor can be aligned with respect to the outer rotor by differential screws that compress struts in the outer rotor. (See Fig. IV-D-7-2.)

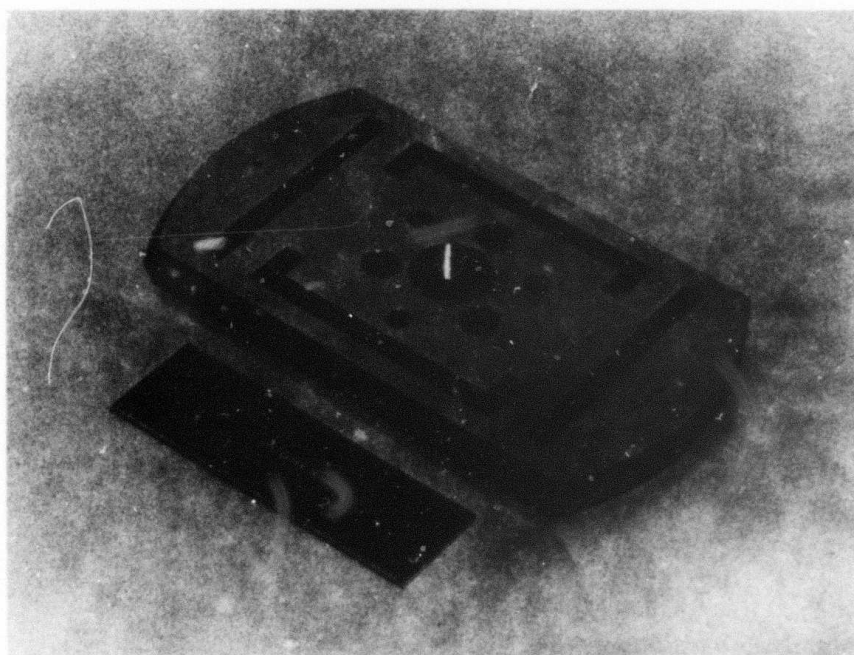
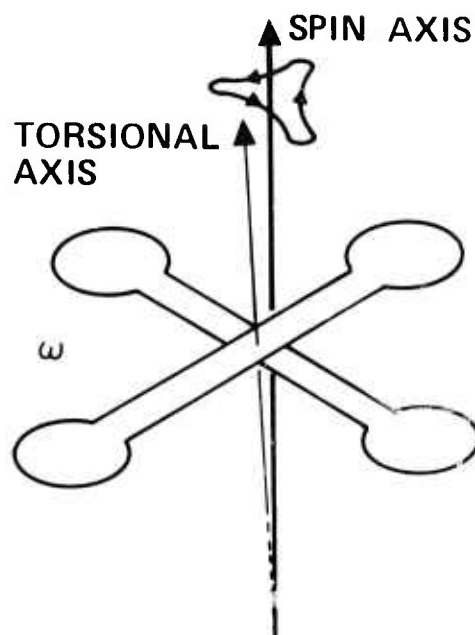


Fig. IV-D-5-2. Isoelectric arm design.



TORSION AXIS OF SENSOR
MAY BE SKEWED WITH
RESPECT TO AVERAGE SPIN
AXIS WHICH COUPLES INTO
 3ω VIBRATIONS OF
SPIN BEARING

Fig. IV-D-7-1. Skew misalignment
sensitivity.

M10774

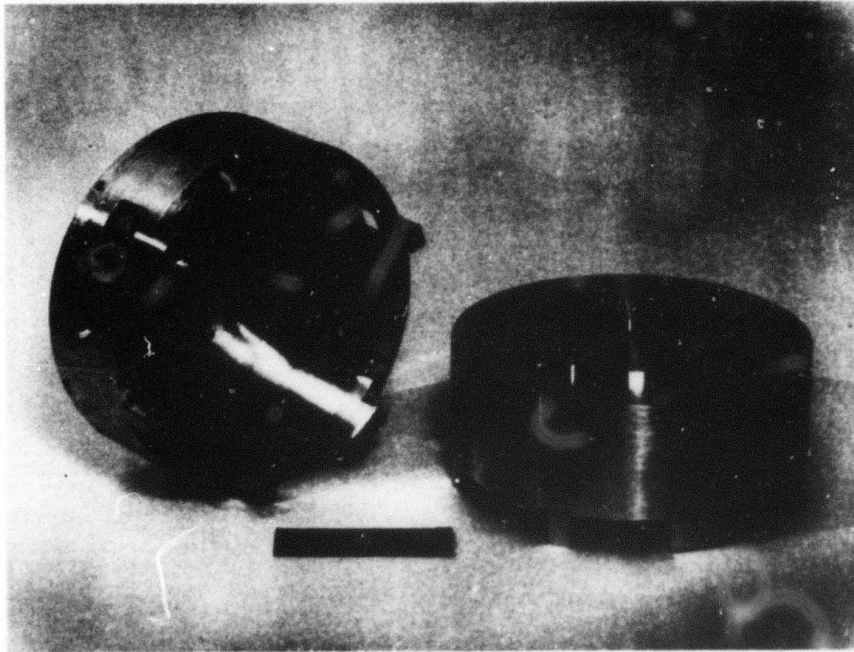


Fig. IV-D-7-2. Skew misalignment adjustment.

Legs of outer rotor are compressed by tightening screws to align torsional axis with spin axis

8. Transducer Mismatch (K_{13})

If the two halves of the bimorph bender piezoelectric transducer are not matched, then there will be a residual sensitivity of the transducer to linear transverse acceleration. This sensitivity can be reduced either by scraping off small portions of the plating on opposite sides of the transducer to balance the transducer output, or the transducer mismatch response can be canceled by an equal and opposite dynamic mass balance mismatch (which is also directly proportional to linear transverse acceleration). Since the time response of the two effects are significantly different, (One occurs in the mechanical portion of the sensor and has a Q of 330 and the transducer mismatch occurs after the mechanical filter and has a Q of 50) this may not be a suitable technique if the acceleration levels are high and variable.

9. Thermal Noise

One of the largest (and fortunately the most predictable) noise source is the thermal energy in the sensor resonant mode producing random mechanical torques through Brownian motion. Because the sensor mode is in thermal equilibrium with the other sensor modes and the rest of the environment, thermal energy is randomly flowing in and out of the sensing mode. The average energy in the mode is given by the Equipartition Theorem of Statistical Thermodynamics as $kT = 4.7 \times 10^{-21}$ J where Boltzmann's constant $k = 1.38 \times 10^{-23}$ J/K, and the sensor temperature is 320 K. The equivalent gravity gradient of the thermal noise is approximately

$$\Gamma_{eq} \approx \sqrt{\frac{2kT}{\eta^2 C \tau_1 \tau_2}} \approx 0.3 \text{ EU}$$

where

Arm Inertia $\eta^2 C$ is 36,200 gm-cm²

Inertial Efficiency η is 0.88

Sensor Time Constant $\tau_1 = 2.7 \text{ sec}$

System Time Constant $\tau_2 = 10 \text{ sec}$

The sensor design provided for large inertia, inertia efficiency and long time constant to achieve this level of noise.

Increasing inertia or time constants or decreasing the effective temperature are possible methods for reducing this noise source, but are not practical or necessary for the purposes of this development effort.

10. Phase Shifts ($\Delta\psi$)

The major source of phase shifts in the RGG system is the shift of the sensor resonant frequency with temperature. The sensor speed is controlled by the computer to be at a value calculated to be exactly one half of the sensor resonant frequency. The torques induced in the sensor arms by the gravity gradient occur at this twice spin speed frequency. If the rotation frequency is equal to the resonant frequency of the sensor, then the phase shift through the resonance is nominally 90° . However, this phase shift is very sensitive to the frequency difference and if the spin speed or the sensor resonant frequency shift, there will be a large change in phase shift (see Fig. IV-D-10-1). In our system, the spin speed is accurately controlled by the computer to parts in 10^{-7} . The sensor resonant frequency is controlled by thermal design and thermal controls so that the temperature sensitive component (the spring constant of the pivots) are maintained at a constant temperature ($0.56 \times 10^{-3}^\circ\text{C}$). As is shown by Section III-J, this level of temperature control will provide the frequency stability needed to reduce the phase errors to an acceptable level.

E. Nonspinning RGG Error Coefficient Correction Method

To reduce the test and adjustment time required to measure and compensate the error coefficients in the completed operating RGG

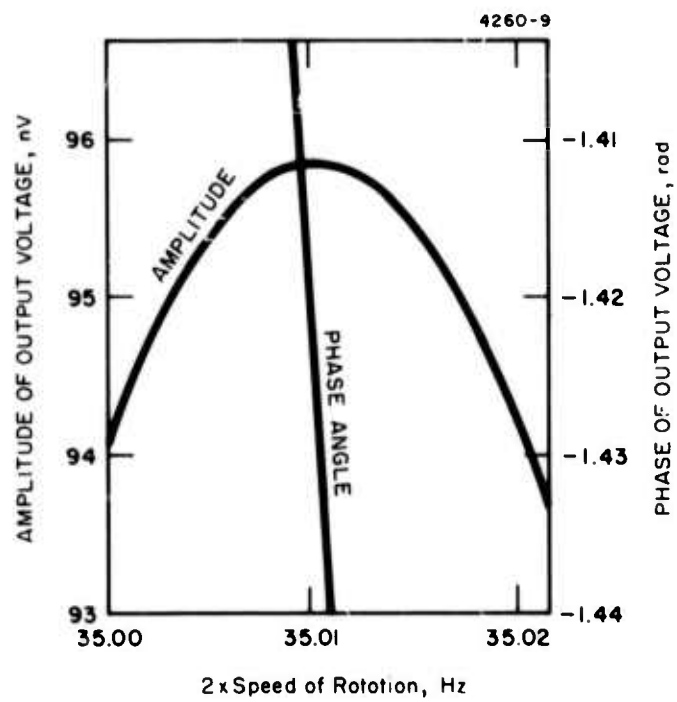


Fig. IV-D-10-1. Phase shift sensitivity.

sensor, it was deemed desirable to measure and compensate these coefficients to a reasonable level before the assembly was completed. It is known that these coefficients change slightly when the sensor is spinning in a vacuum at operating temperature. However, nonspinning tests are relatively simple and easy to make.

Nonspinning RGG error coefficients are measured and corrected by vibrating the Inner-Rotor of the RGG along various precisely defined axes at a frequency equal to the resonant frequency of the sensor. The precise test vibration is generated by aligning the thrust vectors of inertially loaded vibration exciters through the center of percussion of the RGG sensor and its mount. The RGG mount is a 1 m x 1 m x 0.6 m granite block supported on air cushions with three degrees of freedom (Fig. (IV-E-1)). The mount on this support has a resonant frequency of about 1.5 Hz along or about any axis.

The level and direction of the mount and sensor vibration is measured by geophones. The test system was adjusted to accommodate linear accelerations of 0 to 20 mg and angular accelerations of 0 to 0.4 rad per second squared. Alignment and adjustments were made such that accelerations along or about the desired axes did not cross couple into any of the other axes by more than one percent.

Because of the design of the test procedure, the need for having an accurate indicated phase of the RGG response to an applied acceleration was not critical. However, due to the complexity of the system as a whole, it became necessary to write simple computer models of the vibration exciters, geophones, RGG sensor and the sensor internal electronics. The detailed test, error coefficient estimation and adjustment procedure is given in Appendix C. The results of these tests and corrections are discussed in detail in another section of this report.

F. Results of Nonrotating Tests and Adjustments

The assembled inner rotor portions of the sensor structure was placed in the test stand and subjected to linear vibrations and angular rates at the resonant frequency of the sensor. The "as fabricated"

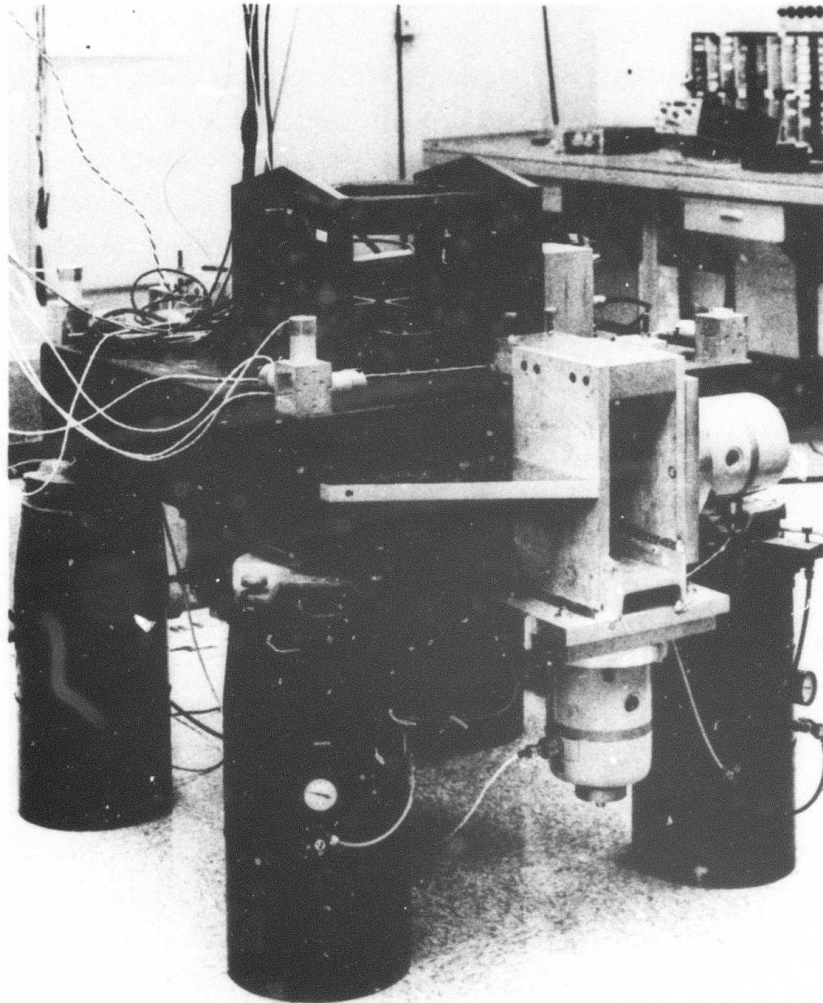


Fig. IV-E-1. RGG Sensor test fixture.

error sensitivities were high and as little as 10^{-4} g acceleration would cause a significant output. Only the first 6 error sensitivities could be measured at this level of output because the remaining sensitivities, being much smaller, were masked by the first six.

A period of debugging of the test facility and the sensor then took place. Some of the problem areas uncovered and corrected are listed below.

- Short gold leaf leads 1.3 mm wide by 0.05 mm thick from the transducer and balance tube contacts produced undesired coupling. They were replaced with 0.030 mm diameter gold leads with a large amount of slack. The wires were bent to produce a S shape and adjusted for radial orientation at the terminals to assure minimum torque coupling.
- Because cross coupling of the test table will introduce erroneous signals, the largest error sensitivities should be adjusted prior to attempting to measure the smaller error sensitivities.

After this learning and debugging period, the error sensitivities were "walked down" in a few test runs. A typical balance adjustment would improve the error sensitivities by a factor of 10. At this level of balance the error model (see Appendix C) developed for the sensor proved highly accurate in predicting response of the sensor to a given excitation in a given orientation. To excite these it was necessary to drive the sensor at 30 mg's. The accuracy estimates shown are estimates of the absolute value of the error sensitivity number obtained from different measurements, rather than the repeatability of one measurement. Many of the error sensitivities can be estimated by more than one combination of sensor orientation and excitation. (i. e., sensor response to vertical acceleration with spin axis up estimates $+K_3$, with spin axis down it estimates $-K_3$.) The accuracy estimates give the variance obtained from these independent estimates. Any one measurement was usually repeatable to 100 E. U.

As the error sensitivities were driven down, a few new effects were found that were not predicted by the sensor error model. These were in the form of shifts in the error sensitivity as a function of the

direction of gravity when the sensor was placed in different orientations. This was most dramatic in the case of the sum mode mismatch (K_6) error sensitivity. With the spin axis up, K_6 could be adjusted to less than 1000 E. U. $-s^2$, but with this adjustment the value with spin axis down was 170,000 E. U. $-s^2$. This in turn implied that in horizontal operation it would be 85,000 E. U. $-s^2$. A decision was made to adjust K_6 so that it was approximately +85,000 E. U. $-s^2$ in both the spin axis up and spin axis down position. (If there was no shift due to gravity loading, the response with spin up would have been opposite in sign to the response with spin axis down.) The response in the horizontal orientation would then be half the difference which in this case was 9,700 E. U. $-s^2$. We were thus optimizing the K_6 balance to have lower noise in horizontal operation rather than vertical orientation. Similar effects of g loading were seen in K_4 and K_5 and to a lesser extent in K_3 .

It is important to note that these g sensitive shifts were nearly instantaneous (in one test we reversed the spin axis and remeasured in 30 s) and there was no noticeable tendency for creep or shift with time at this level of balance.

At the termination of the static balance tests, the error coefficients measurable by this test condition, had all been reduced to less than a factor of 100 from the ultimate goal. (The goal represents a 0.1 E. U. noise contribution from that error source.) Further reduction of the error sensitivity coefficients in the future, require tests under rotating operation due to the mass shifts that would be expected under centrifugal loading. However, the error coefficients reached in static balancing tests were more than sufficient to produce a sensor structure operable in both vertical and horizontal operation without signal saturation. See Table IV-F.

G. Rotating Test Performance

At the completion of the rough balancing of the sensor arms using the static test fixture, the sensor was assembled, mounted on

TABLE IV-F. STATIC BALANCE ERROR SENSITIVITIES

Error Sensitivity	Units	"As Fabricated"	Measured After Static Balancing	Goal After Dynamic Balancing	Factor to Go
Differential Arm Mass Unbalance	K_1 K_2	+110,000,000 +100,000,000	+360,000 \pm 70,000 -110,000 \pm 80,000	6,000 6,000	60 18
Axial Vibration Torsional Sensitivity	K_3 (hor.) K_3 (vert.)	+10,000,000	+650,000 \pm 140,000 +550,000 \pm 140,000	10,000 10,000	65 55
Dynamic Arm Mass Unbalance	K_4 (vert.) K_4 (hor.) K_5 (vert.) K_5 (hor.)	+1,400,000 -1,000,000	-2,000 \pm 500 -14,500 \pm 500 +2,300 \pm 500 -12,400 \pm 500	300 300 300 300	7 48 8 41
Sum Mode Mismatch	K_6 (horiz. min) K_6 (vert. min.) K_6 (vert. mean)	-8,000,000	+9,700 \pm 1,700 -1,000 \pm 500 +83,200 \pm 1,700	300 300 N/A	32 3 -
Prime Anisoclasticity	K_7 K_8		+38,000 \pm 15,000 ~0 \pm 160,000	500 5	6 1
Cross Anisoclasticity	K_9 K_{10}		~0 \pm 160,000 -170,000 \pm 110,000	2,000 2,000	1 85
Spin/Torsion Skew Misalignment	K_{11} K_{12}		N/A Static Tests N/A Static Tests	200,000 200,000	- -
Transducer	K_{13}		+200,000 \pm 10,000	6,000	33

an interim set of ball bearings, and tested for the first time under normal rotational operation in 11 April 1975.

Since the initial rough balancing operation had not included balancing of the skew misalignment and anisoelastic error coefficients, and had left the remaining error sensitivities one to two orders of magnitude from the desired goals, and since the interim ball bearings were audibly louder than the hydrodynamic oil bearings, we expected a significant bias level, especially in horizontal operation. If we assume that the ball bearings would produce accelerations of 10^{-1} to 10^{-2} g at $1\omega_s$, $2\omega_s$ and $3\omega_s$, we would expect biases of 10,000 to 50,000 E. U. in vertical orientation and 100,000 to 500,000 E. U. in horizontal operation. The ball bearing noise level was also quite variable and we expected a significant variation in those bias levels.

The actual experimental results at the first turn-on of the roughly balanced sensor on the interim ball bearings was

<u>Orientation of spin axis</u>	<u>Bias, E. U.</u>	<u>10 s noise level, E. U.</u>
Vertical	25,000	300
Horizontal	300,000	400

Since these noise levels are only 1% or less of the bias levels, tests can now be carried out on the test table with the rotating sensor to determine the values of the error coefficients under rotation. We can then proceed with one or two iterations of the final balancing with the interim ball bearings while awaiting fabrication and delivery of a set of hydrodynamic oil bearings.

To reach the desired goals of

<u>Orientation of spin axis</u>	<u>Bias</u>	<u>Noise</u>
Vertical	<200 E. U. (including lab masses)	<1.0 E. U.
Horizontal	<5000 E. U. (including earth background and lab masses)	<1.0 E. U.

from the present bias and noise levels, will require the replacement of the interim ball bearings with the proper hydrodynamic oil bearings and 3 to 4 iterations of balancing, each reducing the bias and noise by a factor of approximately 5. Each iteration, which involves carrying out a series of rotational tests, disassembling the sensor, adjusting the balancing screws, trimming the anisoelastic slots, redoing the rough static balance, and reassembling the sensor, will require about 6 weeks.

V. CONCLUSIONS AND RECOMMENDATIONS

The individual technical achievements which contributed to the overall success of this program speak well for themselves; they need not be enumerated again in this chapter. The technical challenge of building a gravity gradiometer capable of operating in a moving vehicle was known to be difficult from the outset. The degree of realized success is a tribute to the technical skills and convictions of the small team who contributed so many hours to this effort and to the support of the DoD agencies involved in the contract funding and management.

The program philosophy, or *modus operandi*, proved successful, i. e., the concept of spending time with each component, assembly or subsystem until performance specifications were met or, at least until the shortcomings were evaluated. Thus, when the RGG was first assembled, the unknown aspects were bounded. The most dramatic example of this occurred when it became necessary to resort to the use of substitute spin bearings when the RGG was first demonstrated in April 1975. The RGG operating performance was predictably degraded but the noise level still was remarkably low considering the known, large noise source attributed to the substitute ball bearings.

It is particularly exciting and reassuring to realize that the magnitude of the remaining known and unknown error contributors are bounded. Contrary to the test results obtained with the first hard bearing RGG in 1971, the output of the Prototype RGG is both stable and repeatable. Equally dramatic is the fact that the sensor noise levels (short term variations in the bias) are approximately the same for the horizontal spin axis orientation as for the vertical.

The performance results are more than promising. When performance results are combined with the wealth of knowledge gained, assurance is provided that the program has accomplished what could be expected from it. Thus, these end products of the Prototype RGG program warrant not only a continuation, but an acceleration of the development effort in FY 76 and beyond.

The recommended program for the next phase of the RGG Development should emphasize three principal areas of investigation: sensor, component and sensor system application tasks.

The first category will include fabrication of a second, identical sensor, complete with external electronics. This will permit independent or simultaneous laboratory testing of two assembled RGG sensors. The testing tasks will include modification, trimming, adjustment and calibration in both spinning and non-spinning conditions. Certain critical spares should be provided, including an assembled Inner Rotor/Sensing Assembly, spin bearings, transducers and balance tubes.

The second category, component development, will include continued investigations on items such as: spin bearings, balance tubes, transducers, thermal analysis and control, vacuum requirements, and adjustment techniques such as those which provide skew axis/spin axis coincidence and which minimize the Yankee screwdriver effect. Also included will be the addition of more logic circuitry and the full cap driver capability. Lastly in this category, will be increased capability for off-line data reduction, improved documentation, and analytical assistance, including liaison with Dr. DeBra and with the Analytical Sciences Corporation.

The system application tasks will concern preliminary investigations of the airborne mapping mission. A survey of suitable USAF aircraft and platforms will be made. Liaison with platform vendors and commercial instrumentation companies will be established. These tasks are necessary to prepare for the ultimate goal of evaluating the RGG under airborne conditions.

APPENDIX A

ARM/PIVOT ATTACHMENT DESIGN CONSIDERATIONS

ARM-PIVOT ATTACHMENT DESIGN CONSIDERATIONS

Design of the arm plate to torsion pivot attachment requires consideration of a number of factors. The important design objectives were:

- Withstand shock and torque loads over the storage environmental temperature range
- Provide very precise angular alignment of the pivot structure to the spin-bearing rotor axis to minimize the "skew" sensitive error
- Provide precise angular alignment of the arm assembly's principal axes to the pivot structure to minimize arm dynamic unbalance error
- Provide stable positioning of the arms relative to the pivots to minimize the "differential" and "axial" mass unbalance shifts
- Attachment method to result in a high, stable mechanical system "Q" which implies high pressure clamping forces over clamping area, but with little or no areas of low pressure which might allow sliding or rubbing
- Design must be mechanically compatible (no geometrical interference) with radial balance devices, transducer stand-off pins, and the assembly sequence.
- Heat-shrink assembly techniques are limited by relatively low maximum temperature limit of 160°F of the radial and axial balance devices if, for lack of accessibility, they must be subjected to high temperatures
- Pivot material should have a low thermal coefficient of shear modulus to minimize sensor resonant frequency variation
- Design for minimum sensor overall size and weight.

- For the first prototype sensor, it is especially desirable to provide for ease of assembly/disassembly.

All of the attachment methods which have been considered are based on a basic continuous pivot structure which is "necked-down" in the area where the desired torsion spring rotation is to take place. The non "necked-down" portions are then the attachment areas of the structure. The single-piece structure provides structural integrity and is most likely the best configuration, in terms of fabrication ease, for attainment of concentricity and straightness of the torsion bar system.

The attachment methods considered fall into three basic categories; interference fits between the pivot bosses, clamping techniques, and use of high-strength bonding agents.

A. Interference Fits

There are several methods considered to obtain interference fits. The amount of interference required for a nominal cylindrical pivot boss of 5/16 in. diameter by 5/16 in. long has been estimated to be approximately 0.0001 in. diametral. With this amount of interference the holding torque would be approximately 8.5 in.-lbs per boss. The torsion stress induced in a Be-Cu pivot of 0.06 in. diameter due to the above holding torque would be approximately 200,000 psi which is about double its ultimate shear stress, and thus provides adequate margin.

This amount of interference can be obtained three ways for a cylindrical boss.

1. Press the Arm onto the Pivot

The force required to press is estimated to be 54 lbs which results in 19,000 psi stress in the 0.06 in. diameter pivot. Although the Be Cu pivot, whose ultimate tensile strength is 175,000 psi, would not yield under this load, great care would be required in the

pressing operation to prevent bending of the pivot. Additionally, this approach is not desirable due to the difficulty of disassembly, possible galling of parts, and probably nonrepeatable positioning upon reassembly.

2. Differential Heating/Cooling

This technique removes the high stresses of assembly by heating the arm and cooling the pivot boss such that when temperature equilibrium is reached, the desired interference is obtained. This technique would undoubtedly require special assembly fixtures to move the parts together to provide proper alignment after the very rapid thermal equilization is obtained. This technique has the same additionally undesirable features as mentioned for method 1 above.

3. Differential Expansion on Heating

Provided the arm material's thermal expansion coefficient is larger than that of the pivot, the parts can be heated simultaneously to a high temperature, assembled with zero clearance at the assembly temperature, and then cooled. Thus, at operating temperature, the larger thermal contraction of the arm material provides the "interference" fit required.

This technique eliminates the problems of methods 1 and 2. Disassembly and reassembly is easily accomplished by reheating to the zero clearance temperature. The temperature change required to obtain a 0.0001 in. diametral interference is -85°F (-47°C). Thus, for the nominal sensor operating temperature of 110°F , the structure would have to be heated to 195°F . This temperature exceeds the maximum upper limit of 160°F for the balance devices. In the present design, the radial balance devices are mounted to the inner arm plate, between the inner arm plate and the Main Support Plate; they must be installed (and preferably connected electrically) prior to assembly of the arm to the pivot. Hence, this arm-pivot assembly technique is not compatible with the present design.

4. Taper-Press Technique

This approach, although valid for many applications, is not suitable here. Galling of the aluminum would likely occur on disassembly. The axial spacing between the upper and lower arm plates is set by the axial length of the malleory end masses. Providing two precision taper attachment joints which "seat" at just the right position and which maintain the proper axial spacing for the end masses would require ultra machining precision, very likely beyond the state-of-the-art.

5. Hydraulically Pressurized Hollow Pivot

In this technique, a hollow pivot would be fabricated by sweat-brazing together hollow pivot-boss subassemblies. The assembled pivot then would be "final ground" to assure precise concentricity and boss diameters. This assembly would then be mounted to the Main Support Plate. The Arm Plates, End Masses, End Plates, etc. would be installed and jugged for alignment. Finally, the hollow pivot would be pressurized, creating a radial expansion of the pivot bosses, thus providing a clamping or equivalent "interference fit". Alternately, to generate the clamping force, the hollow pivot would be poured with a liquid material which expands upon setting.

This approach, although attractive in many respects, would undoubtedly require a large development effort and, therefore, has not been given further consideration.

B. Clamping

"Clamping" as used here refers to attachment methods which utilize screw-type fasteners which provide ease of disassembly. Several methods have been considered.

1. Flange Mount

This is the concept which is depicted in the current RGG drawing set. The arms and End Plates are all fastened to flanges made

as an integral part of the pivot. Centering of the arm plates and End Plates is accomplished by assuring zero clearance fits between the outside diameter of the flange and the counterbase area of the arm/end plate into which the flange is inserted. Screws are used to attach the arms/end plates to the flanges.

This design provides the required disassembly but does not provide for positive "centering" if the temperature of the assembly is raised above the temperature at which the zero clearance temperature occurred. This difficulty, due to the higher thermal expansion coefficient of aluminum over BeCu, could be overcome if similar materials for the arm and pivot were used.

2. Miscellaneous

Several alternate clamping methods have been considered. All but the above required increasing the sensor's overall length to provide for access for "split clamps" type clamping techniques or depended upon the use of precision-type threaded pins to act as clamping wedges. These types of clamps had the disadvantage of applying nonsymmetric clamp forces thus resulting in lateral displacement of the joint by unpredictable amounts and ensuing skew-axis misalignment errors.

C. High Strength Bonding Techniques

Use of the high strength plastic bonding agents for providing the method of arm-pivot attachment has been avoided for several reasons. Their modulus of elasticity is relatively low and highly variable with temperature. It has been suspected, in some of our earlier designs, that epoxy bonds had a tendency to work under load and, due to their relatively low "Q", reduce the sensor's overall "Q". Also, it has been suspected that the material's "Q" varied with aging. These apparent unstable material characteristics, together with the difficulty of dissolving or removing the cement for disassembly have led us to consider other, metal-to-metal attachment methods, more favorably.



APPENDIX B

TEST OF TORSIONAL SPRING FOR ROTATING GRAVITY GRADIOMETER

RESEARCH REPORT 490

OCTOBER 1974

S. M. Wandzura
Exploratory Studies Department

TABLE OF CONTENTS

I	BACKGROUND AND PURPOSE	1
II	APPARATUS	2
III	PROCEDURE	10
IV	RESULTS	12
V	CONCLUSIONS	14
	ACKNOWLEDGMENTS	15
	REFERENCES	16

LIST OF ILLUSTRATIONS

FIGURE		PAGE
1	Torsional spring test assembly	3
2	Torsional spring test assembly (side view)	4
3	Torsional spring test assembly (top view)	5
4	Torsional spring test assembly (disassembled)	6
5	Phase-sensitive detector schematic	7
6	Frequency measurement block diagram	8
7	Experimental setup	9
8	PSD output	11
9	Decay measurement	11

I. BACKGROUND AND PURPOSE

A new gravity gradiometer is now under construction at Hughes Research Laboratories. This device is a more sophisticated version of the one shown in Misner, Thorne, and Wheeler.¹ One of the new features of the gradiometer is the nature of the torsional springs used. Four springs consisting of small aluminum cylinders, machined out of the same piece of metal as the adjacent gradiometer arms, will be employed.

The resonant frequency of the device is critical and must be very close to 35 Hz. The frequency is determined by the inertia of the arms and the spring constant of the torsional springs. The inertias of the arms are easily calculated and controlled by tight fabrication tolerances, but the spring constant of the torsional spring is less easily calculated and controlled, providing a potential source of error. These springs are intended to have low damping, since the damping in the gradiometer is designed to be entirely limited by the piezoelectric pickup. The Q of the resonance in the final device will be 300, corresponding to a damping coefficient

$$\beta = 5.0 \times 10^3 \text{ g cm}^2 \text{ s}^{-1}$$

(for each spring), so that the damping coefficient of a spring alone should be much less than the above value.

The purpose of this experiment was to measure the spring constant of a test spring assembly manufactured especially for this purpose and to place an upper bound on the damping coefficient. These data were needed to obtain the precise dimensions for the final machining operation of the actual gradiometer.

II. APPARATUS

The test assembly consisted of two separate pieces of 6061-T6 aluminum as shown in Figs. 1 through 4. Section A was a separate piece, bolted onto section C with machine screws.

The pickup consisted of a magnet held onto a bolt in section A, and a coil attached to section F with double-backed adhesive tape. The coil consisted of a Microtran MMT 4-FB miniature transformer with notches sawed through the core to increase the magnetic flux linkage with the magnet. The output of the coil was amplified by an Applied Cybernetics Model LA260VF Low Noise Preamplifier (battery powered). The signal was then processed by a phase-sensitive detector (PSD) constructed for the experiment. The circuit for the PSD is shown in Fig. 5. The reference frequency was supplied by a General Radio Type 1161-A Coherent Decade Frequency Synthesizer. The output of the PSD was observed on a Tektronix Type 502 Dual Beam Oscilloscope, with the horizontal amplifier triggered by the frequency synthesizer. This is diagrammed in Fig. 6.

The test assembly was used in two configurations. In the first, the entire assembly was suspended by a point along its axis. Measures taken to minimize external coupling include using the suspension wire for grounding and careful hanging of the thin (28 AWG) pickup leads. This configuration is pictured in Fig. 7. In the second configuration, the bottom disk (F) was bolted to a 30.5 x 30.5 x 2.54 cm steel plate which rested on the laboratory table, thus giving one side of the system an essentially infinite moment of inertia. This configuration had the advantage of no mechanical coupling to the moving part of the system other than through the spring (and air friction).

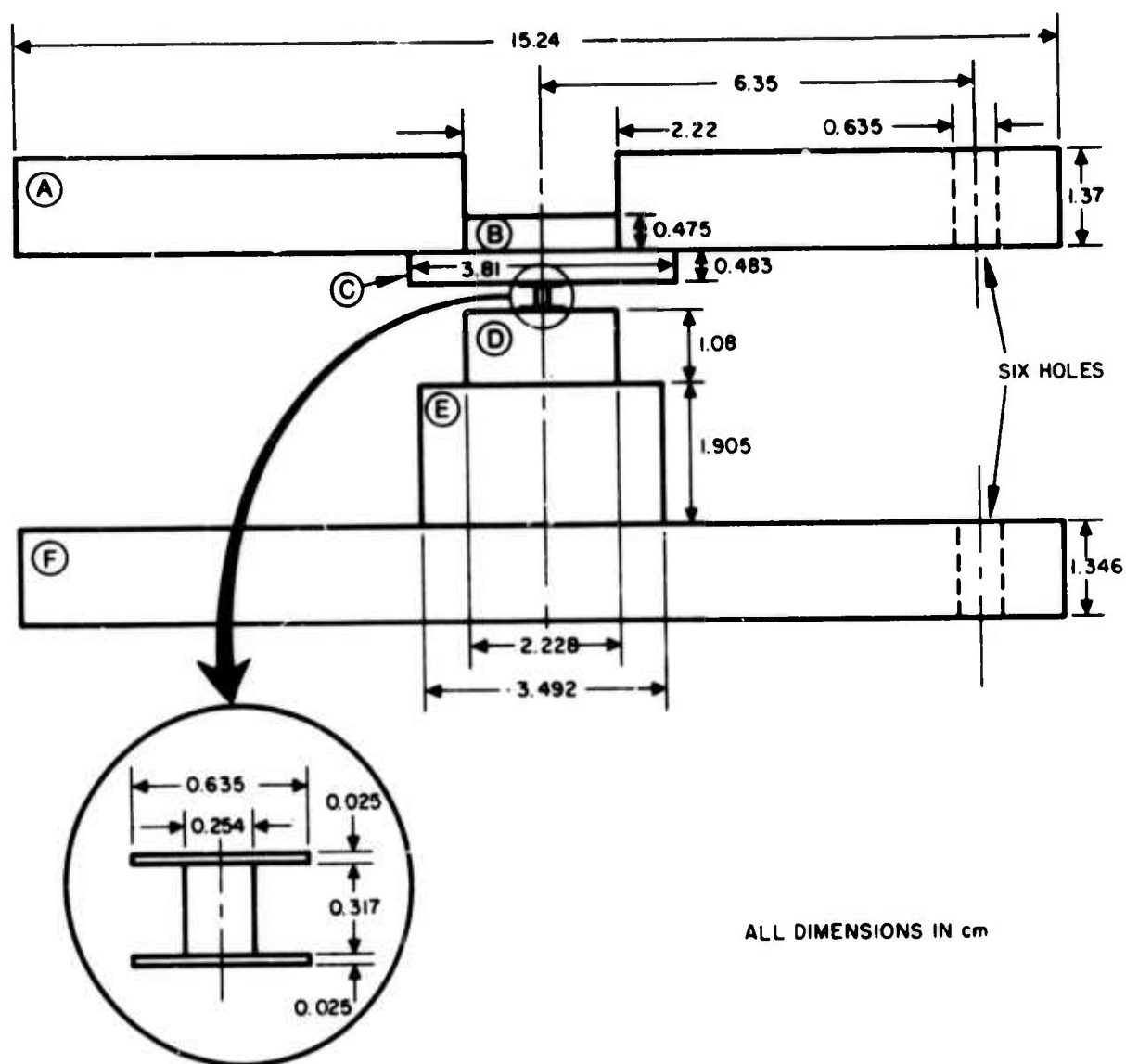


Fig. 1. Torsional spring test assembly.

M10491.

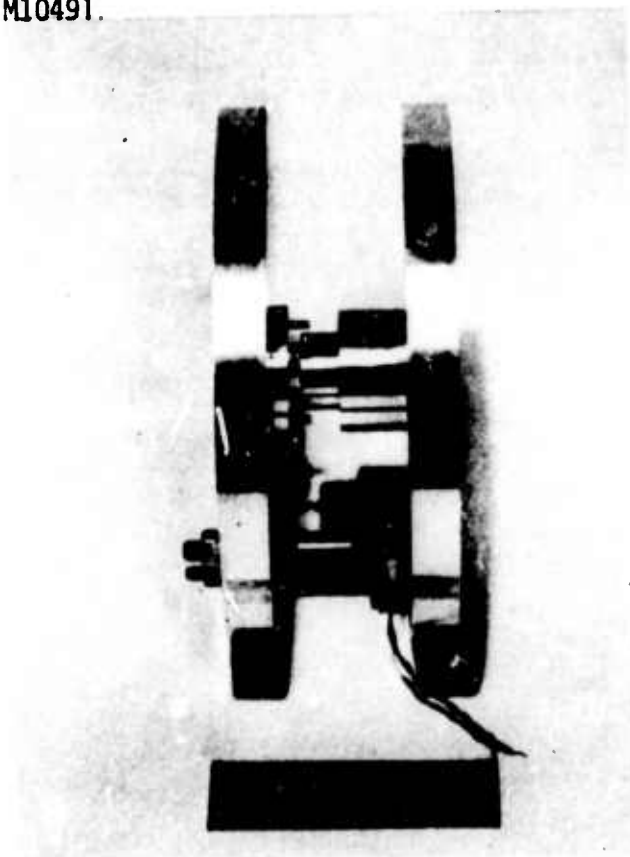


Fig. 2. Torsional spring test assembly (side view).

M10489

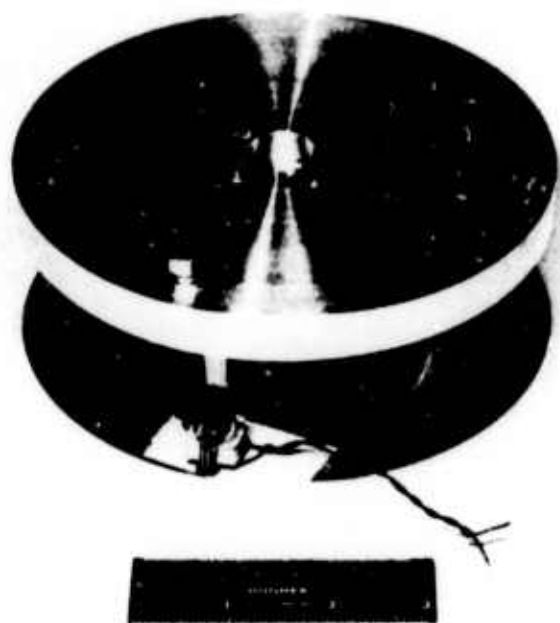


Fig. 3. Torsional spring test assembly
(top view).

M10490

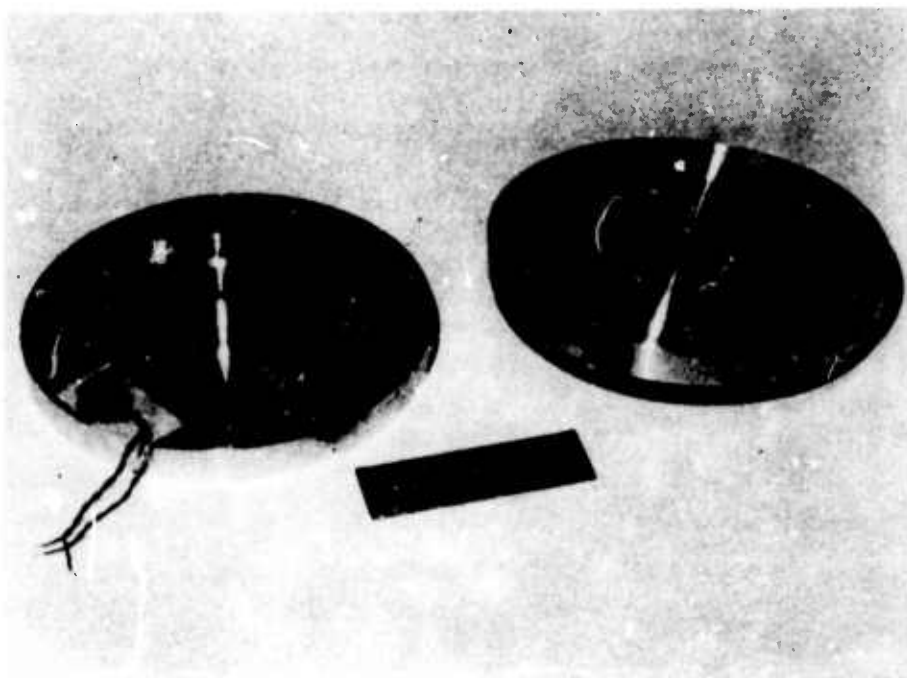


Fig. 4. Torsional spring test assembly (disassembled).

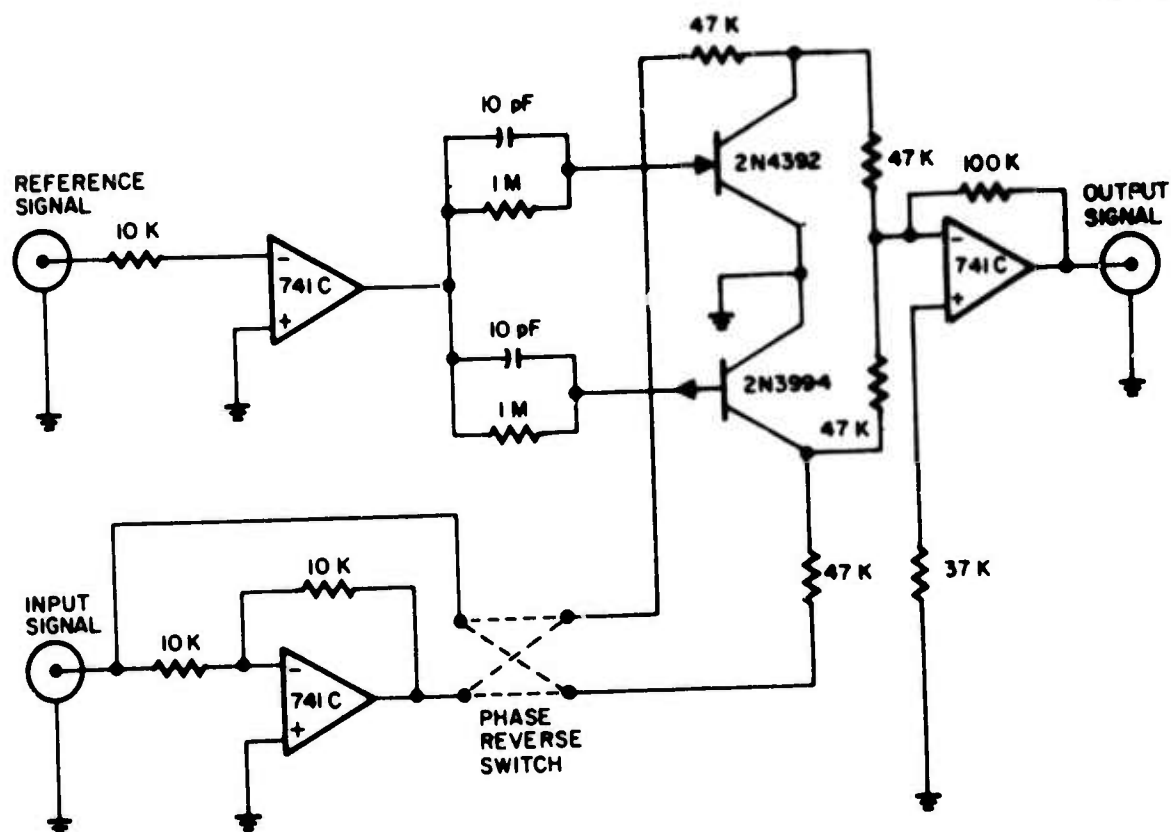


Fig. 5. Phase-sensitive detector schematic.

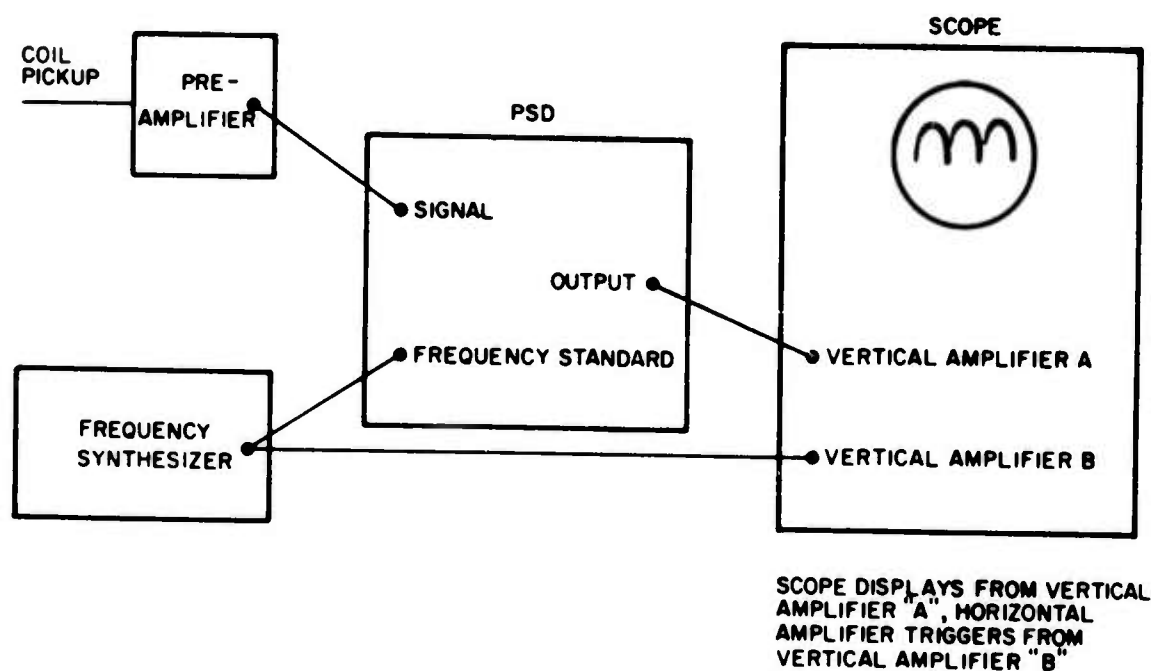


Fig. 6. Frequency measurement block diagram.

M10492

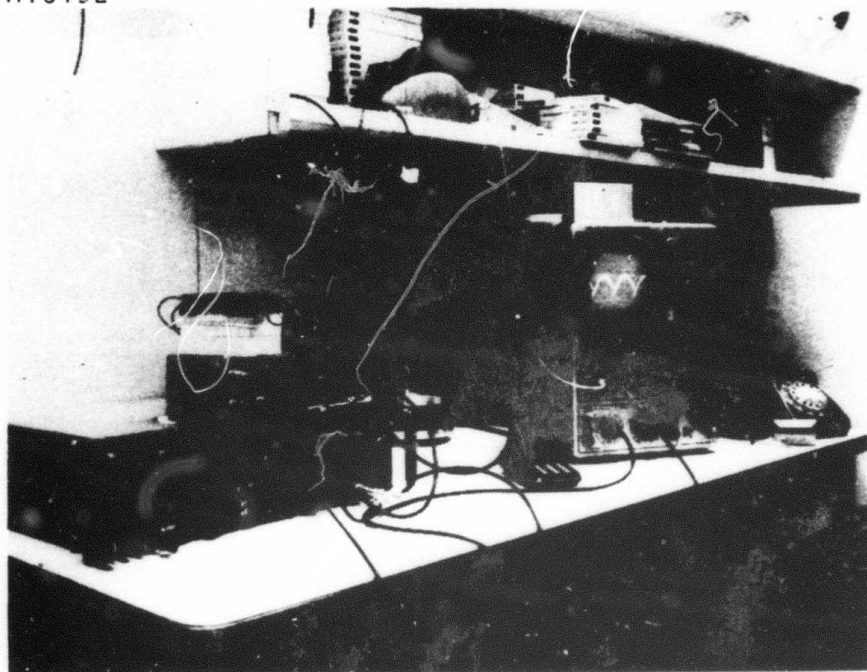


Fig. 7. Experimental setup.

III. PROCEDURE

The measurement of the spring constant was made by measurement of the resonant frequency of the torsional mode of the test assembly. The oscillation was excited very carefully by swatting the apparatus with a screwdriver handle. By adjusting the frequency to make the displayed pattern nearly constant (Fig. 8), the frequency of oscillations could be measured to the accuracy of the synthesizer,* because of the long decay time of the system.

The upper limit on the damping coefficient was obtained by measuring the decay time of the oscillation. This was accomplished by connecting the output of the preamplifier directly to the oscilloscope, using the slowest horizontal sweep available, 5.3 s/cm (Fig. 9), and photographing the scope trace. The decay time (time that the energy in the oscillations decays by 1/e) is given by

$$\tau_d = \frac{t_2 - t_1}{2 \ln \frac{A(t_1)}{A(t_2)}}$$

where $A(t)$ is the amplitude of the oscillation. The time scale of the oscilloscope was calibrated with the synthesizer.

*The accuracy of the synthesizer was checked against the power line frequency and found to agree within ± 0.01 Hz in the range 10 to 60 Hz.

3628-4

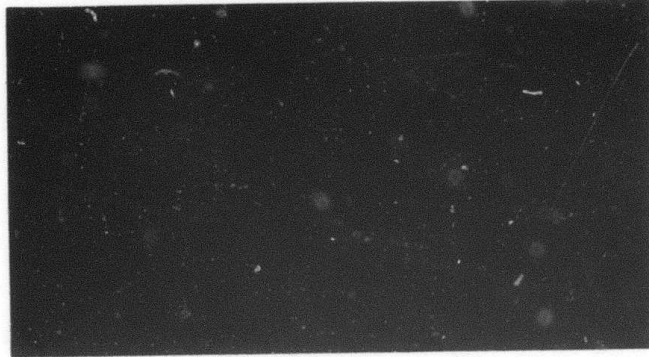


Fig. 8. PSD output.

3628-5

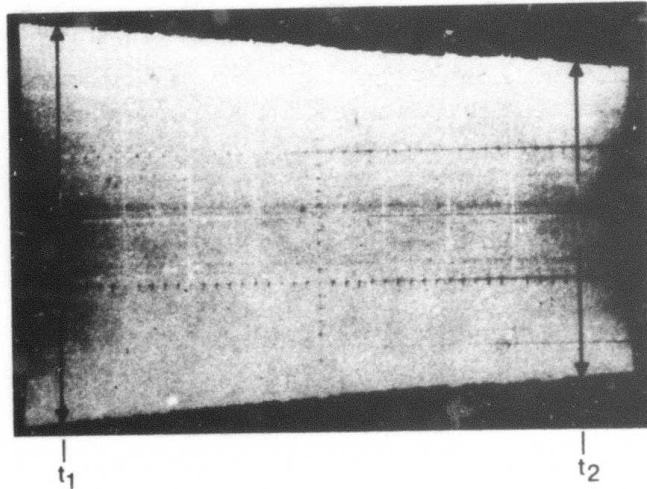


Fig. 9. Decay measurement.

IV. RESULTS

The spring constant is given by

$$\kappa = I\omega^2$$

where (in the case of the first configuration) I is the reduced moment of inertia

$$I = \frac{I_1 I_2}{I_1 + I_2}$$

(I_1 and I_2 are the moments of the top and bottom parts of the assembly) and $\omega = 2\pi f$ is the measured resonant frequency. Using the formula for the moment of inertia of a disk about its axes

$$I = \frac{1}{2} \pi \rho H R^4$$

where ρ is the density, H the thickness and R the radius of the disk, we find (with $\rho = 2.702 \text{ g cm}^{-3}$) that the moments of inertia of the upper and lower halves of the test assembly (excluding appendages) are $1.93 \times 10^4 \text{ g cm}^2$ and $1.91 \times 10^4 \text{ g cm}^2$, respectively.

In both configurations the moment of inertia of the magnet and its mounting bolts on the upper disk about the axis ($I = MR^2$) was $1.52 \times 10^3 \text{ g cm}^2$. In the first configuration the transformer added to the lower disk had a moment of 332 g cm^2 .

In the first configuration, the measured frequency was 26.15 Hz. Using the above formulae, this results on a spring constant

$$\kappa = 2.714 \times 10^8 \text{ g cm}^2 \text{ s}^{-2}.$$

In the second configuration, the measured frequency was 18.27 Hz. This gave

$$\kappa = 2.749 \times 10^8 \text{ g cm}^2 \text{ s}^{-2}.$$

The accuracy in these values is limited by the values of the moments of inertia. The errors here are estimated to be $\pm 2\%$. We thus conclude that the two results are consistent with each other. The frequency measurements were repeatable to $\pm 0.2\%$ through disassembly and reassembly of the apparatus.

Measurement of the damping coefficient (decay time) proved to be impossible with the available apparatus. Unavoidable variations in the various contributors to the damping such as lead wires and softening of the threads on the aluminum where the top disk was bolted onto the assembly prevented consistent measurement of the decay time. The longest decay time (measured on the second configuration, as expected) was 84 s (Fig. 9). This was used to place an upper bound on the damping coefficient

$$\begin{aligned} \beta &= \frac{I}{\tau_d} \\ &\leq 250 \text{ g cm}^2 \text{ s}^{-1}. \end{aligned}$$

This upper bound corresponds to a Q given by

$$\begin{aligned} Q &= \omega \tau_d \\ &= 9300. \end{aligned}$$

V. CONCLUSIONS

The spring constant measurement gave a value approximately 25% less than the result obtained from the standard calculation for an infinite cylinder²:

$$k = \frac{Gr^4}{2l} = 3.33 \times 10^8 \text{ g cm}^2 \text{ s}^{-2}$$

where $G = 2.58 \times 10^{11} \text{ g s}^{-2}$ is the shear modulus of the material, r is the radius of the cylinder, and l is the length. The difference is attributed to end effects in the disks at the junction with the spring ends. The discrepancy is in good agreement (in both magnitude and direction) with an estimate of the end effect. The compliance of the spring is proportional to Gr^4/l , while the compliance due to the end effects must be (by dimensional analysis) proportional to Gr^3 . The ratio of compliance is thus l/r and the fractional change of the spring constant is $O(r/l)$. We have $r/l = 0.4$, so the decrease in spring constant from the infinite cylinder calculation by 23% is consistent with what is expected from the edge effect. (That the effect causes increased compliance is obvious.)

To measure the intrinsic damping of the spring, more elaborate apparatus would be necessary, probably including a vacuum jar. Because the upper bound established was far below that needed for proper operation of the gradiometer, further experiments to determine the damping constant were not attempted.

On the basis of the measurements made on this test program, the pivot dimensions on the drawings for the actual sensor were revised so that the sensor resonant frequency would be the desired 35 Hz.

VI. ACKNOWLEDGMENTS

This work was performed for the Exploratory Studies Department of the Hughes Research Laboratories, Malibu, California. The author wishes to thank Dr. Robert L. Forward for providing the opportunity to do this work.

REFERENCES

1. C. Misner, K. Thorne, and J. Wheeler, Gravitation, (W.H. Freeman, San Francisco, 1973), p. 401.
2. Raymond J. Roark, Formulas for Stress and Strain, (McGraw Hill New York, 1965), pp. 191, 416.

APPENDIX C

ERROR COEFFICIENT ESTIMATION AND
COMPENSATION OF THE NONSPINNING RGG

R. W. Peterson
September 1974

TABLE OF CONTENTS

INTRODUCTION	C-5
LINEARIZED INPUT/OUTPUT EQUATION	C-5
ERROR COEFFICIENT ESTIMATION	C-10
ADJUSTMENT INFLUENCE EQUATIONS	C-14
APPENDIX C-I - SIMPLIFIED TEST AND ESTIMATION	C-27
APPENDIX C-II - ERROR COEFFICIENT DEFINITIONS	C-33
NOMENCLATURE	C-35
REFERENCES	C-39

ERROR COEFFICIENT ESTIMATION AND COMPENSATION OF THE NON-SPINNING RGG "INNER-ROTOR"

INTRODUCTION

Vibration tests of the non-spinning RGG* "inner-rotor" assembly are planned for the purpose of preliminary error coefficient estimation and compensation. The estimation process is based on the linearized relations between "inner-rotor" vibration inputs and the correlated changes that result in the RGG signal process outputs. The compensation process is limited to RGG arm mass distribution adjustments and "anisoelastic trimming." The purpose of this memorandum is to develop the linearized input/output equations for the estimation process and to develop the adjustment-influence equations for the compensation process. In addition, the basic estimation equations are developed, and a simplified estimation process is described.

LINEARIZED INPUT/OUTPUT EQUATIONS

The linearized input/output equations for the non-spinning inner-rotor may be derived from the RGG total differential moment equation which includes both signal and the various motion-sensitive error moments which are documented in the references. The total differential moment equation is presented as (1) and includes the following differential moments:

Differential arm mass unbalance (K_1 , K_2)

Axial vibration sensitivity (K_3)

Dynamic arm mass unbalance (K_4 , K_5)

Sum mode mismatch (K_6)

Prime anisoelasticity (K_7 , K_8)

*Rotating Gravity Gradiometer

Cross anisoelasticity (K_9, K_{10})

Gravity gradient

Rotational field

Spin/torsion misalignment (θ_i, θ_j)

The relations between the error coefficients, K_1 through K_{10} , and the physical parameters are defined in Appendix C-II.

$$\begin{aligned} \frac{\Delta L_k}{\eta C} = & K_1 \left(\frac{a_i}{g} \right) + K_2 \left(\frac{a_j}{g} \right) + K_3 \left(\frac{a_k}{g} \right) + K_4 [\dot{\omega}_i - \omega_j \omega_k + \Gamma_{jk}] \\ & + K_5 [\dot{\omega}_j + \omega_i \omega_k - \Gamma_{ik}] + K_6 \dot{\omega}_k \\ & + K_7 \left[\frac{2a_i a_j}{g^2} \right] + K_8 \left[\frac{a_j^2 - a_i^2}{g^2} \right] + K_9 \left[\frac{a_j a_k}{g^2} \right] \\ & - K_{10} \left[\frac{a_i a_k}{g^2} \right] + [2\Gamma_{ij} - 2\omega_i \omega_j] + 2\omega_s [\theta_j \omega_j - \theta_i \omega_i] \\ & + \left[\frac{\Delta \Phi_{ij}}{\eta C} \right] [\Gamma_{ii} - \Gamma_{jj} + \omega_j^2 - \omega_i^2] \end{aligned} \quad (1)$$

When the non-spinning inner-rotor is angularly and linearly vibrated at the differential mode resonant frequency and this frequency is employed in the signal detection process, the DC and non-linear vibration terms in (1) will not influence the average output of the RGG signal process. The significant linear terms in (1) constitute the "effective-inputs" to the RGG signal process as described by (2).

$$\begin{aligned}
\epsilon \triangleq & [K_1 - 2K_7 C_{jg} + 2K_8 C_{ig} + K_{10} C_{kg}] n_i \\
& + [K_2 - 2K_7 C_{ig} - 2K_8 C_{jg} - K_9 C_{kg}] n_j \\
& + [K_3 - K_9 C_{jg} + K_{10} C_{ig}] n_k \\
& + K_4 \dot{\omega}_i + K_5 \dot{\omega}_j + K_6 \dot{\omega}_k \\
& - 2\omega_i \Omega_j - 2\omega_j \Omega_i
\end{aligned} \tag{2}$$

where

$$C_{ig} \triangleq (\bar{i} \cdot \bar{g})/g$$

$$C_{jg} \triangleq (\bar{j} \cdot \bar{g})/g$$

$$C_{kg} \triangleq (\bar{k} \cdot \bar{g})/g$$

$$\Omega_i \triangleq \bar{i} \cdot \bar{\Omega}$$

$$\Omega_j \triangleq \bar{j} \cdot \bar{\Omega}$$

$$\bar{\Omega} = \text{Earth rate vector}$$

$$\bar{g} = \text{Gravity vector}$$

When the inner-rotor orientation is constrained to the three positions defined by the vertically positive direction of its reference axis, three "effective-input" equations are obtained from (2) as defined by (3), (4), and (5).

$$\begin{aligned}
\epsilon_i = & [K_1 - 2K_8] n_i + [K_2 + 2K_7] n_j + [K_3 - K_{10}] n_k \\
& + K_4 \dot{\omega}_i + K_5 \dot{\omega}_j + K_6 \dot{\omega}_k - 2\omega_i \Omega_j - 2\omega_j \Omega_i
\end{aligned} \tag{3}$$

$$\begin{aligned} \epsilon_j = & [K_1 + 2K_7] n_i + [K_2 + 2K_8] n_j + [K_3 + K_9] n_k \\ & + K_4 \dot{\omega}_i + K_5 \dot{\omega}_j + K_6 \dot{\omega}_k - 2\omega_i \Omega_v - 2\omega_j \Omega_{Hi} \end{aligned} \quad (4)$$

$$\begin{aligned} \epsilon_k = & [K_1 - K_{10}] n_i + [K_2 + K_9] n_j + [K_3] n_k \\ & + K_4 \dot{\omega}_i + K_5 \dot{\omega}_j + K_6 \dot{\omega}_k - 2\omega_i \Omega_{Hj} - 2\omega_j \Omega_{Hi} \end{aligned} \quad (5)$$

These equations describe the "effective inputs" to the RGG signal process, and they are periodic functions of the excitation frequency as defined by (6).

$$\epsilon_i \triangleq E_i \sin(\omega_e t + \phi_i) \quad (6)$$

The RGG signal process filters, detects, and averages the "effective-input" functions to produce the changes in the output of each RGG channel as defined by (7) and (8) where κ_0 and ϕ_0 represent the "effective" gain and phase shift of the RGG signal process.

$$\epsilon_{ci} \triangleq \kappa_0 E_i \sin(\phi_i + \phi_0) \quad (7)$$

$$\epsilon_{si} \triangleq \kappa_0 E_i \cos(\phi_i + \phi_0) \quad (8)$$

The output functions of (7) and (8) together with a priori knowledge of the effective gain and phase shift of the RGG signal process enable estimation of the "effective-input parameters" as defined by (9) and (10) where $\hat{\kappa}_0$ and $\hat{\phi}_0$ are estimates of the gain and phase of the signal process.

$$\hat{\epsilon}_{ai} \triangleq \left(\frac{\kappa_0}{\hat{\kappa}_0} \right) E_i \sin(\phi_i + \phi_0 - \hat{\phi}_0) \quad (9)$$

$$\hat{\epsilon}_{bi} \triangleq \left(\frac{\kappa_0}{\hat{\kappa}_0} \right) E_i \cos(\phi_i + \phi_0 - \hat{\phi}_0) \quad (10)$$

The actual input parameters are obtained from (6) and defined by (11) and (12).

$$\epsilon_{ai} \triangleq E_i \sin \phi_i \quad (11)$$

$$\epsilon_{bi} \triangleq E_i \cos \phi_i \quad (12)$$

Thus, the "effective-input" function and its estimate may be expressed as (13) and (14), respectively.

$$\epsilon_i = \epsilon_{ai} \cos \omega_e t + \epsilon_{bi} \sin \omega_e t \quad (13)$$

$$\hat{\epsilon}_i = \hat{\epsilon}_{ai} \cos \omega_e t + \hat{\epsilon}_{bi} \sin \omega_e t \quad (14)$$

The vibration functions are also periodic at the excitation frequency and may be expressed in terms of quadrature excitation parameters. As an example, consider the vibration function, n_i , to be defined by (15), where the excitation parameters are n_{ai} and n_{bi} .

$$n_i \triangleq n_{ai} \cos \omega_e t + n_{bi} \sin \omega_e t \quad (15)$$

After correction for the earth-rate-related terms, the estimated "effective-input parameters" and the measured "excitation parameters" provide the basis for estimating the error coefficients, K_1 through K_{10} . For this purpose, it is convenient to replace the

periodic functions in the "effective-input" equations by complex numbers composed of the input and excitation parameters. For example, the parametric representation of the periodic functions of (13) and (15) are defined by (16) and (17), respectively.

$$\epsilon_i \triangleq \epsilon_{ai} + j\epsilon_{bi} \quad (16)$$

$$n_i \triangleq n_{ai} + jn_{bi} \quad (17)$$

ERROR COEFFICIENT ESTIMATION

When the "effective-input" equations are expressed in parametric form, a set of linear equations is obtained. The "effective-input" is the sum of the error coefficients as weighted by the complex excitation parameters for a given orientation and excitation condition. The "effective-inputs" which result from several different excitation and orientation conditions may be combined to form a column vector of "effective-inputs," $\bar{\epsilon}$, that is linearly related to the error coefficient vector, \bar{K} , by the excitation matrix, \bar{E} , as in (18).

$$\bar{\epsilon} = \bar{E} \bar{K} \quad (18)$$

When a sufficient number of independent tests are conducted to develop a nonsingular excitation matrix, the error coefficient vector may be described in terms of the inverse excitation matrix and the "effective-input" vector as in (19).

$$\bar{K} = \bar{E}^{-1} \bar{\epsilon} \quad (19)$$

This equation provides a general basis for the estimation of the error coefficient vector from the "effective-inputs" and the excitations. To illustrate, let the estimate of the error coefficient vector, $\hat{\bar{K}}$, be related to the estimated "effective-input" vector, $\hat{\bar{\epsilon}}$, by the inverse excitation-measurement matrix, \bar{M}^{-1} , as in (20).

$$\hat{\mathbf{K}} \triangleq \overline{\mathbf{M}}^{-1} \hat{\mathbf{e}} \quad (20)$$

The measurement matrix may take many forms depending on the nature of the measurements; however, it must be non-singular if (20) is to have a solution. The quality of the error coefficient estimates will depend on the accuracy of both the "effective-input" estimates and the measurements. When both are exact, the estimate is exact as evidenced by (19).

In order to estimate all ten error coefficients, ten independent tests are required. This requirement leads to excitation and measurement matrices which are ten by ten in size. In general, these matrices are composed of sixty complex numbers (120 parameters). The "effective-inputs" consist of ten complex numbers (20 parameters); and if the gain and phase of the signal process differs for every test, an additional twenty parameters are required. The general estimation problem involves the storage and manipulation of 160 parameters!

Although it is possible to handle the general estimation problem with modern data processing techniques, this approach is not very practical from a laboratory-test point of view. For the present objective of minimizing the adjustable error coefficients, it is desirable to keep the test and estimation procedures as simple as possible.

The simplest estimation process is achieved when the excitation functions are limited to one parameter for each test condition. Under these circumstances, each "effective-input" is related to a single excitation parameter and at most two error coefficients. To illustrate this point, examine Table II of Appendix C-I which has been derived from (3), (4), and (5). Several of the error coefficients are directly related to the input/excitation ratios, and the remaining error coefficients can be separated by a fairly simple simultaneous solution of the appropriate input/excitation ratios.

When the mass unbalance error moments dominate the anisoelastic error moments, a further simplification is possible. In this case, the six condition test set defined by Table I of Appendix C-I may be employed to yield estimates of the first six error coefficients directly from the appropriate input/excitation ratios. Actually, the six tests are merely a triple repetition of two tests, i. e., vibration along the vertical and rotation about the vertical for each of the three "inner-rotor" cardinal orientations.

In order to consider the motion coupling influence in these simplified test and estimation processes, it is necessary to examine the estimation errors. These errors may be developed from (18) and (20) by writing the "effective-input" estimation error as (21).

$$\hat{\epsilon} - \bar{\epsilon} = \overline{\overline{M}} \hat{K} - \overline{\overline{E}} \bar{K} \quad (21)$$

Rearrangement of (21) yields the estimation error for the error coefficients as (22).

$$\hat{K} - \bar{K} = \overline{\overline{M}}^{-1} [(\hat{\epsilon} - \bar{\epsilon}) - (\overline{\overline{M}} - \overline{\overline{E}}) \bar{K}] \quad (22)$$

An important characteristic of (22) is the coupled influence of the measurement errors on the error coefficient estimates due to the true error coefficient vector, \underline{K} . This characteristic demonstrates how large error coefficients influence the estimates of smaller error coefficients through the measurement errors. This has practical significance in an iterative adjustment procedure if the non-adjustable error coefficients are so large that their measurement error products prevent satisfactory estimation of the adjustable error coefficients.

The simplified test and estimation processes of Appendix C-I are based on the concept of "pure excitation" functions. The co-existence of any other coherent excitation function produces an equivalent measurement error which degrades the error coefficient estimates according to the norm of the error coefficient vector. To illustrate this point, let's examine one scalar element of (22) as defined by (23).

$$\Delta K_i = \frac{1}{M_i} \left[\Delta e_i - \sum_j \Delta M_{ij} K_j \right] \quad (23)$$

If we assume statistical independence between the "effective-input" estimation errors and the measurement errors, the variance of the scalar error coefficient estimation error may be approximated as (24).

$$\sigma_{\Delta K_i}^2 \cong \left(\frac{1}{M_i} \right)^2 \left[\sigma_{\Delta e_i}^2 + \sum_j \sigma_{ij}^2 K_j^2 \right] \quad (24)$$

If the measurement error variances are all equal, (24) reduces to (25).

$$\sigma_{\Delta K_i}^2 \cong \left(\frac{1}{M_i} \right)^2 \left[\sigma_{\Delta e_i}^2 + \sigma_M^2 |\bar{K}|^2 \right] \quad (25)$$

The standard errors due to the "effective-input" estimation errors and due to the measurement errors taken separately are obtained from (25) as (26) and (27).

$$\sigma_{\Delta K_i} \Big|_{\Delta e_i} \cong \left[\sigma_{\Delta e_i} / M_i \right] \quad (26)$$

$$\sigma_{\Delta K_i} \Big|_{\Delta M} \cong \left[\sigma_M / M_i \right] |\bar{K}| \quad (27)$$

The influence of the norm of the error coefficient vector is indicated by (27) which suggests that a one percent measurement error causes an error coefficient estimation error of approximately one percent of the error coefficient vector magnitude. This demonstrates the large error coefficients influence on the estimates of the smaller coefficients.

In order to make proper balance adjustments for a given error coefficient estimation set, it is necessary to understand the adjustment influences on the error coefficients. These relations are described by the "adjustment influence" equations which are developed in the next section.

ADJUSTMENT INFLUENCE EQUATIONS

The present RGG balance adjustment configuration is constrained to produce mass shifts in planes which are nominally normal to the torsion axis, and the freedom of each individual adjustment is nominally parallel to one of the principal axes of inertia of each arm. Since the "adjustment planes" are displaced axially from the rotor "center plane," the first and second mass moment changes are coupled relative to the "rotor reference frame." This characteristic necessitates simultaneous consideration of both the differential and dynamic arm mass unbalance error coefficients when making these adjustments.

Each arm has adjustment screws which are either radially or tangentially adjustable. For analytical simplicity, it will be assumed that the adjustment screws will be moved in groups to produce mass moment changes parallel to the principal axes of arm inertia. The adjustable mass moments for each arm will be modelled in terms of the radial and tangential components as defined by (28) and (29).

$$\bar{p}_1 \triangleq \bar{i} p_{r1} + \bar{j} p_{t1} \quad (28)$$

$$\bar{p}_2 \triangleq \bar{i} p_{t2} + \bar{j} p_{r2} \quad (29)$$

The mass moments of (28) and (29) influence the differential axial-transverse second mass moments in proportion to the axial separation distance between the "like adjustment planes" of the two arms. In this model, the separation distances are designated as

"radial" or "tangential" and identified by d_r and d_t , respectively. The second moment influences are defined by (30) and (31) as a function of the first moments.

$$\delta(\Delta\Phi_{ik}) = -\frac{1}{2} d_r \delta p_{r1} - \frac{1}{2} d_t \delta p_{t2} \quad (30)$$

$$\delta(\Delta\Phi_{jk}) = -\frac{1}{2} d_r \delta p_{r2} - \frac{1}{2} d_t \delta p_{t1} \quad (31)$$

The differential arm mass unbalance influence is defined as the difference between (28) and (29) as shown in (32).

$$\delta p_d \triangleq \bar{i} (\delta p_{r1} - \delta p_{t2}) + \bar{j} (\delta p_{t1} - \delta p_{r2}) \quad (32)$$

The change in the differential mass unbalance coefficients due to the mass moments of (32) are expressed as (33) and (34).

$$\delta(K_1) = \frac{g}{\eta C} [\delta p_{t1} - \delta p_{r2}] \quad (33)$$

$$\delta(K_2) = \frac{g}{\eta C} [\delta p_{t2} - \delta p_{r1}] \quad (34)$$

In order to reduce the estimated differential mass unbalance coefficients, the changes should be equal and opposite to the estimates as shown in (35) and (36).

$$\hat{K}_1 \triangleq \frac{g}{\eta C} [\delta p_{r2} - \delta p_{t1}] \quad (35)$$

$$\hat{K}_2 \triangleq \frac{g}{\eta C} [\delta p_{r1} - \delta p_{t2}] \quad (36)$$

Similarly, the changes in the second moments influence the dynamic mass unbalance coefficients according to (37) and (38).

$$\delta(K_4) = \frac{1}{2\eta C} [d_r \delta p_{r1} + d_t \delta p_{t2}] \quad (37)$$

$$\delta(K_5) = \frac{1}{2\eta C} [d_r \delta p_{r2} + d_t \delta p_{t1}] \quad (38)$$

The estimates should be compensated according to (39) and (40).

$$\hat{K}_4 = \frac{-1}{2\eta C} [d_r \delta p_{r1} + d_t \delta p_{t2}] \quad (39)$$

$$\hat{K}_5 = \frac{-1}{2\eta C} [d_r \delta p_{r2} + d_t \delta p_{t1}] \quad (40)$$

The radial and tangential mass moments should be adjusted to satisfy (35), (36), (39), and (40) simultaneously. This leads to the adjustment requirements stated in (41) through (44).

$$\delta p_{r1} = \eta C \left[\left(\frac{d_t}{d_r + d_t} \right) \left(\frac{\hat{K}_2}{g} \right) - \left(\frac{2}{d_r + d_t} \right) \hat{K}_4 \right] \quad (41)$$

$$\delta p_{t1} = \eta C \left[- \left(\frac{d_r}{d_r + d_t} \right) \left(\frac{\hat{K}_1}{g} \right) - \left(\frac{2}{d_r + d_t} \right) \hat{K}_5 \right] \quad (42)$$

$$\delta p_{r2} = \eta C \left[\left(\frac{d_t}{d_r + d_t} \right) \left(\frac{\hat{K}_1}{g} \right) - \left(\frac{2}{d_r + d_t} \right) \hat{K}_5 \right] \quad (43)$$

$$\delta p_{t2} = \eta C \left[- \left(\frac{d_r}{d_r + d_t} \right) \left(\frac{\hat{K}_2}{g} \right) - \left(\frac{2}{d_r + d_t} \right) \hat{K}_4 \right] \quad (44)$$

The adjustment influence equations, (41) through (44), are applicable to the adjustment requirements for all three adjustment mechanisms, i. e., the coarse balance screws, the fine balance screws, and the mercury-filled balance tubes. When these equations are applied to the adjustment requirements for a particular one of the adjustment mechanisms, the appropriate adjustment plane separation distances must be employed. This results in three distinct adjustment influence equation sets.

The adjustment plane separation distances for the present RGG arm design are listed in Table III. A single separation distance is listed for the coarse tangential adjustment screws as the mean distance between like pairs on each arm on the assumption that the mass of each screw in a pair is identical.

Table III. Adjustment Plane Separations

Adjustment Mechanism	d_r , cm	d_t (ave), cm	d_t (inner), cm
Coarse screws	6.812	4.112	3.343 ^a
Fine screws	5.542	3.637	3.637
Balance Tubes	10.967	10.967	10.967
^a $\left. \frac{d_t}{2} \right _{\text{inner}} \triangleq 0.568''$			

The adjusting influence equation sets are numerically evaluated in (45) through (56) assuming the following units:

$$\delta p \text{ in gm-cm}$$

$$K_1, K_2 \text{ in EU/g}$$

$$K_4, K_5 \text{ in EU-sec}^2$$

COARSE BALANCE SCREWS

$$\delta p_{r1} = 10^{-8} [1.38 \hat{K}_2 - 809 \hat{K}_4] \quad (45)$$

$$\delta p_{t1} = 10^{-8} [-2.81 \hat{K}_1 - 809 \hat{K}_5] \quad (46)$$

$$\delta p_{r2} = 10^{-8} [1.38 \hat{K}_1 - 809 \hat{K}_5] \quad (47)$$

$$\delta p_{t2} = 10^{-8} [-2.81 \hat{K}_2 - 809 \hat{K}_4] \quad (48)$$

FINE BALANCE SCREWS

$$\delta p_{r1} = 10^{-8} [1.66 \hat{K}_2 - 895 \hat{K}_4] \quad (49)$$

$$\delta p_{t1} = 10^{-8} [-2.53 \hat{K}_1 - 895 \hat{K}_5] \quad (50)$$

$$\delta p_{r2} = 10^{-8} [1.66 \hat{K}_1 - 895 \hat{K}_5] \quad (51)$$

$$\delta p_{t2} = 10^{-8} [-2.53 \hat{K}_2 - 895 \hat{K}_4] \quad (52)$$

BALANCE TUBES

$$\delta p_{r1} = 10^{-8} [2.10 \hat{K}_2 - 375 \hat{K}_4] \quad (53)$$

$$\delta p_{t1} = 10^{-8} [-2.10 \hat{K}_1 - 375 \hat{K}_5] \quad (54)$$

$$\delta p_{r2} = 10^{-8} [2.10 \hat{K}_1 - 375 \hat{K}_5] \quad (55)$$

$$\delta p_{t2} = 10^{-8} [-2.10 \hat{K}_2 - 375 \hat{K}_4] \quad (56)$$

In order to determine the required adjustment of individual balance tube sets, the orientation of the balance tube sets must be considered. In the present RGG configuration, the balance tube adjustment axes (\bar{a} , \bar{b}) are rotated about the torsion axis approximately 45° from the rotor reference axes (\bar{i} , \bar{j}) as shown in Figure 1.

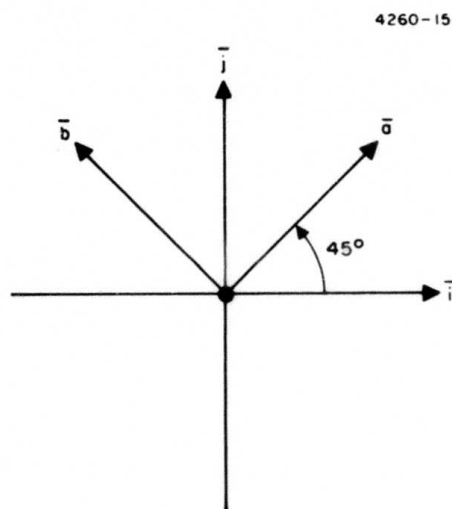


Figure 1

The appropriate balance tube mass moment changes are obtained by coordinate transformation of the elements of (53) through (56) as shown in (57) through (60).

$$\delta p_{a1} = [\delta p_{r1} + \delta p_{t1}] [\sqrt{2}/2] \quad (57)$$

$$\delta p_{b1} = [\delta p_{t1} - \delta p_{r1}] [\sqrt{2}/2] \quad (58)$$

$$\delta p_{a2} = [\delta p_{r2} + \delta p_{t2}] [\sqrt{2}/2] \quad (59)$$

$$\delta p_{b2} = [\delta p_{r2} - \delta p_{t2}] [\sqrt{2}/2] \quad (60)$$

Substitution of (57) through (60) into (53) through (56) yields the balance tube influences as (61) through (64).

$$\delta p_{a1} = 10^{-8} [1.48 (\hat{K}_2 - \hat{K}_1) - 265 (\hat{K}_4 + \hat{K}_5)] \quad (61)$$

$$\delta p_{b1} = 10^{-8} [-1.48 (\hat{K}_1 + \hat{K}_2) + 265 (\hat{K}_4 - \hat{K}_5)] \quad (62)$$

$$\delta p_{a2} = 10^{-8} [1.48 (\hat{K}_1 - \hat{K}_2) - 265 (\hat{K}_4 + \hat{K}_5)] \quad (63)$$

$$\delta p_{b2} = 10^{-8} [1.48 (\hat{K}_1 + \hat{K}_2) + 265 (\hat{K}_4 - \hat{K}_5)] \quad (64)$$

In addition to the differential and dynamic arm mass balance adjustments, the balance screws will be employed to adjust the sum mode mismatch error coefficient, K_6 , by changing the polar moments of inertia of the two arms. Both for analytical and test convenience, it is planned that all the adjustment screws in a given set will be of equal mass. This assumption leads to four mass parameters, (M_{r1} , M_{t1} , M_{r2} , M_{t2}), which are defined here as the mass of each screw in a given set. The change in the polar moments of inertia of the arms may be expressed to first order in terms of the appropriate mass, the separation distance of the masses in the adjustment direction, and the incremental change in this separation distance as in (65) and (66).

$$\delta\Phi_{kk1} = 2M_{r1} S_{r1} (\delta S_{r1}) + 4M_{t1} S_{t1} (\delta S_{t1}) \quad (65)$$

$$\delta\Phi_{kk2} = 2M_{r2} S_{r2} (\delta S_{r2}) + 4M_{t2} S_{t2} (\delta S_{t2}) \quad (66)$$

The change in the differential polar inertia is obtained by subtracting (66) from (65).

$$\begin{aligned} \delta(\Delta\Phi_{kk}) &= 2M_{r1} S_{r1} (\delta S_{r1}) + 4M_{t1} S_{t1} (\delta S_{t1}) \\ &\quad - 2M_{r2} S_{r2} (\delta S_{r2}) - 4M_{t2} S_{t2} (\delta S_{t2}) \end{aligned} \quad (67)$$

The change in the sum mode mismatch error coefficient from Appendix C-II is stated as (68).

$$\delta(K_6) = \left[\frac{\beta_0^2}{\omega_0^2 - \beta_0^2} \right] \left[\frac{\delta(\Delta\Phi_{kk})}{\eta C} \right] \quad (68)$$

In order to minimize the error coefficient estimate, \hat{K}_6 , the change in (68) should be equal and opposite to the estimate as stated by (69).

$$\delta(\Delta\Phi_{kk}) \triangleq \eta C \left[1 - \left(\frac{\omega_0}{\beta_0} \right)^2 \right] \hat{K}_6 \quad (69)$$

When the polar inertia increment is expressed in gm-cm^2 and the error coefficient is expressed in EU-sec^2 , the numerical value of (69) is expressed as (70) for the present configuration. Note the negative sign.

$$\delta(\Delta\Phi_{kk}) \cong -9.35 \times 10^{-5} \hat{K}_6 \quad (70)$$

In order to simplify the computation of the inertia moment of (67), fixed separation distances, S_{r0} and S_{t0} , will be used for the laboratory test calculations as in (71).

$$\begin{aligned} \delta(\Delta\Phi_{kk}) \cong & 2 S_{r0} [M_{r1} (\delta S_{r1}) - M_{r2} (\delta S_{r2})] \\ & + 4 S_{t0} [M_{t1} (\delta S_{t1}) - M_{t2} (\delta S_{t2})] \end{aligned} \quad (71)$$

In the absence of better data, the approximate arm outside dimensions will be used to define the fixed separation distances. This assumption leads to the following values:

$$S_{r0} \triangleq 13 \text{ cm}$$

$$S_{t0} \triangleq 3.5 \text{ cm}$$

Substitution of these values into (71) and equating (70) and (71) yields the adjustment requirement of (72).

$$26[M_{r2} \delta S_{r2} - M_{r1} \delta S_{r1}] + 14[M_{t2} \delta S_{t2} - M_{t1} \delta S_{t1}] = 9.86 \times 10^{-5} \hat{K}_6 \quad (72)$$

If the radial screws only are employed in this adjustment process, the adjustment requirement is stated as (73).

$$[M_{r2} (\delta S_{r2}) - M_{r1} (\delta S_{r1})] \cong 15.0 \times 10^{-6} \hat{K}_6 \quad (73)$$

In addition to arm mass distribution adjustments, there are provisions for trimming the magnitude of the prime anisoelastic error coefficient, $\sqrt{K_7^2 + K_8^2}$, by removing material from specified parts of each arm plate. The arm plates have been designed to be anisoelastic

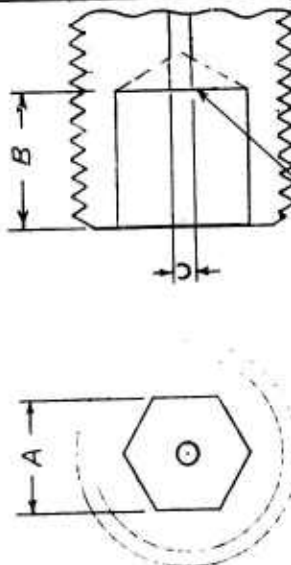
in a fixed direction so that the trimming process will reduce the anisoelastic error coefficient up to a point. At present the quantitative sensitivity of the trimming process is not well known, and until empirical data can be obtained the trimming process will be "cut and try" to avoid the "overshoot" possibility.

Balance Screw Influence (Mass Unbalance and Inertia)

Screw Size	$\delta P/\text{Turn}$ gm-cm/Turn			$\Delta\Phi$ Radial $\frac{\text{gm cm}^2}{\text{Turn}}/\text{Screw}$ $R \approx 5.6 \text{ cm}$	$\Delta\Phi$ Tangential $\frac{\text{gm cm}^2}{\text{Turn}}/\text{Screw}$ $R \approx 5.56$
	Number of Screws				
	1	2	4		
3/4 x 1/4-28	0.674	1.35	2.70	7.55	2.17
1/2 x 1/4-28	0.426	0.85	1.70	4.77	1.37
3/8 x 1/4-28	0.302	0.60	1.21	3.38	0.974
1/4 x 1/4-28	0.195	0.39	0.78	2.18	0.629
1/4 x #2-56	0.00894	0.018	0.036	0.100	0.0288

REVISIONS			
EFF	AUTHORITY	ZONE LTR	DESCRIPTION
		A	NOTE 1 ADDED
			DATE
			7-19-74
			APPROVED

ITEM	D	L	A	B	THREAD	CLASS	C	NO. REQ'D
1	.250	.750	.125	.187	1/4-28	3A	.031	24
2	.250	.500	.125	.187	1/4-28	3A	.031	24
3	.250	.375	.125	.187	1/4-28	3A	.031	24
4	.250	.250	.125	.125	1/4-28	3A	.031	24
5	.086	.187	.035	.062	2-56	3A	.021	16



FLAT OR CONICAL BOTTOM OPTIONAL

1. NON MAGNETIC CUTTING TOOL
EDGES REQUIRED FOR ALL FINISH CUTS

NOTES:

QTY REQD	CODE IDENT	PART NO. OR IDENTIFYING NO.	NOMENCLATURE OR DESCRIPTION	FIND NO.
PARTS LIST				
EXCEPT AS NOTED DIM. ARE IN INCHES AND PER ANS Y14.5 XXX XX ANGLES ±.010 ±.03 ±0°30'		HUGHES HUGHES AIRCRAFT COMPANY CULVER CITY, CALIFORNIA		
MATERIAL MALLORY-1000		BALANCE WEIGHTS		
DR GLW 7/2/74		SIZE (CODE IDENT NO) DRAWING NO. REV. A		
CHK		B 82577 140534		
APPD		SCALE		
NEXT ASSY		USED ON		
APPLICATION				

	W	\bar{x}	\bar{y}	\bar{z}	$W_{\bar{x}}$	$W_{\bar{y}}$	$W_{\bar{z}}$	I_{XXCG}	I_{YYCG}	I_{ZZCG}	$W\Delta\bar{z}^2$	$W(\bar{x}^2 + \bar{y}^2)$	I_{XX}	I_{YY}	I_{ZZ}
End Masses (includes 2 small and 2 large weights, alumi- num inserts, balance screw holes and screws)	2.2262	(±2.282)	0	1.0403	0	0	2.3159	1.3512	12.5930	12.0800	0.0012	0	1.3524	12.5942	12.0800
End Mass Mounting Bolts (2)	0.2815	(±2.211)	0	1.054	0	0	0.2967	0.2411	1.6174	1.3834	0	0	0.2411	1.6174	1.3834
Inner Arm Plate (including effect of aniso. cutouts and screw holes)	0.4143	0	0	-0.182	0	0	-0.0754	0.2177	0.8857	1.1456	0.6425	0	0.8602	1.5282	1.1456
Outer Arm Plate	0.4130	0	0	2.290	0	0	0.9458	0.2177	0.8857	1.1454	0.6215	0	0.8392	1.5072	1.1454
Balance Tubes and Mtg. Brackets	0.1006	0	0	2.613	0	0	0.2629	0.0320	0.1142	0.1372	0.2416	0	0.2736	0.3558	0.1372
Transducer Mounts:															
Inner Arm	0.0259	0	0	-0.580	0	0	-0.0168	0.0082	0.0082	0.0160	0.0780	0	0.0862	0.0862	0.0160
Outer Arm	0.0289	0	0	1.892	0	0	0.0547	0.0082	0.0082	0.0160	0.0198	0	0.0280	0.0280	0.0160
Transducer Cross- Thru Spud	0.0340	0	0	-0.859	0	0	-0.0292	0.0030	0.0030	0.0033	0.1256	0	0.1286	0.1286	0.0033
Pivots and Pivot Bosses	0.0021	0	0	0.152	0	0	0.0003	0.0011	0.0011	0.0002	0.0017	0	0.0028	0.0028	0.0002
Transducers	0.0032	0	0	0.449	0	0	0.0014	0.0044	0.0044	0.0010	0.0012	0	0.0056	0.0056	0.0010
Totals	3.5327	0	0	1.0633	0	0	3.7563						3.8177	17.8540	15.9281

$$\eta \triangleq \frac{I_{YY} - I_{XX}}{I_{ZZ}} = \frac{17.8540 - 3.8177}{15.9281} = 0.88123$$

$$\eta^2 I_{ZZ} = 12.3692 \text{ lb-in.}^2 = 36,198 \text{ g-cm}^2$$

$$\eta^2 I_{ZZ} \text{ for original design goal of } 1/3 \text{ E. U. was } 26,400 \text{ g-cm}^2$$

$$\sigma_{\text{THERMAL NOISE}} = \frac{1}{3} \times \sqrt{\frac{26,400}{36,198}} = 0.285 \text{ E. U.}$$

APPENDIX C-I SIMPLIFIED TEST AND ESTIMATION

The simplified test and estimation processes mentioned in the main text are based on the concept of "pure excitation" functions. The "inner-rotor" is to be vibrated either linearly or angularly along or about one of its cardinal reference axes for each test condition. Two test condition sets are to be employed for error coefficient estimation, a preliminary six condition test set and a final ten condition test set. The test conditions are described by Tables I and II, respectively. Each test requires observation of the change in the average output of each RGG channel, defined here as ϵ_c and ϵ_s . These observed output changes must be employed to estimate the "effective-input parameters," \hat{e}_a and \hat{e}_b , which are defined by 1A and 2A in terms of the estimated gain and phase, \hat{K}_0 and $\hat{\phi}_0$, of the RGG signal process.

Table I. Six Condition Test Set

Test Condition Number	Vertical Axis	Excitation Function	Effective Input
1	i	n_{i1}	$K_1 n_{i1}$
2	j	n_{j2}	$K_2 n_{j2}$
3	k	n_{k3}	$K_3 n_{k3}$
4	i	$\dot{\omega}_{i4}$	$K_4 \dot{\omega}_{i4}$
5	j	$\dot{\omega}_{j5}$	$K_5 \dot{\omega}_{j5}$
6	k	$\dot{\omega}_{k6}$	$K_6 \dot{\omega}_{k6}$

Table II. Ten Condition Test Set

Test Condition Number	Vertical Axis	Excitation Function	Effective Input
1	i	n_{i1}	$(K_2 - 2K_8) n_{i1}$
2	j	n_{j2}	$(K_2 + 2K_8) n_{j2}$
3	k	n_{k3}	$K_3 n_{k3}$
4	i	$\dot{\omega}_{i4}$	$K_4 \dot{\omega}_{i4}$
5	j	$\dot{\omega}_{j5}$	$K_5 \dot{\omega}_{j5}$
6	k	$\ddot{\omega}_{k6}$	$K_6 \ddot{\omega}_{k6}$
7	j	n_{i7}	$(K_1 + 2K_7) n_{i7}$
8	i	n_{j8}	$-(K_2 + 2K_7) n_{j8}$
9	k	n_{j9}	$(K_2 + K_9) n_{j9}$
10	k	n_{i10}	$(K_1 - K_{10}) n_{i10}$

$$\hat{e}_a \triangleq \frac{1}{K_0} [e_c \cos \hat{\phi}_0 - e_s \sin \hat{\phi}_0] \quad (1A)$$

$$\hat{e}_b \triangleq \frac{1}{K_0} [e_s \cos \hat{\phi}_0 + e_c \sin \hat{\phi}_0] \quad (2A)$$

If the RGG signal process is set up with a nominal unit functional gain and with the phase equalling an even multiple of π , the "effective-input parameter" estimates are equal to the average output of each RGG channel as is apparent from (1A) and (2A).

The "excitation parameters" for each test condition must be determined by measurement. These are the values of the in-phase and quadrature components of the appropriate excitation function relative to the excitation and detection reference generator. These parameters are defined for the six degrees of freedom by (3A) through (8A).

$$n_i \triangleq n_{ai} + jn_{bi} \quad (3A)$$

$$n_j \triangleq n_{aj} + jn_{bj} \quad (4A)$$

$$n_k \triangleq n_{ak} + jn_{bk} \quad (5A)$$

$$\dot{\omega}_i \triangleq \dot{\omega}_{ai} + j\dot{\omega}_{bi} \quad (6A)$$

$$\dot{\omega}_j \triangleq \dot{\omega}_{aj} + j\dot{\omega}_{bj} \quad (7A)$$

$$\dot{\omega}_k \triangleq \dot{\omega}_{ak} + j\dot{\omega}_{bk} \quad (8A)$$

The error coefficient estimates for the six condition test set are defined by (9A) through (14A) as the real part of the appropriate input/excitation ratios.

$$\hat{K}_1 \triangleq [e_{a1} n_{ai1} + e_{b1} n_{bi1}] / |n_{i1}|^2 \quad (9A)$$

$$\hat{K}_2 \triangleq [e_{a2} n_{aj2} + e_{b2} n_{bj2}] / |n_{j2}|^2 \quad (10A)$$

$$\hat{K}_3 \triangleq [e_{a3} n_{ak3} + e_{b3} n_{bk3}] / |n_{k3}|^2 \quad (11A)$$

$$\hat{K}_4 \triangleq [e_{a4} \dot{\omega}_{ai4} + e_{b4} \dot{\omega}_{bi4}] / |\dot{\omega}_{i4}|^2 \quad (12A)$$

$$\hat{K}_5 \triangleq [e_{a5} \dot{\omega}_{aj5} + e_{b5} \dot{\omega}_{bj5}] / |\dot{\omega}_{j5}|^2 \quad (13A)$$

$$\hat{K}_6 \triangleq [e_{a6} \dot{\omega}_{ak6} + e_{b6} \dot{\omega}_{bk6}] / |\dot{\omega}_{k6}|^2 \quad (14A)$$

The error coefficient estimates for the ten condition test set may be approached in the same manner by taking the real parts of the input/excitation ratios. The estimates of K_3 , K_4 , K_5 , and K_6 are obtained directly as defined by (11A) through (14A), but the remaining input/excitation ratios yield estimates of combinations of the differential mass unbalance and anisoelastic error coefficients as defined by (15A) through (20A).

$$[\hat{K}_1 - 2\hat{K}_8] \triangleq [e_{a1} n_{ai1} + e_{b1} n_{bi1}] / |n_{i1}|^2 \quad (15A)$$

$$[\hat{K}_2 + 2\hat{K}_8] \triangleq [e_{a2} n_{aj2} + e_{b2} n_{bj2}] / |n_{j2}|^2 \quad (16A)$$

$$[\hat{K}_1 + 2\hat{K}_7] \triangleq [e_{a7} n_{ai7} + e_{b7} n_{bi7}] / |n_{i7}|^2 \quad (17A)$$

$$[\hat{K}_2 + 2\hat{K}_7] \triangleq [e_{a8} n_{aj8} + e_{b8} n_{bj8}] / |n_{j8}|^2 \quad (18A)$$

$$[\hat{K}_2 + \hat{K}_9] \triangleq [e_{a9} n_{aj9} + e_{b9} n_{bj9}] / |n_{j9}|^2 \quad (19A)$$

$$[\hat{K}_1 - \hat{K}_{10}] \triangleq [e_{a10} n_{ai10} + e_{b10} n_{bi10}] / |n_{i10}|^2 \quad (20A)$$

A further simultaneous solution is required to separate the error coefficients. The results of this solution are presented as (21A through (26A).

$$\hat{K}_1 = \frac{1}{2} [(\hat{K}_1 - 2\hat{K}_8) + (\hat{K}_2 + 2\hat{K}_8) + (\hat{K}_1 + 2\hat{K}_7) + (\hat{K}_2 + 2\hat{K}_7)] \quad (21A)$$

$$\hat{K}_2 = \frac{1}{2} [(\hat{K}_1 - 2\hat{K}_8) + (\hat{K}_2 + 2\hat{K}_8) - (\hat{K}_1 + 2\hat{K}_7) - (\hat{K}_2 + 2\hat{K}_7)] \quad (22A)$$

$$\hat{K}_7 = \frac{1}{4} [(\hat{K}_1 + 2\hat{K}_7) - (\hat{K}_2 + 2\hat{K}_7) - (\hat{K}_1 - 2\hat{K}_8) - (\hat{K}_2 + 2\hat{K}_8)] \quad (23A)$$

$$\hat{K}_8 = \frac{1}{4} [(\hat{K}_2 + 2\hat{K}_8) - (\hat{K}_1 - 2\hat{K}_8) + (\hat{K}_1 + 2\hat{K}_7) + (\hat{K}_2 + 2\hat{K}_7)] \quad (24A)$$

$$\hat{K}_9 = [(\hat{K}_2 + \hat{K}_9) - \hat{K}_2] \quad (25A)$$

$$\hat{K}_{10} = [\hat{K}_1 - (\hat{K}_1 - \hat{K}_{10})] \quad (26A)$$

Note that when the anisoelastic parameter, K_8 , is small, (15A) and (16A) provide direct estimates of K_1 and K_2 , and the solution for K_7 is obtained simply from (17A) and/or (18A).

$$\hat{K}_1 = -\frac{1}{2}(T_{11} + T_{12} + T_{17} + T_{18})$$

$$\hat{K}_2 = -\frac{1}{2}(T_{11} + T_{12} - T_{17} - T_{18})$$

$$\hat{K}_7 = +\frac{1}{4}(T_{17} - T_{18} - T_{11} - T_{12})$$

$$\hat{K}_8 = +\frac{1}{4}(T_{12} - T_{11} + T_{17} + T_{18})$$

where

$$\hat{T}_{11} = -K_1 - 2K_8$$

$$\hat{T}_{17} = -K_1 + 2K_7$$

$$\hat{T}_{12} = -K_2 + 2K_8$$

$$\hat{T}_{18} = +K_2 + 2K_7$$

APPENDIX C-II

ERROR COEFFICIENT DEFINITIONS

For analytical convenience, an arbitrary set of error coefficients, K_1 through K_{10} , have been employed to describe the "effective inputs" for the non-spinning inner-rotor tests. The intent of this appendix is to define the relations between these error coefficients and the physical parameters they represent.

DIFFERENTIAL MASS UNBALANCE

$$K_1 \triangleq p_{dj}g/\eta C$$

$$K_2 \triangleq -p_{di}g/\eta C$$

AXIAL VIBRATION SENSITIVITY

$$K_3 \triangleq p_{dk}g/\eta C$$

DYNAMIC MASS UNBALANCE

$$K_4 \triangleq -\Delta\Phi_{ik}/\eta C$$

$$K_5 \triangleq -\Delta\Phi_{jk}/\eta C$$

SUM MODE MISMATCH

$$K_6 \triangleq \left[\frac{\beta_0^2}{\omega_0^2 - \beta_0^2} \right] \left[\frac{-(\Delta K/\beta_0^2) + \Delta\Phi_{kk}}{\eta C} \right]$$

PRIME ANISO ELASTICITY

$$K_7 \triangleq [K_{ii} - K_{jj}] g^2 / 2\eta C$$

$$K_8 \triangleq K_{ij} g^2 / \eta C$$

CROSS ANISO ELASTICITY

$$K_9 \triangleq K_{ik} g^2 / \eta C$$

$$K_{10} \triangleq K_{jk} g^2 / \eta C$$

NOMENCLATURE

a_i, a_j, a_k	RGG rotor acceleration components
\bar{a}, \bar{b}	Balance tube reference coordinates
C	Arm polar inertia
c_{ig}, c_{jg}, c_{kg}	Gravity vector direction Cosines
d_r	Separation distances of the radial adjustment planes of the two arms
d_t	Separation distances of the tangential adjustment planes of the two arms
ϵ	Effective input to the RGG signal process
$\epsilon_i, \epsilon_j, \epsilon_k$	Effective inputs defined by 3, 4, and 5
e_c, e_s	Change in outputs of RGG signal process
ϵ_a, ϵ_b	Effective input components
$\bar{\epsilon}, \hat{\epsilon}$	Effective input vector and its estimate
$\overline{\Delta\epsilon}$	Effective input estimation error
E_i, E_j, E_k	Magnitudes of effective input functions
$\overline{\overline{E}}$	Excitation matrix
\bar{g}, g	Gravity vector and scalar magnitude

$\bar{i}, \bar{j}, \bar{k}$	RGG inner rotor reference coordinates
$K_1 \rightarrow K_{10}$	Motion sensitive error coefficients defined in Appendix C-II
K_0	RGG Signal Process Gain
$\bar{K}, \hat{\bar{K}}$	Error coefficient vector and its estimate
$\overline{\Delta K}$	Error coefficient estimation error
ΔL_k	Differential torque acting on RGG differential mode
M_r, M_t	Mass of each radial or tangential adjustment screw
$\overline{\overline{M}}$	Measurement Matrix
M_i	Diagonal Scalar element of the measurement matrix
ΔM_{ij}	Scalar element of measurement matrix error
n_i, n_j, n_k	RGG rotor normalized translational vibration components
n_a, n_b	Inphase and quadrature vibration components
\bar{p}	RGG arm mass moment
p_r, p_t	Mass moments of radial and tangential adjustment screws
$\delta p_r, \delta p_t$	Changes in adjustment screw mass moments
$\delta p_a, \delta p_b$	Changes in balance tube mass moments

δp_d	Changes in differential arm mass unbalance
S_r	Separation distance of the radial adjustment screws in the radial direction
S_t	Separation distance of the tangential adjustment screws in the tangential direction
$\delta S_r, \delta S_t$	Changes in the separation distances
β_0	Sum mode frequency
Δ, δ	Difference or incremental change
η	RGG arm inertia efficiency
Γ_{ij}	Component of gravity gradient tensor
Φ_{ij}	Component of the inertia tensor of an RGG arm
$\Delta\Phi_{ij}$	Component of the differential inertia tensor of the two RGG arms
$\phi_0, \hat{\phi}_0$	Phase shift of RGG signal process and its estimate
ϕ_i	Phase angle of the ith effective input
ω_e	Excitation frequency
ω_s	RGG spin speed
$\omega_i, \omega_j, \omega_k$	RGG rotor angular velocity components
$\dot{\omega}_i, \dot{\omega}_j, \dot{\omega}_k$	RGG rotor angular acceleration components

ω_0	Differential Mode resonant frequency
Ω	Earth rate vector
Ω_i, Ω_j	Earth rate components in rotor reference frame
Ω_H, Ω_V	Horizontal and vertical earth rate components

REFERENCES

1. Ames, C. B., R. L. Forward, et al, "Prototype Moving Base Gravity Gradiometer," Semiannual Technical Report 1, Contr F19628-72-C-0222, August 1972.
2. Ames, C. B., R. L. Forward, et al, "Prototype Moving Base Gravity Gradiometer," Semiannual Technical Report 2, Contr F19628-72-C-0222, January 1973.
3. Peterson, R. W., "Rigid Body Reaction Moments of the Rotating Gravity Gradiometer," Hughes Research Report 467, May 1973.
4. Peterson, R. W., "Skew Sensitive Errors of the Rotating Gravity Gradiometer," Hughes Research Report 468, May 1973.